PREPARATION AND SURFACE CHARACTERIZATION OF ZIRCONIUM CARBIDE SINGLE CRYSTALS

William Ansel Mackie

B.A., Linfield College, McMinnville, Oregon, 1971

A dissertation submitted to the faculty

of the Oregon Graduate Center

in partial fulfillment of the

requirements for the degree

Doctor of Philosophy

in

Applied Physics

August 1987

The dissertation "Preparation and Surface Characterization of Zirconium Carbide Single Crystals" by William Ansel Mackie has been examined and approved by the following Examination Committee:

Paul R. Davis, Thesis Advisor
Associate Professor

Lynwood W. Swanson
Professor

Richard A. Elliott
Professor

Clarence H. Hinrichs
Professor, Linfield College

ACKNOWLEDGEMENTS

The work carried out here was financed primarily by the Murdock Charitable Trust. In addition, a smaller grant from Rasor Associates, Inc. was used for a portion of the thermionic study.

I especially would like to thank Dr. Paul R. Davis, my thesis advisor, who gave me considerable advice and assistance. In addition, I would like to give special thanks to Dr. Clarence H. Hinrichs, without whose help this research would not have been possible. Dr. Lynwood W. Swanson also gave stimulating advice and guidance which was very helpful and greatly appreciated.

I would also like to thank Noel Martin at FEI Co. for technical advice and assistance, and the Hewlett-Packard's McMinnville Division for LN_2 donations.

Additionally, my thanks go to the faculty, staff and especially the students of Linfield College who have participated in the Murdock research work, and to the Oregon Graduate Center for the excellent instruction and facilities.

TABLE OF CONTENTS

PART TWO: SURFACE ANALYSIS AND WORK FUNCTION STUDIES

I. EXPERIMENTAL SPECIMEN PREPARATION

A. SPECIAL CONSIDERATIONS FOR ZIRCONIUM CARBIDE

B. MOUNTING METHODS

i) Field Emission Cathode Mounting

1) Tantalum Wire/Brazing

2) Vogel Type Mounting

3) Electron Bombardment Heating

4) Tantalum/Rhenium Cups

ii) Thermionic Cathode Mounting

1) Effective Thermionic Work Function Samples

2) Hemispherical Samples for TPM

iii) FERP/AES Study Crystal Mounting

C. SPECIMEN CRYSTALLOGRAPHIC ORIENTATION

D. FIELD EMITTER TIP PREPARATION

i) Etching

ii) Tip Grinding

iii) Grinding/Etching

II. EXPERIMENTAL TECHNIQUES AND RESULTS

A. FIELD EMISSION RETARDING POTENTIAL (FERP) MEASUREMENTS

i) Theoretical Background

ii) Experimental

LIST OF FIGURES AND TABLES

ABSTRACT

Preparation and Surface Characterization
of Zirconium Carbide
Single Crystals

William Ansel Mackie, Ph.D.

Oregon Graduate Center, 1987

Supervising Professor: Paul R. Davis

The first aim of the research was the production of single crystal samples of ZrC using an arc heated floating zone technique. The second was a work function study of single crystal planes of ZrC using thermionic emission techniques, supplemented with field emission data.

A semi-empirical work function theory is developed to predict the clean surface work functions of ZrC, as a function of crystallographic orientation. The theory predicts work function variations with stoichiometry for ZrC and other transition metal carbides.

A detailed description is given of the apparatus and the procedures used for the production of single crystal samples of ZrC. The initial material was sintered ZrC having an average C/Zr ratio of 0.98. The final products were centerless ground single crystal samples with stoichiometries between 0.84 and 0.96.

To obtain accurate thermionic data the spectral emissivity of crystalline $ZrC_{0.91}$ was measured with resulting data yielding $\varepsilon(0.65\ \mu m)$ in the temperature range $1200 < T < 2400$ K. There were no effects

due to crystallographic direction noted.

Thermionic work function measurements are reported for five $ZrC_{0.896}$ crystal samples. Data were taken for temperatures in the range 1800 to 2500 K and analyzed using Schottky plots and Richardson's equation with the pre-exponential constant equal to 120 $A\text{-}cm^{-2}K^{-2}$. Results obtained from (100) and (210) crystal planes are graphed to show the temperature dependence of the effective thermionic work function.

Relative work functions are presented using direct observation of thermionic emission patterns from a hemispherical ZrC single crystal. The relative effect of oxygen on single plane thermionic work functions is also depicted.

The thermionic work function data are compared with absolute, room temperature work function measurements made using the field emission retarding potential method. These data are correlated with Auger electron spectroscopic data taken to show temperatures needed for thermal desorption of adsorbates and stoichiometric changes as a function of temperature.

Finally, a cursory examination of the field emission properties of ZrC is made. Cathode etching and mounting procedures are examined and an emission pattern produced from a clean ZrC surface. The relative work function ordering of the crystal planes agrees with the thermionic data and the work function model's predictions.

INTRODUCTION

The impetus for this research was initially the investigations of some of the transition metal carbides relative to their use as field emission cathodes. It was known that initial investigations to this end had been made on TiC. At the outset then, the aim was to generate feasibility studies and comparative data on other transition metal carbides used specifically in the field emission mode.

As investigations started, it became clear that the acquisition of the material itself was a problem. This necessitated the construction and development of metal carbide crystal growing apparatus and techniques. This area of materials preparation was studied until we could routinely and consistently produce specimens of proper dimensions and characteristics.

During the course of these material studies, and after preliminary field emission cathode testing and absolute work function analysis of the (100) plane of ZrC, we became interested in the question of high temperature thermionic work functions. The motivation for this interest was the search for better cathodes used in thermionic energy converters. Since the material studies had enabled production of ZrC single crystal specimens, the thermionic study was natural.

Literature values for effective thermionic work function and spectral emissivity of the carbides are conflicting and uncertain, most

research having been done with sintered material. Therefore, we measured the spectral emissivity of crystalline ZrC over a wide range of temperatures, including those high temperatures used for the thermionic work function studies.

As a means of comparing relative work functions, hemispherical thermionic emission patterns from single crystal ZrC samples were obtained. These data are compared with the field emission data noting similarities and differences in the features.

To augment the work function data and as a means of understanding the surface composition changes at high temperatures, under varying stoichiometries and in the presence of oxygen, Auger data are introduced. The changes in work function noted in the retarding potential data with adsorbed oxygen are compared with the changes in the work function of single crystal ZrC thermionic emitters.

The relevant primary and peripheral data are compiled and compared. Conclusions are drawn from these data and compared with the empirical model developed. The final results are 1) work function data for zirconium carbide and 2) an explanation of the surface phenomena involved.

PART ONE: BULK MATERIALS PREPARATION AND ANALYSIS

As stated in the introduction, the fabrication of suitable samples of transition metal carbides could be a research topic in and of itself. The development and the perfecting of the capability to grow suitable single crystals has consumed a great deal of time. Since a ready source of crystal specimens was not available, an in-house source became imperative. While, as always, there is more to be learned about the crystal growing process, enough is now known to reliably produce single crystal zirconium carbide samples for this and other* research efforts.

* Rasor Associates Inc. have contracted to use the procedures developed here to provide them with ZrC samples for their project.

I. BACKGROUND

Transition metal carbides are cubic materials with a crystal lattice identical to that of sodium chloride. (see Fig. 1) The atomic spacing varies slightly with stoichiometry as is indicated in Fig. 2. This variation has been measured and/or compiled by Storms.[1]

The refractory metal carbides exhibit unique physical properties. Collectively they are the hardest compounds known and have some of the highest melting points. Table I is a compilation of some of their physical properties.

Their phase diagrams also reveal interesting features. Transition metal carbides can exist over a wide range of stoichiometries. Changes in stoichiometries occur due to carbon vacancies in the lattice structure, and cause lattice parameter changes.[1] (See Fig. 2 for lattice changes associated with ZrC stoichiometric changes.)

In the case of ZrC, the large composition range of the solid, single phase ZrC[1] makes the preparation of single crystal samples of the desired stoichiometry difficult (see Fig. 3). The process used in this study is that of floating zone melting, described in Part One, Section III.

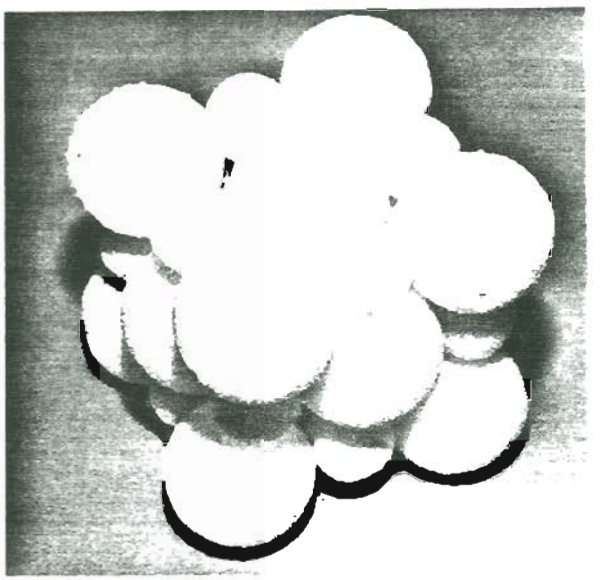

Fig. 1: Zirconium carbide crystal structure, face centered cubic zirconium with a basis of carbon. (NaCl type lattice structure.)

TABLE I: Properties of Transition Metal Carbides.[2]

Formula	Molecular Weight	Melting Point (C)	Thermal Conductivity ($\frac{\text{cal-cm}}{\text{sec-cm}^2\text{-C}}$)	Electrical Resistivity ($\mu\Omega$ - cm)	Hardness (kg/mm^2)
TiC	59.91	3160	0.049	180-250	3200
ZrC	103.23	3030	0.049	~70	2600
NbC	104.92	3500	0.034	74	2470
HfC	190.51	3890	-	109	--
TaC	192.96	3880	0.053	170-200	1800

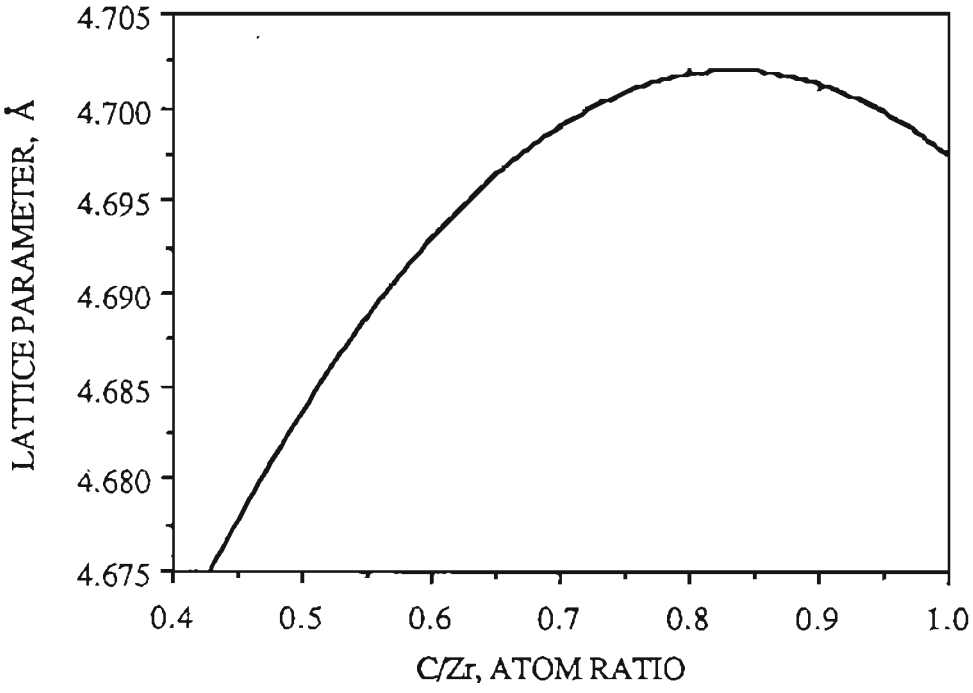

Fig. 2: Lattice parameter of ZrC as a function of composition.

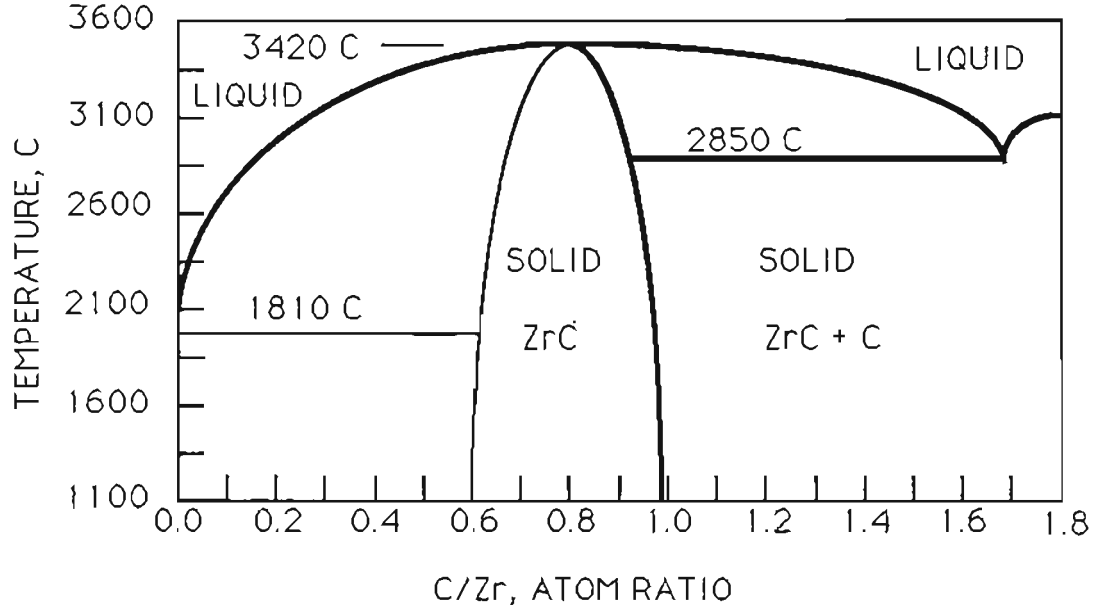

FIG. 3: Phase diagram of the zirconium carbide system.

II. SINTERING PROCESS

The starting material for the zone melting process is the sintered transition metal carbide. Sintering can be accomplished through a four step process. The "raw" material, for example, might consist of powdered ZrC with a 325 mesh particle size. This powder (as well as that of the other carbides) was obtained from Teledyne-Wah Chang in Albany, OR. A stoichiometric and purity analysis conducted by Wah-Chang showed a carbon to zirconium ratio of 0.99 with the following concentrations of impurities: 50 ppm hafnium, 95 ppm nitrogen, and 690 ppm oxygen.

The first step in sintering is to add a binder to the powdered ZrC so the material will keep its physical shape after pressing and until the actual sintering is completed. The binder used in this study was paraffin. This was added to the ZrC powder in the form of a solution of paraffin in heptane. Mixed to a moist consistency, a typical 50-100 gram sample was then placed in a oven to remove the heptane. This is accomplished by baking for two hours at 70 C in a vacuum oven which is maintained at a pressure of around 50 microns.

The resulting mixture of powder and paraffin was next cold pressed in the second step of the process. This was done in a hydraulic press capable of exerting a pressure of approximately 2000 psi. The steel die had dimensions of 3.0 x 0.5 inches, yielding a pressed block roughly 0.5 inches thick.

The third step was the removal of the paraffin by vacuum baking prior to sintering. Since the pressed blocks are fragile after this step, they were placed directly on the carbon discs used in the sintering furnace. This allowed easy transfer after the wax removal process. The vacuum oven used in this step trapped the paraffin to prevent contamination of the pumping system. Baking was carried out over a four hour period at a temperature of 480 C, again at a pressure of 50 microns.

The last step is the actual sintering of the pressed ZrC blocks. This was achieved by heating in a carbon element vacuum furnace, maintained at a pressure of 13-15 microns, for at least four hours at a temperature up to 2200 C. Temperature measurement were made pyrometrically and were only approximate due to the configuration of the apparatus and the fogging of the viewport at temperatures greater than 2000 C.

The final density of the sintered blocks was 60-68% of theoretical. The blocks were relatively soft in that they could be scratched with one's fingernail. They were usable in this condition but a further attempt was made to increase the density on one of the samples by passing a high current through it in a vacuum system. A small hole was drilled in the side of the block to monitor the temperature pyrometrically. A current of approximately 2000 amperes was passed through the sample until the temperature read 3300-3400 C. The result was that further sintering did take place, but the piece was unusable

due to many small cracks which developed throughout the interior of the sample. These fissures may have developed because of the manner in which the block was held by the much cooler electrodes.

While the resistively heated method may prove useful with some modification, the furnace heated sintering process is adequate. Samples of three other transition metal carbides have been sintered in this manner, TiC, HfC and ZrC.

During the later phases of this research, sintered blocks were purchased from Degussa Electronics. These commercially prepared samples came in five inch diameter discs, 0.250 inches thick. They were harder, having a calculated density between 90-94% of theoretical for the samples obtained. All of the results presented in this dissertation come from samples prepared from commercially sintered stock.

III. ZONE MELTING

A. METHODOLOGY

The ability to produce single crystal samples of transition metal carbides was crucial to this research. The production of single crystals of ZrC by the method of floating zone melting has been reported by others.[3,4,5] Most, if not all, of the work with carbides has been done using rf induction heating. For example, Otani, et al.[4] have successfully produced single crystal samples of titanium carbide in a helium atmosphere. However, the pressures required by the rf heating method were high, 5-15 atmospheres. These pressures are needed to suppress arcing between the turns of the induction coil.

In the procedure reported on here, single crystal samples of transition metal carbides have been prepared in an inert gas at atmospheric pressure. Here, heating is achieved by means of an electric arc. This method is similar to that developed by Verhoeven, et al,[5] in which zone refining of LaB_6 was achieved by an arc induced floating zone technique.

B. APPARATUS

The apparatus built for this process is depicted in Fig. 4. A seed crystal is mounted vertically directly above a vertical piece of the sintered material to be zone melted. The sintered rod is cut from a block using a four or five inch diameter diamond saw, 0.010 to 0.025 inches in thickness. These rods range from 0.030 to 0.125 inches square and were up to 5 inches in length. The variation in size produced crystals with diameters appropriate for the experimental requirements. A horizontal negative electrode, or stinger, is supported on a screw driven stage which may be powered up or down. The holders for these three pieces are made from molybdenum to withstand the high temperatures generated during zone melting. The design is such as to allow vertical adjustment of the sintered stock rod and horizontal adjustment of the stinger during the zone melting run. This entire configuration is mounted on a quick-change vacuum system under a removable bell jar.

Heating is accomplished by an electric arc through an inert atmosphere between the stinger and the molten zone. This molten zone is suspended by surface tension between the seed crystal and the sintered stock rod. The arc is initiated by means of a high voltage DC pulse. The schematic of the electrical configuration is shown in Fig. 5.

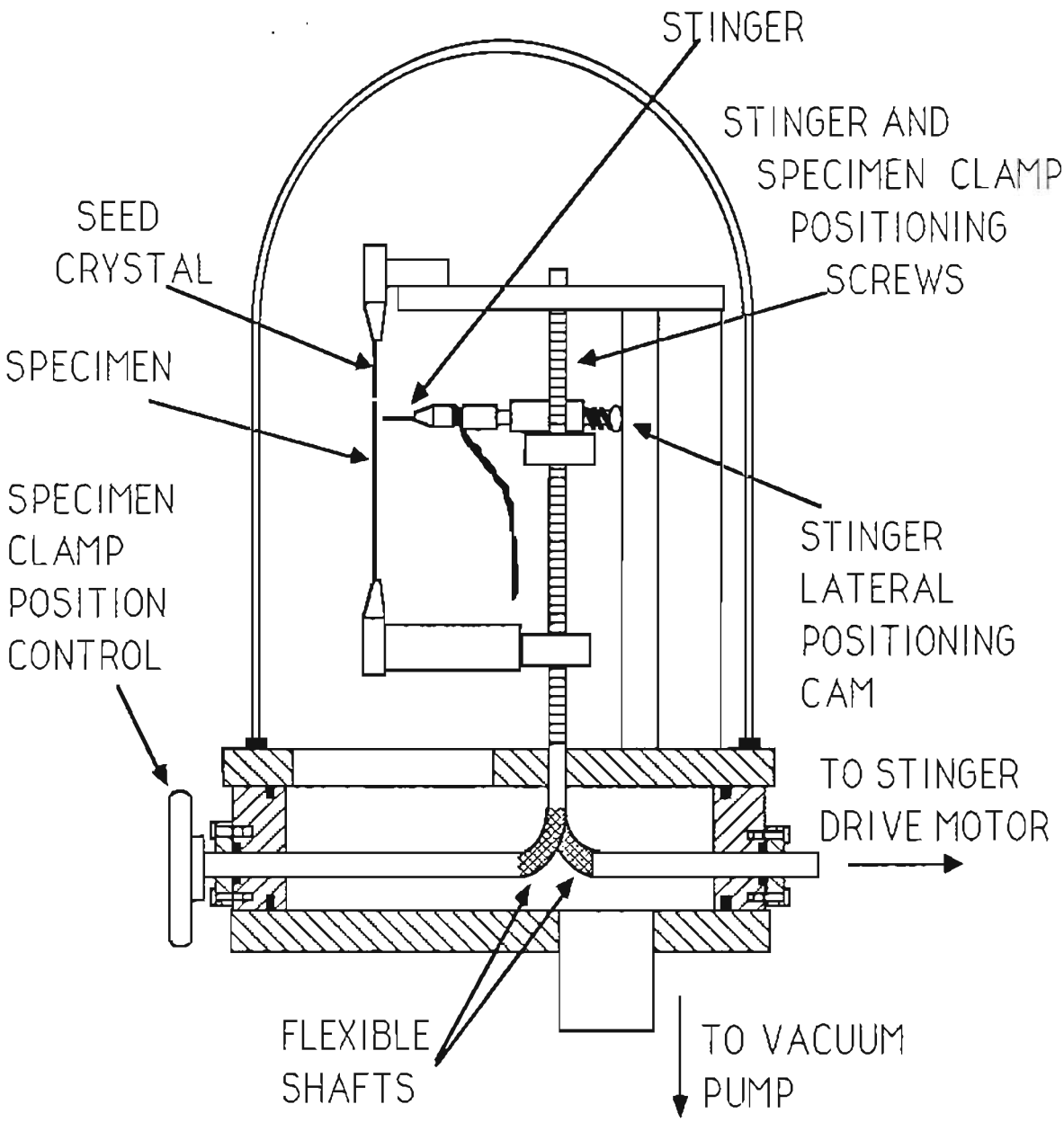

FIG. 4: Floating zone melting apparatus used in the production of single crystal samples of transition metal carbides.

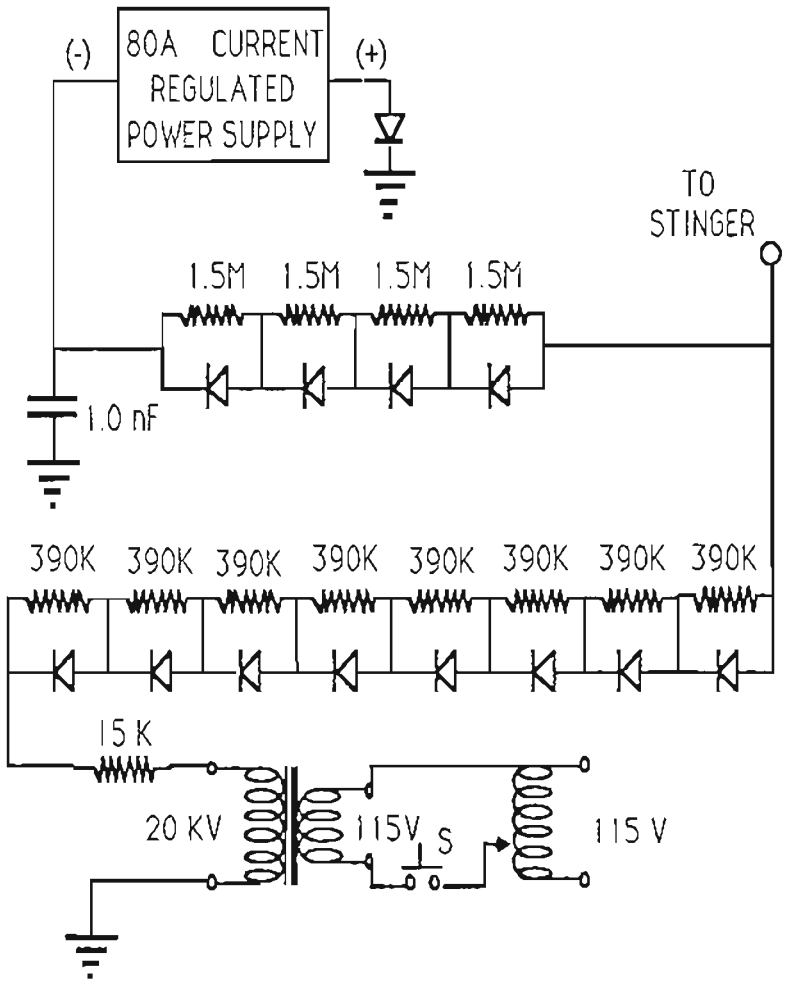

FIG. 5: Schematic of arc initiator circuit for use in floating zone melting apparatus.

C. PROCEDURE

When the sintered rod, seed crystal and stinger are positioned, the bell jar is lowered over the zone melter and the system is evacuated to a pressure $<5 \times 10^{-6}$ torr using the system's oil diffusion pump. The system is kept at this pressure for 15 minutes and then backfilled with an inert gas to a pressure of one atmosphere. With the stinger near the seed crystal, an arc is ignited. The sintered rod is raised and the current increased to form a molten zone, suspended by surface tension between the two vertical rods. (see Fig. 4)

The stinger drive is then activated and the molted zone is carried down along the length of the sintered rod. If the travel rate is slow enough and proper adjustments are made during the length of travel to keep the zone stable and intact, a single crystal sample is produced. Optimum adjustment of the variables is important in obtaining consistent results. These variables have been carefully investigated, as well as the effect these variable have on the stoichiometry of the final product.

All samples used experimentally were zone melted with one pass. While several passes would improve purity, it would also reduce the carbon levels. Since purity was not deemed to be a problem, zone melting was confined to a single pass to preserve stoichiometry.

D. VARIABLES

Various parameters have been adjusted in an attempt to optimize the zone melting procedure. The objectives are: a) the zone melted piece must be a single crystal, b) the stoichiometry should not drastically change through the specimen's length, and c) no impurities should be added during the process.

The three objectives are functions, respectively of: a) stinger speed, temperature and stability of zone which in turn is directly related to stinger material and shape, b) initial stoichiometry, evaporation rates of each component and, possibly, speed of zone travel, and c) initial impurities present, impurities introduced from the atmosphere and possibly zone temperature and speed.

In an effort to optimize the dependent variables (crystallinity, stoichiometry and purity) various adjustments of the independent variables were made and their effects noted.

i) Stinger Speed

The calibration and adjustment of this parameter was straight forward. A chart was made (see Fig. 6) which gives the stinger speed in centimeters per hour as a function of belt position and variac (motor speed) setting.

During the initial attempts at zone melting, speeds of 50-60 cm/hr

were used. These proved too fast for good single crystal growth. While later experiments were made at 2 cm/hr, most zone melting is now done in the range of 10-30 cm/hr. This speed seems adequate for growth of single crystals of the diameters used (1-3 mm).

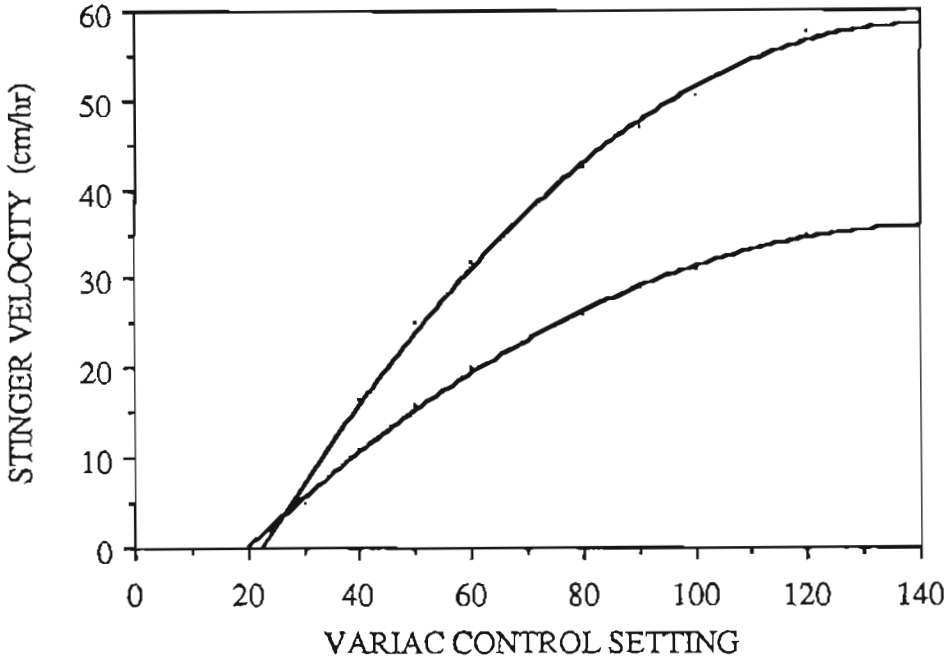

Fig. 6: Calibration curve for zone melt travel speed, as a function of variac setting. Two curves represent different belt positions on drive mechanism.

ii) Temperature

The melting temperature is an indication of the position on the phase diagram. Enough arc current must be supplied to increase the temperature to the melting point. Any additional current tends to

evaporate more material from the zone (especially in the case of HfC) and enlarges the zone to the point of zone melt-through. Thus the optimum current and therefore temperature, is that which just gives a complete molten zone through the stock. At this power input the temperature for a molten zone is approximately 2850 C for ZrC. (see Fig. 3)

iii) Stinger Material

As well as being dependent upon temperature, zone stability is a function of stinger material and shape. Materials tested as stingers were carbon, tungsten, thoriated tungsten, tantalum, sintered stock and previously zone melted material. Consistently the best results have been achieved using sintered stock of the same material and diameter as that being zone melted.

Stinger end-shape plays a key role in the ability to keep a stable arc needed for proper crystal growth. The natural end form is a molten sphere. While we are unable to change this we can, to some degree, adjust the size and hence stinger stability. We have found that filing or grinding the sintered stinger end to a conical or pyramidal form yields an equilibrium end form stable enough to last throughout one pass. The stinger needs to be reformed prior to each run to give a stable arc.

iv) Atmosphere

The atmosphere used, and the vacuum achieved, prior to backfilling relate directly to stoichiometry and purity. To ensure purity a pressure of $<5 \times 10^{-6}$ torr is developed before backfilling. The inert gas used is standard purity (99.9+ %) bottled gas. The vacuum and gas purity are thought to be adequate to preserve sample purity.

Argon has been the primary gas used in our zone melting. The species of inert gas used, however, directly affects the evaporation rates and the power requirement. To investigate this phenomenon, four gases were used and compared: Ar, He, Ar/He 50-50 and 75-25 mixtures.

E. RESULTS AND DISCUSSION

While using helium, it was first noted that a piece could be zone melted using less current, but more power than with an argon atmosphere. A controlled experiment resulted in the following data. (see Table II)

Table II: Comparative Power Requirements

(Sample size: 0.041x0.048 inch $ZrC_{1.5}$)

Gas used:	Ar	Ar/He	He
Voltage/Current:	15 V/11.5 A	17 V/11.5 A	22 V/10.25 A
Power:	172.5 W	195.5 W	231 W

The differences in voltages can be explained by the ionization potentials, I, which are shown in Table III. The reason for the difference in power requirements is the variation of thermal conductivity, K, of the gas. These are also listed in Table III, which includes the ionization potentials and thermal conductivities of other inert gases for comparison.

Table III: Ionization Potentials and Thermal Conductivities for Various Gases[2]

Gas	Ionization Potential (eV)	Thermal Conductivity (mW/cm- K)	
Argon	15.76	0.162	(at 270 K & 1 atm.)
Helium	24.58	1.411	"
Neon	21.56	0.461	"
Krypton	14.00	0.086	"
Xenon	12.13	0.0514	"

Another dramatic difference in using helium over argon was the type and consequences of the crystalline growths that occurred on the end of the stinger during zone melting. Certain of these growths are undesirable because they tend to cause instabilities in the arc. Two types of growths were typical and are identified below. (see Fig. 7)

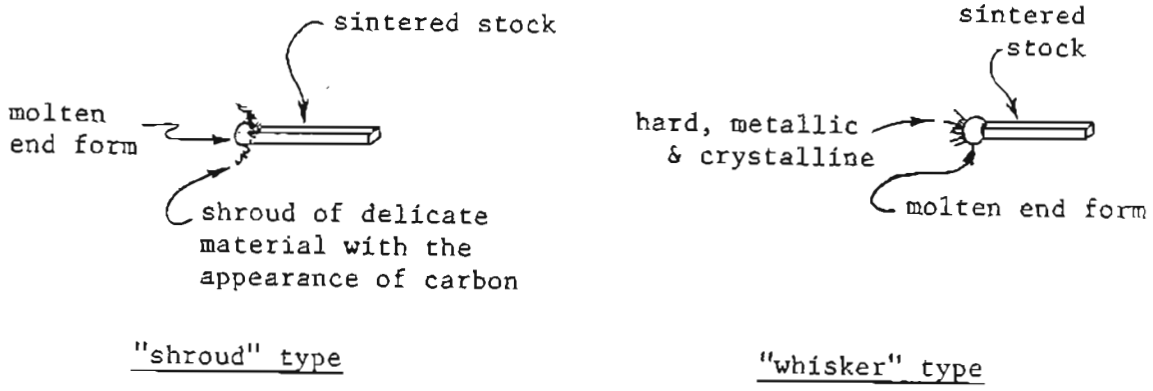

Fig. 7: Evaporative products from zone melting.

While there is some of the "carbon shroud" material present with the argon atmosphere, much more material and of both types is present with the use of helium. To explain this phenomenon, we need to examine the mechanism of evaporation of ZrC (Zr or C) given an inert gas at one atmosphere pressure.

Evaporation is the escape of an atom or molecule (in our case Zr, C, or ZrC) entirely away from the molten zone. The physical presence of the inert gas retards this escape by simple collisions. An atomic gas (or plasma) can be characterized by the average mean free path L, which is given by

$$L(v) = \bar{v}\tau(v) \qquad (1)$$

where $\bar{v}$ is the average speed and τ=t the mean time between collisions.

The total scattering cross section, for collision of two molecules, assuming two hard spheres, is given as (see Fig. 8),

$$\sigma_o = \pi(a_1 + a_2)^2 \qquad (2)$$

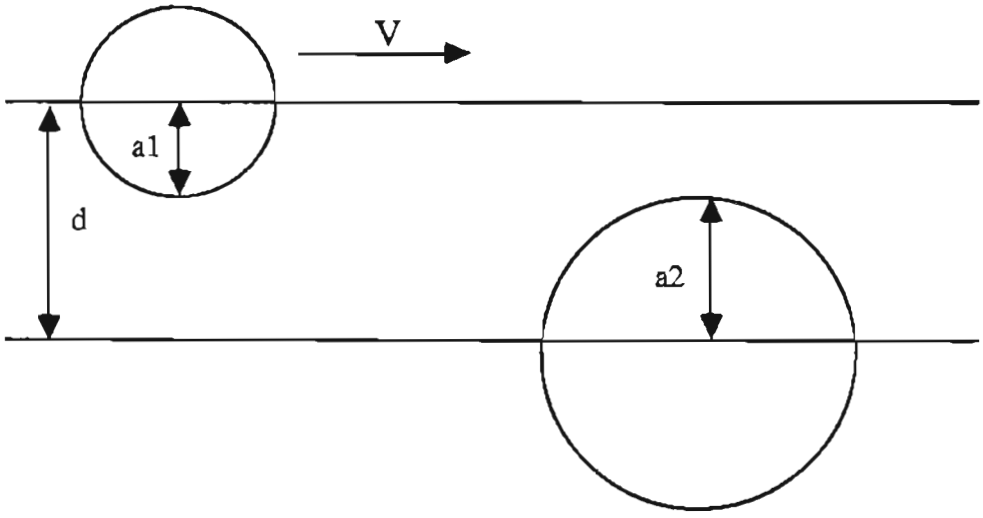

Fig. 8: Total scattering cross section. If spheres were congruent, then $\sigma_o = \pi d^2$, where d is the diameter of the spherical particle.

With n being the mean number of molecules per unit volume

$$\tau = \frac{1}{\bar{V}\sigma_o n} \tag{3}$$

and

$$L = \frac{\bar{v}}{\bar{V}} \frac{1}{n\sigma_o} . \tag{4}$$

For two different particles

$$\bar{V} = (v_1^2 + v_2^2)^{1/2} \tag{5}$$

As an approximation we assume similar type particles, then

$$\bar{V} = 2^{1/2}\, \bar{v} \tag{6}$$

and the mean free path becomes

$$L \simeq \frac{1}{2\pi nd^2} = \frac{0.225}{nd^2} = \frac{9.375 \times 10^{-21}}{d^2} \quad \text{(cm)} \quad (7)$$

since

$$n = \frac{P}{kT} = 2.4 \times 10^{19} \text{ molecules/cm}^3. \quad (8)$$

The evaporation rate can be assumed directly proportional to the mean free path, and is therefore inversely proportional to the square of the atomic diameter. Listed in Table IV are the approximate atomic diameters for the constituents of the gas, as well as others listed for comparison.

Table IV: Approximate Atomic Diameters for the Appropriate Elements

Atom	d (Angstroms)	Atom	d (Angstroms)
Argon	1.88 - 1.91	Hafnium	1.6
Helium	0.53	Krypton	2.0
Carbon	0.91	Neon	1.6
Zirconium	1.6	Xenon	2.2

These rough figures demonstrate the benefits of the use of argon for the inert atmosphere in our arc zone melting procedure. To keep the evaporation rate constant a pressure of approximately 12.8 atmospheres of helium would be needed in comparison with that of 1 atmosphere when using argon.

An alternate method can be used to explain the rate of evaporation of the various components in the system surrounding the molten zone. The rate of evaporation will be controlled by the rate of diffusion of the evaporant into the surrounding inert gas. The physical presence of the inert gas can similarly by thought to retard this escape through momentum exchange during collisions.

Assuming that evaporation is limited by diffusion, one may investigate the effects of different inert gas atmospheres on the rate of evaporation by using a simplified one-dimensional model of the evaporation process. The appropriate equations describing the diffusion of evaporant A through a gas B are Fick's first and second laws:

$$J_n = -D_{AB}(dn/dx), \tag{9}$$

$$\partial n/\partial t = D_{AB}(\partial^2 n/\partial x^2) \tag{10}$$

where J_n is the number flux density of atoms A leaving the liquid surface in number per unit area per second; n is the number density of atoms of type A in the region outside the liquid surface; and D_{AB} is the diffusion coefficient for atoms of type A diffusing into a gas atmosphere of type B, in units of area per second. Under steady state conditions, Eq. (10) leads to the conclusion that the gradient of the number density is a constant.

Using a hard sphere kinetic theory model,[6] one obtains the following

expression for the diffusion coefficient:

$$D_{AB} = (kT/\pi)^{3/2}(1/m_A + 1/m_B)(1/[3P(R_A + R_B)^2] \quad (11)$$

where m_A and m_B are the masses and R_A and R_B are the atomic radii of the two constituents, k is the Boltzmann constant, T is the temperature and P is the total pressure. The flux may be expressed as

$$J_n = \frac{K(P,T)(1 + m_A/m_B)}{m_A R_A^2 (1 + R_B/R_A)^2} \quad (12)$$

where K is a function of P and T. A comparison of

$$J_n m_A R_A^2/K(P,T) \quad (13)$$

for evaporation of both carbon and zirconium in the inert gases is presented in Table V.

The data appearing in Table V predict that the rate of vaporization is greater for a helium atmosphere than for an argon atmosphere. They also suggest that the rate of vaporization of carbon relative to zirconium is greater for the argon atmosphere. If this were true, one would expect a lower final stoichiometry for specimens melted in argon. That the rate of evaporation is greater for helium than argon is borne out by experiment but, as discussed below, there is not clear evidence that the stoichiometry of the zone melted specimen is different for the two gases.

TABLE V: Specific vaporization rates, $\{[J_n m_A R_A^2]/K\}$, for carbon and zirconium in different inert gas environments, B.

ELEMENT	GAS	R_B(A)	m_B(amu)	R_A/R_B	m_A/m_B	$[J_n m_A R_A^2]/K$
Carbon						
	Helium	0.53	4	0.76	3.0	1.29
	Neon	1.6	20	2.29	0.6	0.15
	Argon	1.9	40	2.71	0.3	0.094
	Krypton	2.0	84	2.84	0.14	0.077
	Xenon	2.2	131	3.14	0.092	0.064
Zirconium						
	Helium	0.53	4	0.34	22.75	13.22
	Neon	1.6	20	1.03	4.55	1.35
	Argon	1.9	40	1.22	2.28	0.67
	Krypton	2.0	84	1.29	1.08	0.40
	Xenon	2.2	131	1.42	0.70	0.29

From the preceding discussion, it might be concluded that in every respect argon is superior to helium as an atmosphere for arc induced zone melting. There is, however, one problem arising from the use of argon which seriously affects its suitability. This is the problem of arc instability which is more pronounced in the case of argon than helium. As mentioned above, arc stability is crucial because of its effect on the quality of the crystals grown by this method. In order to optimize the various parameters involved in the arc induced zone melting process, two argon/helium gas mixtures (50% Ar - 50% He and 75% Ar - 25% He), as well as pure argon and pure helium were investigated. From these studies, it was concluded that the gas mixtures provide essentially the same arc stability as pure helium, while their ability to suppress evaporation is as effective as pure argon. With the exception of power requirements, no significant differences in results were detected between the two mixtures.

The results of the series of runs using the four different gases or gas mixtures are presented in Table VI. (The stoichiometry of the sintered stock was 0.989.) The carbon analyses used in making the stoichiometry determinations were performed in the analytical laboratory of Teledyne Wah Chang (Albany, Oregon, U.S.A.). There are no statistically significant differences in the stoichiometries of the zone melted specimens. There is, however, a greater range of values exhibited for argon than for the other gases, due to problems associated with the instability of the argon arc.

TABLE VI: Summary of data for specimens zone melted in various argon-helium mixtures.

Gas	Sample NO.	Area sq. cm	Voltage V	Current A	Power watt	P/Area watt/cm	x
100% Ar	180	0.024	11.2	31	347	14.4	0.902
	182	0.019	11	25.7	282	14.8	0.94
	192	0.028	11.9	36.8	438	15.6	0.93
	192B	0.029	11.5	39.7	456	15.7	
	194	0.013	11.5	21.5	247	19	0.91
	AVERAGE		11.4±.3			15.9±.2	0.92
75% Ar-	183	0.016	12.2	20.8	254	15.9	0.92
25% He	184	0.013	12.5	19.2	240	18.5	0.93
	185	0.014	12.3	17.1	210	15	0.93
	193	0.047	12.5	50.1	636	13.5	0.94
	AVERAGE		12.4±.2			15.7±.2	0.93
50% Ar-	189	0.013	14.5	18	261	20.4	0.93
50% He	190	0.035	12.8	37.2	476	13.6	0.93
	191	0.026	13.2	29.6	391	15	0.93
	AVERAGE		13.5±.2			16.3±.4	0.93
100% He	186	0.015	19	17.8	338	22.5	0.93
	187	0.014	18.9	16.8	318	22.7	0.91
	188	0.016	16.4	19.3	317	19.8	0.94
	AVERAGE		18.1±.2			20.8±.2	0.93

IV. STOICHIOMETRIC ANALYSIS

A. CHEMICAL METHOD OF ANALYSIS

While all of the zirconium carbide samples were analyzed at other facilities, an attempt was made to do the analysis in-house. (Samples were analyzed at either the U.S. Bureau of Mines, Albany, Oregon facility, or at Teledyne Wah-Chang Analytical Laboratory, also in Albany.)

The method of analysis was to combust the zirconium carbide sample in a flow of oxygen, then collect the evolved carbon dioxide and make the stoichiometric determination from this data. The process is given as

$$ZrC + 2O_2 \leftrightarrow ZrO_2 + CO_2.$$

The carefully weighed sample of ZrC, typically 0.1-0.3 grams, was placed in a quartz combustion boat. This in turn was inserted into a quartz combustion tube in a tube furnace. Ground glass ball joints were used to facilitate the hook-up to the rest of the system which was made of pyrex glass. Oxygen was blown over the sample at a flow rate of 10 ml/min. at a furnace temperature of 650-900 C. (Temperature requirements varied depending upon whether the ZrC sample was sintered or crystalline.) The evolved carbon dioxide was adsorbed in a previously weighed ascarite filled tube. (Ascarite is composed of asbestos pellets coated with sodium hydroxide.) The reaction with

ascarite is described by

$$CO_2 + 2NaOH \rightarrow 2Na^{++}CO_3^{--} + H_2O.$$

Once the combustion had been completed, the ascarite tube was again weighed along with the ZrO filled quartz combustion boat. (see Fig. 9). From the data collected, the stoichiometry of the original sample was calculated.

Multiple runs were made on samples of sintered ZrC, crystalline ZrC, and, for calibration purposes, on pure carbon. Table VII lists the data collected. The data for the crystalline ZrC has been omitted due to the poor results obtained. The reason for this was that the combustion of the crystalline material was very slow and proceeded only at the very upper temperature limit of the tube furnace used.

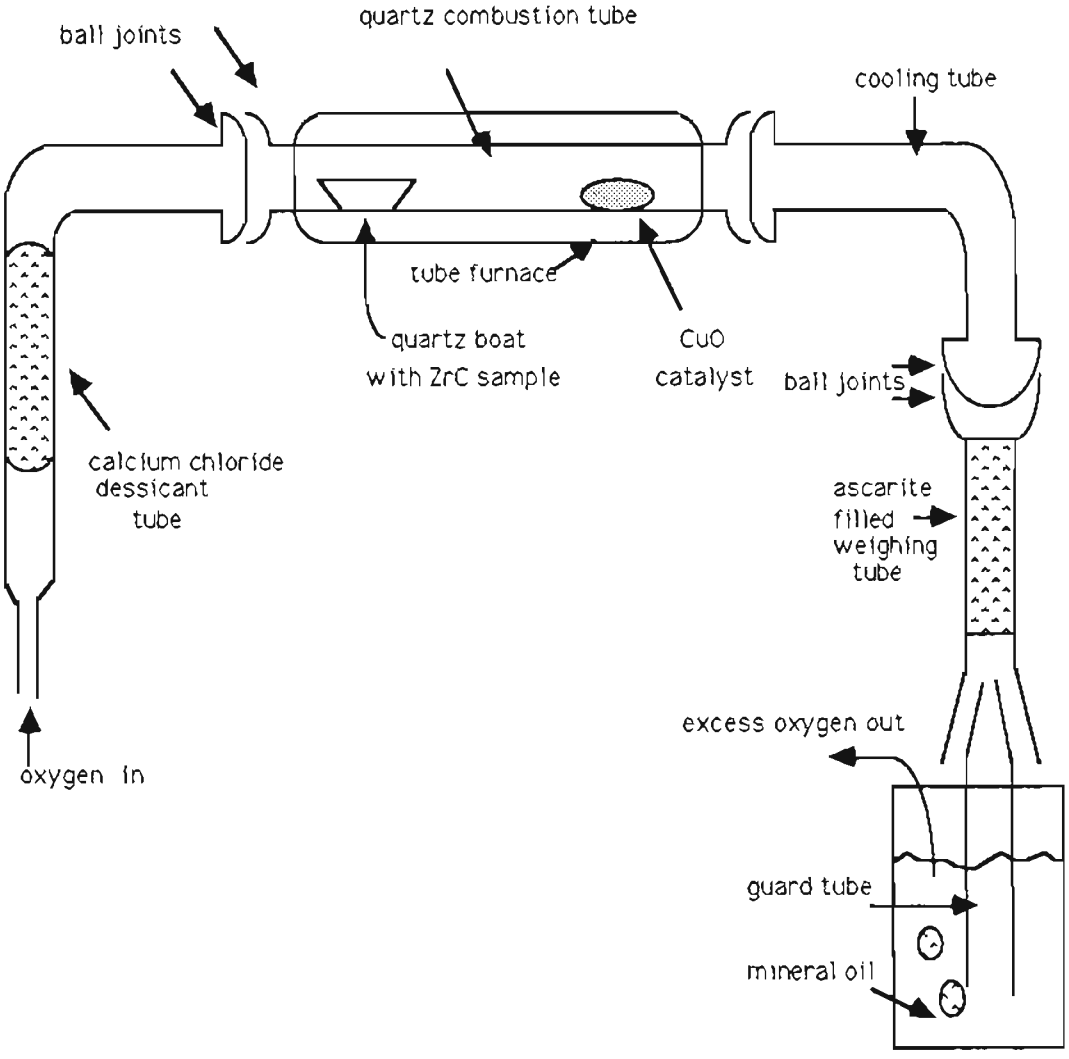

Fig. 9: Experimental apparatus used for stoichiometric analysis.

Table VII: Data Resulting from In-house Stoichiometry Determination of ZrC.

Compound Analyzed	Pre-analyzed Composition	Trial	Experimental Results
Sintered ZrC (#1)	$ZrC_{0.94}$	1	$ZrC_{0.871}$
		2	$ZrC_{0.882}$
		3	$ZrC_{0.894}$
Sintered ZrC (#2)	$ZrC_{0.98}$	1	$ZrC_{0.941}$
		2	$ZrC_{0.936}$
		3	$ZrC_{0.901}$
		4	$ZrC_{0.924}$
		5	$ZrC_{0.940}$
Pure Carbon	99.999%	1	97.90%
		2	92.07%
		3	96.70%
		4	93.60%

TABLE VII: (continued)

DATA ANALYSIS

Compound	Experimental Value	% Difference
$ZrC_{0.94}$	$ZrC_{0.889}$ (st.dev. 0.006)	5.4%
$ZrC_{0.98}$	$ZrC_{0.926}$ (st.dev. 0.040)	5.5%
Carbon	Carbon	
99.999%	95.07%	4.9%

As can be seen from the data, the values calculated were consistently off by approximately five percent. It seems apparent that carbon is being lost from the system. This could happen either by leakage of carbon dioxide, or by the generation of carbon monoxide instead of the desired carbon dioxide. The latter event would give a false reading due to the fact that ascarite does not adsorb carbon monoxide. Cupric oxide was added to the combustion tube to enhance the conversion of carbon to carbon dioxide but, from the experimental results, the addition of this oxidizer did not improve the accuracy significantly. There was marked improvement of accuracy when the ascarite was changed with each trial, but in none of the trials did the accuracy improve to acceptable values.

The conclusions from these trial experiments only point to

modifications in the hope of improving the accuracy. Since outside analysis was available, further work was not carried out. However, possible improvements might include:

1) The ground glass joints may leak. A better more efficient method of sealing the combustion tube needs to be devised.

2) Perhaps the volume of ascarite needs to be increased to ensure that all the carbon dioxide generated has a chance of being adsorbed.

3) A better catalyst could be tried. Instead of the cupric oxide, perhaps platinum wool should be used.

4) Finally, at combustion temperatures above 1000 C carbon is converted to carbon monoxide, not carbon dioxide. To help keep temperatures lower, perhaps a finer powdering of the crystalline samples would help.

B. STOICHIOMETRIC VALUES FOR VARIOUS SAMPLES USED

Contained in Table VIII are the compositions obtained for the various samples used throughout this research. Initially the material used was that as supplied by Demetron (later to become Degussa), which had a C/Zr ratio of 1.5. This caused some trouble because this ratio was much too high. Values for the material sintered in-house, as well as for the material more recently received from Degussa are included.

In addition, values for various samples of zone melted material are listed and compared. The experiment in which the particular sample was used is also indicated.

TABLE VIII: Chemical Analysis of Sintered Stock and Zone Melted Material

	Atomic %				C/Zr
	Zr	C	Hf	Si	Ratio
Sintered Stock (Demetron)	81.1%	16.0%	0.05%	0.26%	1.495
Zone Melted 1-pass (Dem.)	86.4% (ave.)	13.6% (ave.)	---	---	1.2 (ave.)
Stock for Sintering (Wah C.)	88.2%	11.5%	<0.04%	0.44%	0.990
Zone Melted 1-pass (Wah C.)	89.2% (ave.)	10.8% (ave.)	---	---	0.92 (ave.)
HfC Sintered Stock	1.6%	6.4%	91.3%	0.45%	1.04 C/Hf
Sintered Stock	88.4%	11.6%	---	---	0.982
(Degussa BLK L095K01)	88.5%	11.5%	---	---	±0.005
Zone Melted ZrC (#152)	89.5%	10.5%	---	---	0.896
used for thermionic work	89.4%	10.6%	---	---	±0.005
ZrC Single Crystal Platelet	89.3%	10.7%	---	---	0.91
FERP/AES sample					
TiC Single Crystal Platelet	---	19.0%	89.0% Ti	---	0.9355
FERP/AES sample					
ZrC 2.5 mm Diameter Crystals	89.1%	10.9%	---	---	0.925
used for emissivity measurements	89.2%	10.8%	---	---	±0.005
Sintered Stock (Degussa)	88.6%	11.4%	---	---	0.977

PART TWO: SURFACE ANALYSIS AND WORK FUNCTION STUDIES

I. EXPERIMENTAL SPECIMEN PREPARATION

A. SPECIAL CONSIDERATIONS FOR ZIRCONIUM CARBIDE

Because of the special physical properties exhibited by the transition metal carbides, they require special treatment. In some instances, new techniques had to be developed to circumvent problems arising from some negative attribute. For example, the common method of mounting a fine wire to a heating filament for use as a field electron emitter is that of spot welding. This simple task is thwarted by the extreme brittleness of these carbides. The thermal shock involved in the spot welding process is enough to shatter the carbide wire sample. Other means needed to be developed.

The effect of stoichiometry and impurities can have marked effects on the surface electronic properties. Zone melting, in general, tends to remove impurities. However, the carbides can dissolve a considerable amount of oxygen.[1] This can occur when the C/Zr ratio is less than one and happens by direct substitution in the lattice at the carbon vacancies. When ZrC is exposed to oxygen it can remove carbon in the form of CO.

$$O_2 + C_{\text{in zrc}} \leftrightarrow ZrO_{\text{in zrc}} + CO$$

In general, any operation involving these carbides needs to be reviewed in light of their special properties. Mounting methods, etching solutions, and heating procedures all needed to be modified.

B. MOUNTING METHODS

i) Field Emission Cathode Mounting

Since spot welding of emitter blanks to heating filament loops is not feasible for carbide materials, other methods were needed. The requirement is the ability to heat the emitter quickly and to a high temperature. Many methods were tried with varying degrees of success.

1) Tantalum Wire/Brazing

The first method used with some success, was to use a filament of 0.005-0.010 inch tantalum wire wrapped around the emitter shank and brazed into place. The optimum method was to wrap two filaments around the emitter shank, each filament being wrapped around the shank once. The method is similar to that depicted in Fig. 10, except only one multiwrap filament was used in that instance.

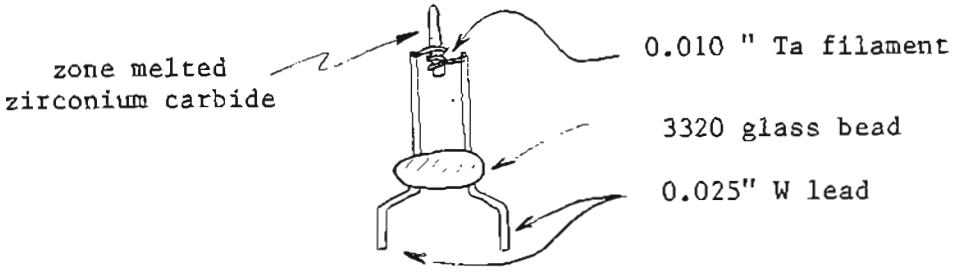

Fig. 10: Emitter blank assembly.

The double filament did necessitate using a higher current for heating, but the temperature attained was higher than through the use of a single filament wrap.

In order to maintain good thermal contact, a braze was needed. Initial attempts utilized tungsten carbide for the brazing material. However, brazing in a quick change system failed to work due to high 10 x 10^{-5} torr pressure and glow discharges. Two tips were mounted on flanges and put on a mercury diffusion pumped vacuum system. Tungsten filaments (0.010") were used to mount crystal blanks instead of the preferred, malleable tantalum filaments. After evacuating to <5 x 10^{-7} torr, melting of the braze was accomplished using ~70 watts of electron bombardment power.

While this worked, it required very high temperatures, along with the need to use the diffusion pumped vacuum system, and emitter blanks were therefore slow to process. Due to these considerations as well as the fact that the Ta withstands the tip etchant solution much better than does the W, an alloy braze was used.

The Ta-Co braze is interesting and very useful. These elements form an alloy which disassociates at a temperature of around 1500-1700 C, thus leaving a high temperature braze of Ta only. The Ta-Co alloy braze flows at a relatively low temperature and forms a high temperature braze when the Co has evaporated. The technique which seems to be the most convenient is to add the braze powder (Ta-Co alloy with TaC filler added) to the etched and micrographed emitter just prior to mounting the

flange in FEM tube for evacuation. Then, when the system has been evacuated and baked, the braze is melted and the Co evaporated the first time the emitter is heated. This is done carefully with inspections made to ensure proper brazing. This method has been employed repeatedly with great success.

One adversity however, was encountered with this technique. During the initial heating to evaporate the cobalt, it was occasionally found that before the Co evaporated it would dissolve the Ta filament or at least etch it so badly that it would later burn out. To prevent this, it was learned that the braze alloy needs to be heated to 1600 C for an extended period of time (> 10 minutes) to ensure complete evaporation of the Co. Only then is the braze strong to high temperatures.

2) Vogel Type Mounting

Since occasionally the Ta filament burns out in the previously described mounting technique, other methods were also investigated. The Vogel mount method of holding an emitter uses the tension between two fixed Ta supports with the insertion of two pyrolytic graphite pillows sandwiching the ZrC. The graphite pillows are needed to heat the crystal when a current is passed through the supporting Ta. (see Fig. 11)

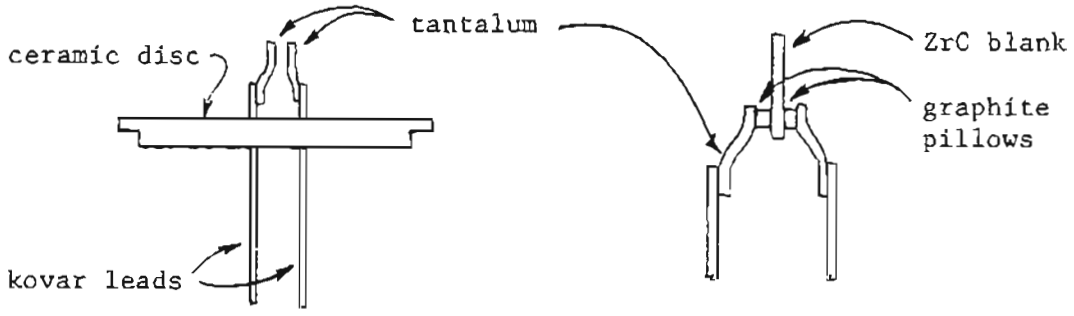

Fig. 11: Initial Vogel type mount.

The Vogel mount was initially quite successful. The emitter could be heated quickly to high temperatures. However, extended heating at an elevated temperature (1800-2000 C) resulted in separation of one of the pyrolytic carbon pillows from the Ta support, which happened upon cooling. Evidently the heat relieved the tension in the Ta and/or kovar leads and the expansion due to heating caused the separation.

Since initially this system seemed to work in giving higher heating temperatures, another configuration was assembled and tested. (see Fig. 12)

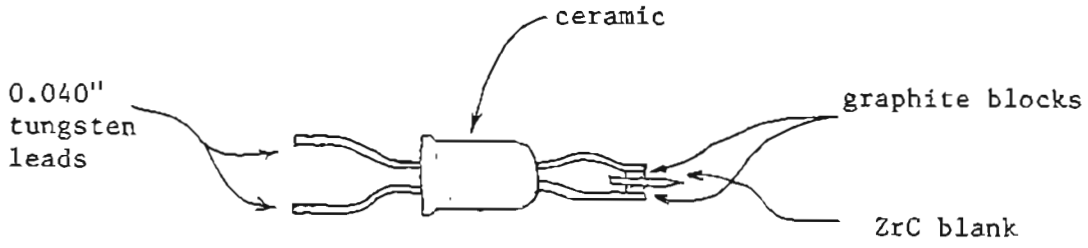

Fig. 12: Design of improved Vogel type mount for emitter heating. The W supports and the emitter shank are ground parallel to facilitate mounting with the flat sided carbon blocks.

Due to the delicate nature of an etched emitter, the emitter blanks were mounted and then etched. A special jig had to be constructed so that during etching, the etching current would not pass through the carbon pillows. In some of the previous attempts this current was enough to heat and oxidize the carbon, when allowed to pass through them during etching.

This new mount was tried, again with mixed success. The ability to quickly heat the emitter to very high temperatures without undue heating and outgassing of the supports and related tube parts was excellent. However, during a heating to 2000 C for an extended period the supports

separated irreversibly upon cooling. The supports were not very hot (very dull red) but evidently were warm enough to relax the tension in the W supports.

This type of mount is relatively easy to use and does heat an emitter up quickly. However, its utility is limited in its ability to withstand prolonged heating at very high temperatures.

3) Electron Bombardment Heating

In an attempt to enable heating to high temperatures (>2000 C) an electron bombardment set-up was tried. The emitter blank was inserted into a shallow hole in the end of a 0.050" dia. Mo rod. The emitter blank was brazed in place with Co-Ta alloy, heated via electron bombardment in a quick-change vacuum system at 5×10^{-6} torr. A spiralled W filament was looped at a distance around the emitter shank and the entire assembly was mounted on a flange.

The results of this method of heating were good. Quick heating to very high temperatures could easily be achieved. However the braze alloy evidently was heated too hot before all of the Co had evaporated, and the emitter shifted in its Mo holder and shorted with the bombardment filament. Further design modifications were made and the system was tried again, however an even better method of holding emitters was found and is described next.

4) Tantalum/Rhenium Cups

The use of Ta or Re vapor deposited cups for holding the end of the emitter shank (see Fig. 13) proved to be the best method tried for mounting. While Re cups with a Re filaments were tried, the Ta cup with a Ta filament has been used the most, because it is inert to the electrochemical tip etching solution.

The cups and mounting procedures are fully described in the next section. This sample mounting system has been used extensively with both field emission and thermionic emission specimens. If the braze is set (Co evaporated) correctly, the filament and cup assembly can withstand repeated heating to high temperatures.

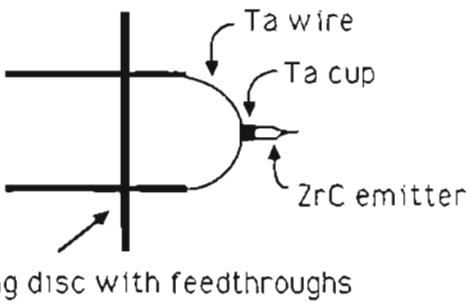

Fig. 13: Field emitter mounting assembly using Ta cups.

ii) Thermionic Cathode Mounting

1) Effective Thermionic Work Function Samples

Square sintered rods (0.060" x 0.060" x 4") produced zone melted crystalline rods with diameters of 0.050 to 0.055 inches. Crystals of random orientation or seeded (100) oriented rods were produced with single crystal lengths of from 0.25 to >1 inch. These rods were broken along crystal boundaries or cleavage planes to approximately one inch lengths and centerless ground to a finished diameter of 0.030 inches to fit the mounting cups. It should be noted that single crystal ZrC is easily cleaved along the (100) crystal plane.

Selection of sample pieces used for the thermionic measurements were made based upon orientation of the cleaved (100) plane in relation to the axis of the ground rod. The first piece mounted had a naturally cleaved (100) plane approximately 30 degrees off-axis. Among the five pieces selected, two had cleaved (100) planes off-axis, one had a [100] orientation on axis but was ground to improve the surface and two had random orientations. The rationale used in selecting the random orientations was to choose pieces with cleaved (100) planes at very roughly a 45 degree angle from the ground rod axis. The desire was to obtain a crystal orientation close to the [110]. Later, Laue analysis showed this selection process to have yielded the [210] and [311] orientations. To ensure orientation to some crystallographic direction,

other than [100], the more difficult process of orienting a seed crystal and zone melting this orientation on axis would be needed.

A small section 0.050 to 0.100 inches in length was removed from each of the five selected ground rods. Stoichiometry was then determined using the remaining piece of ground rod. In addition, stoichiometric determination was made on a typical piece of unground, zone melted rod. The resulting stoichiometries were in agreement with an average C/Zr ratio of 0.896 $\pm$ 0.015, as listed in Table VIII.

The selected small pieces were next prepared for mounting in the 0.030 inch I.D. Re or Ta cups. The first step was to prepare the emitting surface. For two of the samples the emitting surface was used without further preparation. For these two the surfaces consisted of cleaved (100) planes. They were very smooth but their planes were between 25 and 30 degrees off perpendicular to the specimen axis. The other three samples were ground so the emitting surface was perpendicular to the sample axis. The grinding was accomplished by using 600 and finally 1200 grit diamond impregnated wheels, cooled with ethanol.

The second step prior to insertion into the cups was to prepare the other end. This preparation consisted of measuring the proper length, roughly 0.035 inches, grinding the crystal bottom flat and perpendicular to the axis to match the inside of the cup and then chamfering the bottom to facilitate application of the braze material and produce good thermal contact with the bottom of the cup.

In all but one case, Re cups were used to hold the ZrC thermionic specimens. All cups had inside diameters of 0.030 inches and, generally, a 0.008 inch diameter Re heating filament was spot welded to the bottom of the cup. Ta wire 0.011 inches in diameter was used for the Ta cup. In addition, 0.007 inch diameter Re and 0.007 inch diameter Re/W wires were tried. These variations were introduced in an attempt to reach higher temperatures. The cup support filaments were spot welded to the 0.040 inch diameter posts of the base assemblies, as shown in Figs. 14 and 15.

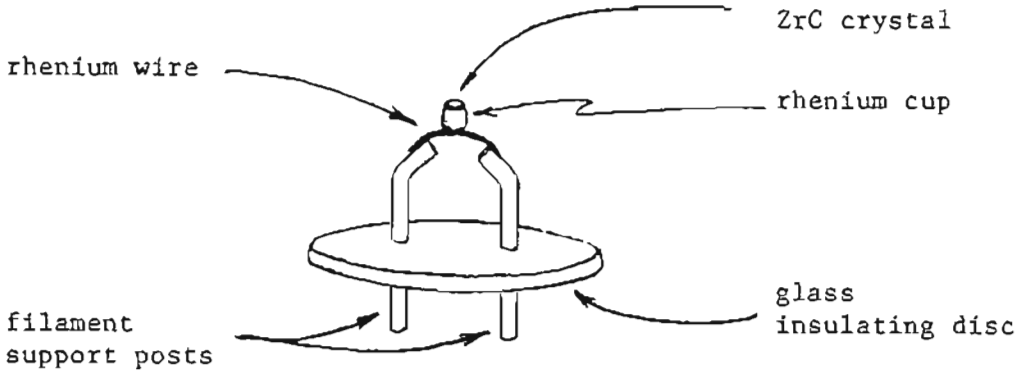

Fig. 14: Base assembly showing configuration of filament, cup and zirconium carbide crystal.

A small amount of powdered Co-Ta alloy was placed in the bottom of the cup, and distributed along the bottom edge. The prepared crystal was then carefully pressed into the cup, with the powdered braze occupying the space formed by the beveled bottom edge of the crystal.

With the ZrC crystal in place, the next step was to set the braze. This was done in a vacuum of <2 x 10^{-6} torr. The temperature of the filament was slowly increased until the braze melted. After a minute, the temperature was further increased to >1600 C pyrometer brightness and held at that temperature for 10 minutes. This process apparently leads to the evaporation of the cobalt from the braze alloy leaving behind a secure, high temperature braze of Ta. (see Fig. 16)

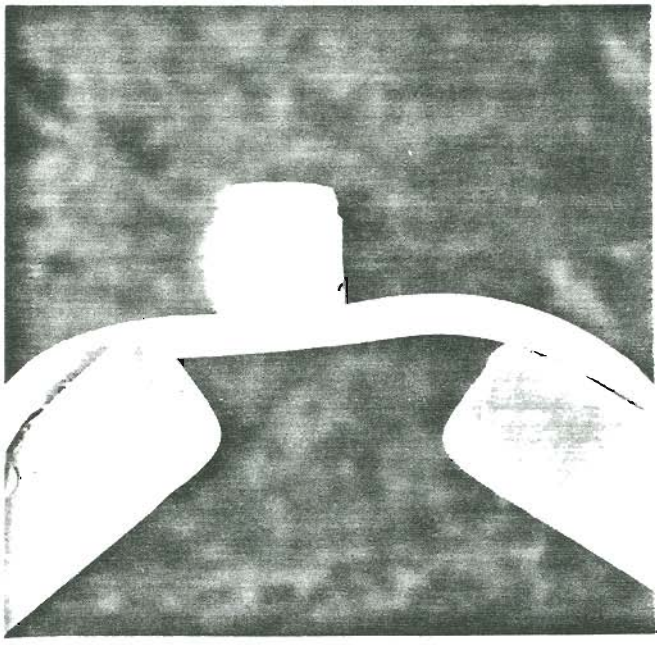

Fig. 15: SEM of ZrC sample #5.

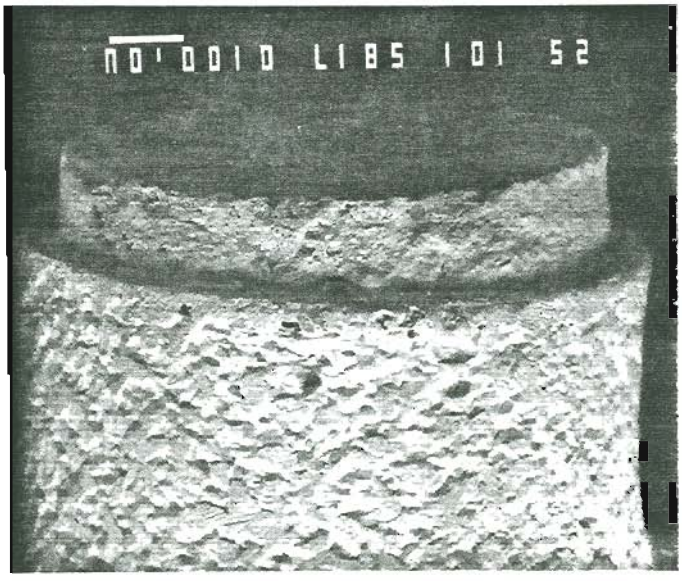

Fig. 16: SEM of ZrC sample #3. Crystal protrudes approximately 0.004 of an inch from the edge of the cup.

2) Hemispherical Samples for the Thermionic Projection Microscope

The single crystal samples used were [100] oriented along the axis, and centerless ground to 0.030 inches in diameter. The specimens were mounted in a jewelers lathe to facilitate forming the end of the rod into a hemisphere.

Grinding was done in steps. First, a 600 grit diamond wheel was used to roughly shape the end while visually inspecting with a 3x binocular microscope. A 1200 grit diamond wheel was hand held to further shape the end hemispherically.

The final steps were to use 15 μm and then 6 μm diamond impregnated mylar. This lapping proceeded with only visual inspections being made to ensure the end conformed to a hemisphere. The shape was relatively easy to obtain, however, the tooling marks were somewhat more difficult to remove. Polishing continued with the finer grits until a very smooth, mirror finish was obtained.

This sample was mounted and brazed in a tantalum cup with a tantalum filament as described in a previous section. This emitter assembly was attached to the tungsten press leads and sealed into the pyrex bulb comprising the tube proper. The tube was in turn sealed onto the pyrex manifold of the mercury diffusion pumped system.

iii) FERP/AES Study Crystal Mounting

Single crystal samples of three metal carbides (TiC, ZrC and TaC) suitable for FERP and AES measurements were obtained.[7] Each crystal had one side which had fractured naturally, presumably along the [100] crystallographic direction. Since the fractured surfaces were deemed smooth enough for AES and work function determination, these specimens were mounted without further surface preparation. (see Fig. 17) Samples of the ZrC and TiC pieces were analyzed and produced C/Metal values of 0.910 and 0.936 respectively.

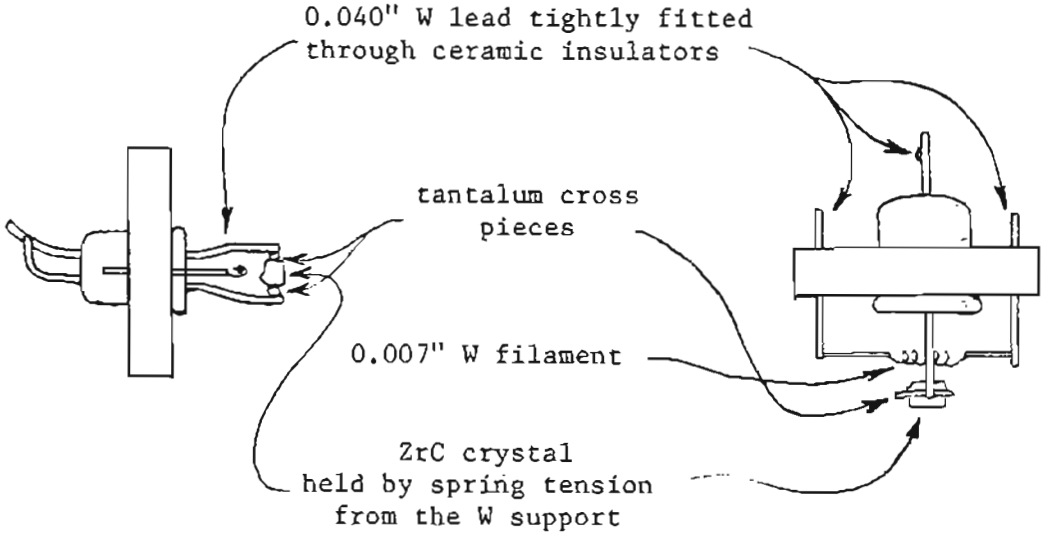

Fig. 17: Typical mounting of macroscopic crystal samples for FERP and AES measurements.

C. SPECIMEN CRYSTALLOGRAPHIC ORIENTATION

A standard configuration was used for obtaining the Laue x-ray diffraction patterns. Verification was easily obtained that the cleaved planes were of a [100] orientation, as in Fig. 18. The other orientations were not always as straight forward (see Fig. 19). Identification of these higher index planes necessitated taking additional Laue photographs at both three and five centimeter working distance (crystal to film spacing), and use of a Greninger chart to plot the axis of zones of planes on a stereographic projection (Wulff net).

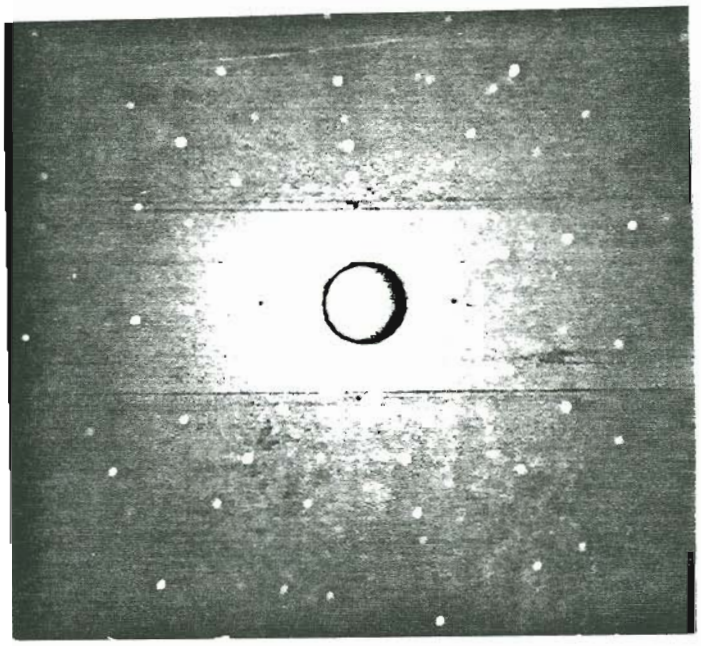

Fig. 18: Laue x-ray diffraction pattern for a cleaved (100) plane of a ZrC crystal.

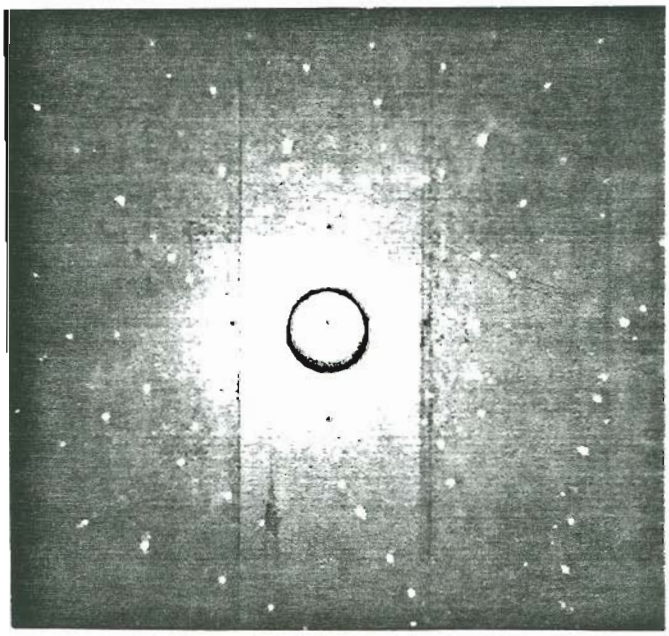

Fig. 19: Laue x-ray diffraction pattern of an approximate (211) ZrC crystal.

D. FIELD EMITTER TIP PREPARATION

i) Etching

The common emitter making process is to electrochemically etch a 0.020-0.030 inch diameter wire to form a small (< 1μm) radius end suitable for field emitting electrons. Many solutions were tried and various parameters, including solution temperature, voltage/current settings, AC vs. DC, and pulsed vs. continuous operation were varied in attempting to gain satisfactory results. The solutions yielding some success are given in Table IX.

Table IX: Carbide Emitter Etching Solutions

Solution A	Solution B
(#'s parts by volume)	
2 - HNO_3	2 - HNO_3
1 - H_2O	3 - H_2O
1 - HCl	0.5 - 0.1 N NaF solution
Trace HF(<5%)	
V = 15-30 v DC	V = 30 v DC
pulsed operation	continuous or pulsed

Solution C

3 - HNO_3

1 - HCl

2 (approx.) - H_2O

25-35 v DC

Continuous operation initially (to remove material),

Pulsed operation just before drop-off.

Solution C has been found to be most successful, and has been used in making all the emitters sharp enough for use. Optimally this solution is kept at constant temperature using a water bath. The cathodes used have been small (≈1 cm dia.) loops of 0.010 inch Ta wire suspended just below the surface of the etchant. The anode is the mounted emitter blank.

ii) Tip Grinding

During the time various emitter solutions were being tried, a different mode of emitter manufacture was attempted. With the use of a modified gemstone faceter, emitter blanks of zone melted ZrC were ground to tip radii ranging from 1.4 to 8 μm. These tips have total cone angles in the 40-50 degree range. (see Fig. 20)

1400 X (r < 7 μm) 140 X 1400 X (r = 9 μm)

Fig. 20: SEM pictures of ground emitters.

The method involved using 1200 (1.8 μm) diamond grit on a 6" steel disc revolving in the horizontal plane with water coolant dripped continuously. An emitter blank was held in pin vise and was rotated with a small battery operated motor, so that at the point of contact the emitter and disc were turning in opposite directions. During this process the tip was viewed with a 3X binocular microscope. The grinding was continued until the emitter "looked sharp". After the 1200 grit grinding the crystal blank was adjusted by increasing the cone angle slightly and then lapping with Raybrite B[8] on a Tin Plate[8] lapping wheel, using the same configuration as before. This additional lapping further reduced the apex radius and removed grit marks.

This grinding method exemplified the fact that the material is

extremely brittle and is easily fractured along the (100) plane. The last 1-5 μm of the tip were easily broken just due to lapping. Increasing the cone angle helped prevent breakage. Also, using finer initial grit alone reduced breakage from excessive pressure during lapping. With use of 50,000 grit (0.5 μm) or 100,000 grit (0.25 μm), tips with radii of < 0.5 μm might be expected, although these grit sizes were not tried because of success in the grinding/etching method described below.

iii) Grinding/Etching

All emitters used to date have been made using the optimum etchant mentioned above, but first the zone melted material was prepared by grinding. Using a centerless grinder with 600 grit diamond paste, zone melted stock 0.5 to 2 cm in length was ground into uniform rods 0.020" to 0.030" in diameter.

These rods were further prepared as follows: a) opposite sides on one end of the shank were flattened, if the emitter was to be held in a Vogel type mount. This was done using a 600 grit diamond wheel on a gemstone faceter and/or b) putting a slight, tapered constriction on the ground rod, to ensure a successful "drop-off" during the electrochemical etching procedure. This tapering was most needed on very short emitter blanks. Longer blanks could usually be etched directly without this ground constriction, by the method next described.

The optimum etching method starts by etching a constriction in the emitter blank. This constriction, which occurs naturally at the level of the solution when the voltage is on, is due to a higher etch rate at the top of the solution level as opposed to below, likely caused by convection currents. Once a definite constriction has been achieved, excess material is etched away from the bulbous portion of the emitter blank remaining below the constriction. The reason is to reduce the weight of the portion that will eventually drop off when the constriction is etched smaller. The final emitter radius is in part a function of the constriction radius at the moment of drop-off.

This method has allowed the consistent production of smoothly shaped emitters in the range of 0.2 to 0.5 μm radius. Figure 21 shows micrographs of ZrC emitters made from Wah Chang stock sintered at O.G.C. The stoichiometric average is $ZrC_{0.92}$. The photos were taken using Linfield's Coates & Welter Field Emission SEM.

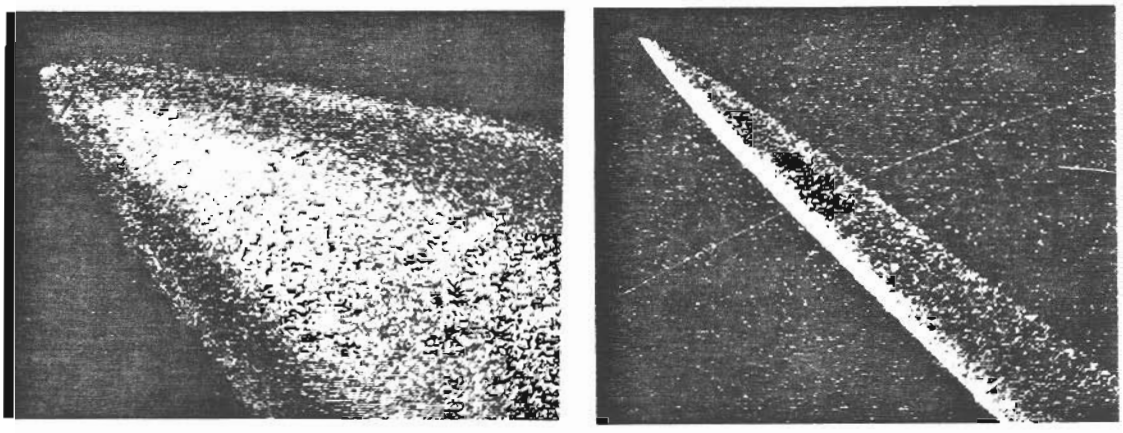

8500 X (0.6 μm) 500 X (0.5 μm)

Fig. 21: Typical etched ZrC field emitters. Magnification (tip radius)

II. EXPERIMENTAL TECHNIQUES AND RESULTS

A. FERP WORK FUNCTION MEASUREMENTS

i) Theoretical Background

The theory behind the work function measurement utilizing the field emission retarding potential (FERP) technique can be easily seen upon examination of Fig. 22. A strong electrostatic field is applied to the surface of the emitter, deforming and narrowing the potential barrier, thus allowing electrons to tunnel through the potential barrier. Electrons are emitted at or near the Fermi level of the emitter. At 0 K, there are no electrons occupying energy levels above the Fermi level, making the emitted electron current highest at the Fermi level, and decaying exponentially with lower energies. For the case of a free electron model, the formula for the differential field emitter current dI_c between the energies of ε and $\varepsilon + d\varepsilon$ ($\varepsilon = E - E_f$) is, in the temperature dependent form,[9]

$$dI_c/d\varepsilon = I_o e^{\varepsilon/d}/[(1 + e^{\varepsilon/pd})d]. \qquad (14)$$

The variable p is equal to kT/d, and d is given by

$$d = heF/2(2m\phi_e)^{1/2}t(y) = 0.976F/\phi_e{}^{1/2}t(y) \quad (eV). \qquad (15)$$

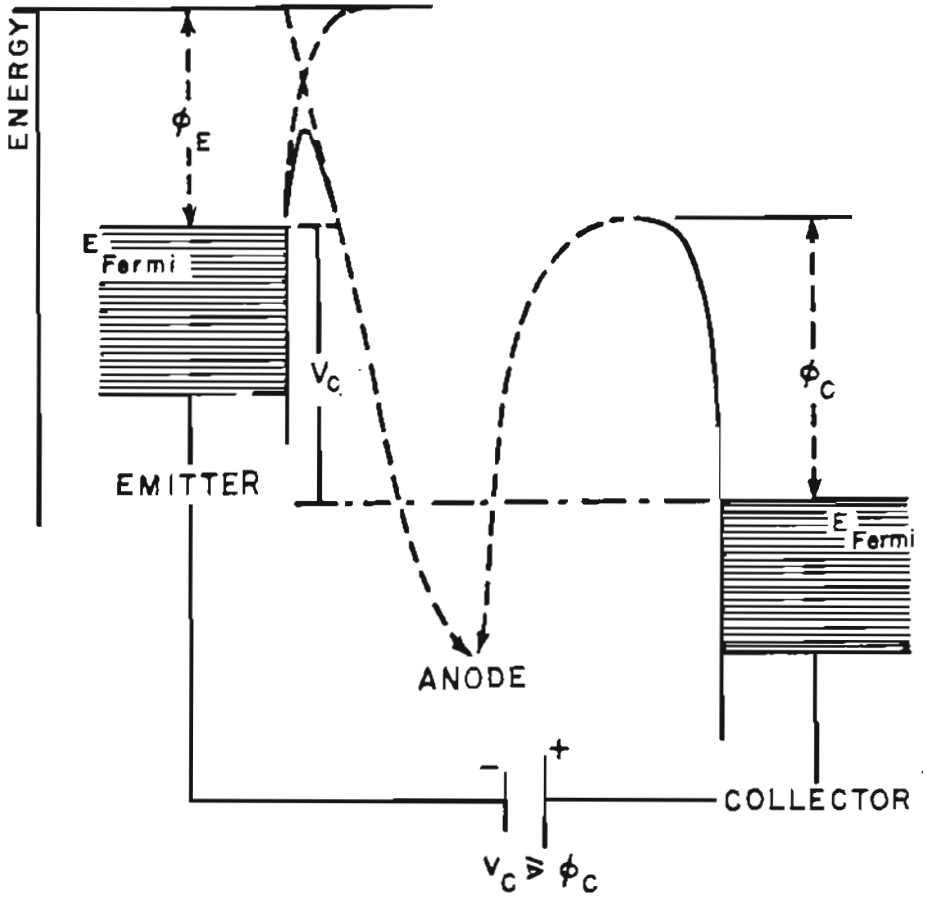

Fig. 22: Potential energy diagram for the field emission retarding potential (FERP) method of determining work function. When bias voltage V_c is applied to the collector in a way that only electrons from the Fermi level of the emitter are collected, then $V_c = \phi_c$.

Here F is the electric field (units V/A), and ϕ_e is the emitter work function (units eV). Through use of the Fowler-Nordheim equation

$$I_o = \{e^3F^2A/[8\pi h\phi t^2(y)]\} \exp[-4(2m\phi^3)^{1/2}v(y)/3heF]$$

$$= \{1.5 \times 10^{10}\ F^2A/[\phi t^2(y)]\} \exp[-0.683\phi^{3/2}v(y)/F]\ (A) \quad (16)$$

the maximum emitted current I_o in Eq. (14) can be found. The variable A, from Eq. (16), is the area of the emitting surface. The functions t(y) and v(y) are image correction terms, slowly varying tabulated functions of the variable $y = (e^3F)^{1/2}/\phi$.

When the emitter and collector are electrically connected, their Fermi levels are aligned. When this is the case, emitted electrons are unable to be collected at the collector's metal surface because of the potential barrier of height ϕ_c, the work function of the metal. When a positive voltage V_c is applied to the collector with respect to the emitter, the collector's potential barrier is lowered. When $V_c = \phi_c$, electrons emitted from the Fermi level of the emitter can just be collected at the metal surface. This condition represents the current cut-off.

For an emitter at 0 K, the value of the total current collected at the metal surface, I_c up to a given value of ε is given by

$$I_c = I_o/d \int_0^{\varepsilon} e^{\varepsilon/d} d\varepsilon = I_o(1 - e^{-\varepsilon/d}). \qquad (17)$$

This equation neglects reflection, i.e., $I_p = I_c$ where I_p is the primary electron beam current. Eq. (17) can be rewritten in a more convenient form:

$$\log_{10}(I_o - I_c)/I_o = -\phi_c/2.3d + V_c/2.3d. \qquad (18)$$

From this, it can be seen that by plotting $\log_{10}(I_o - I_c)/I_o$ versus V_c, ϕ_c can be obtained from the intercept, and d can be obtained from the slope. However, Eq. (18) also neglects any reflection coefficients. This means that it may be invalid for use with certain crystals where high reflection is found.

A more convenient method of determining the collector work function is from the total energy distribution (TED) curves (Figs. 23 and 24). To show how this is accomplished, Eq. (14) is first differentiated with respect to ε, giving ε_p which is the difference in energy between the TED peak and the Fermi energy level:

$$\varepsilon_p = kT \ln[kT/(d-kT)]. \qquad (19)$$

Eq. (19) is plotted in Fig. 25, for several values of d. From this,

ε_p may be found theoretically. Since $\varepsilon_p = \phi_c - V_p$, and V_p may be obtained experimentally as the value of the maximum dI_c/dV_c on the energy axis, ϕ_c can be acquired directly from the TED curve and Fig. 24. The value of ε_p usually is around 30 meV. Using this method gives ϕ_c to within an accuracy of 1%. This method also has greater validity since it is less affected by reflection processes.

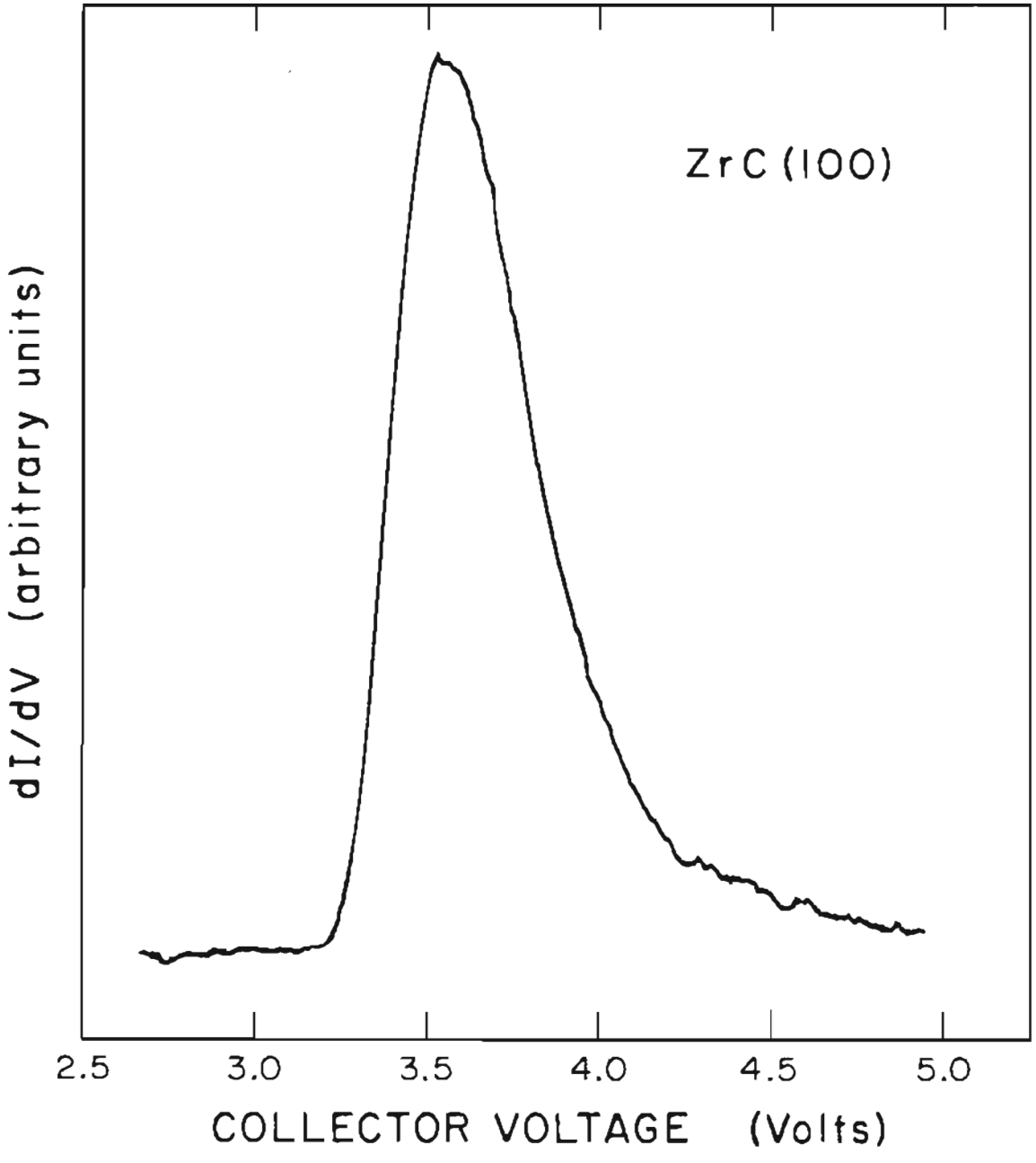

Fig. 23: TED curve for $ZrC_{(100)}$ obtained from the FERP apparatus.

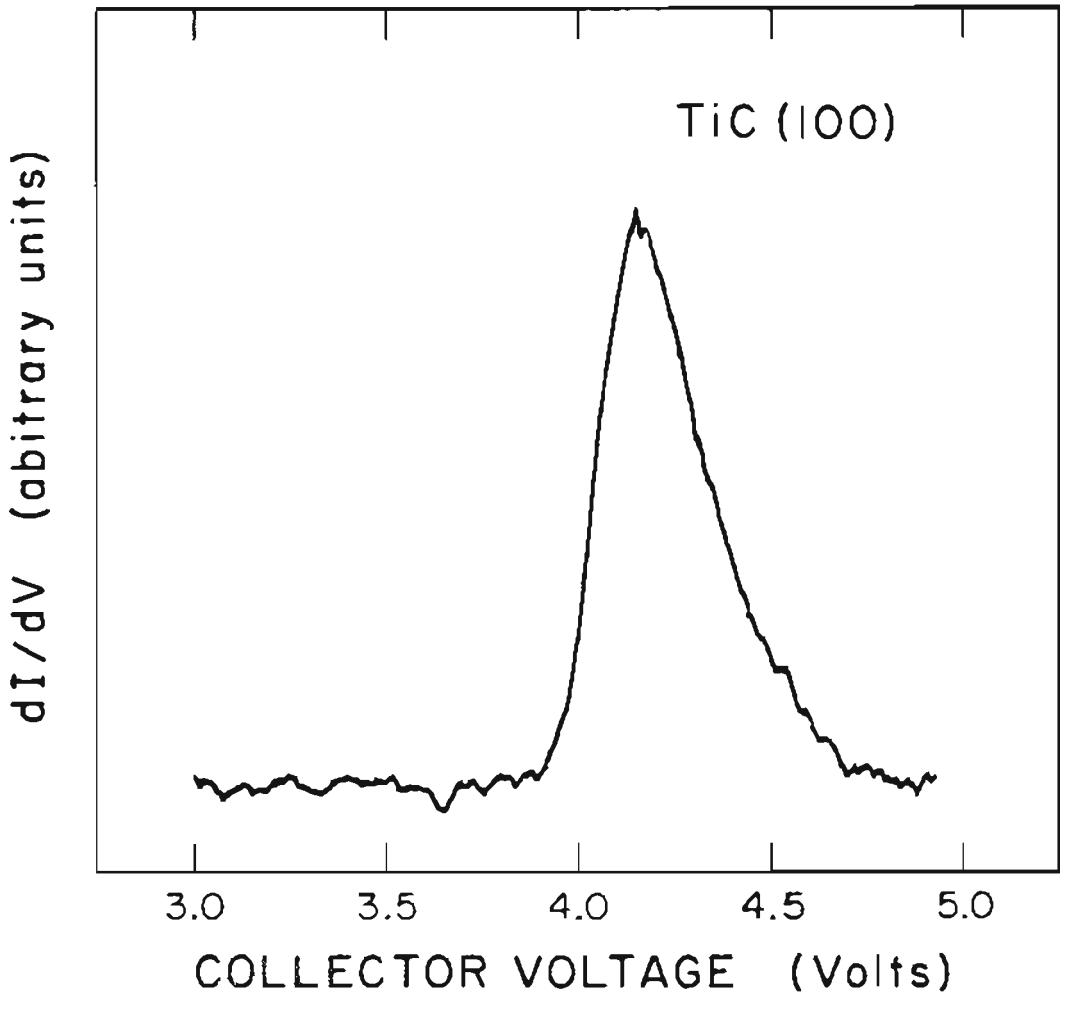

Fig. 24: TED curve for $TiC_{(100)}$ obtained from the FERP apparatus.

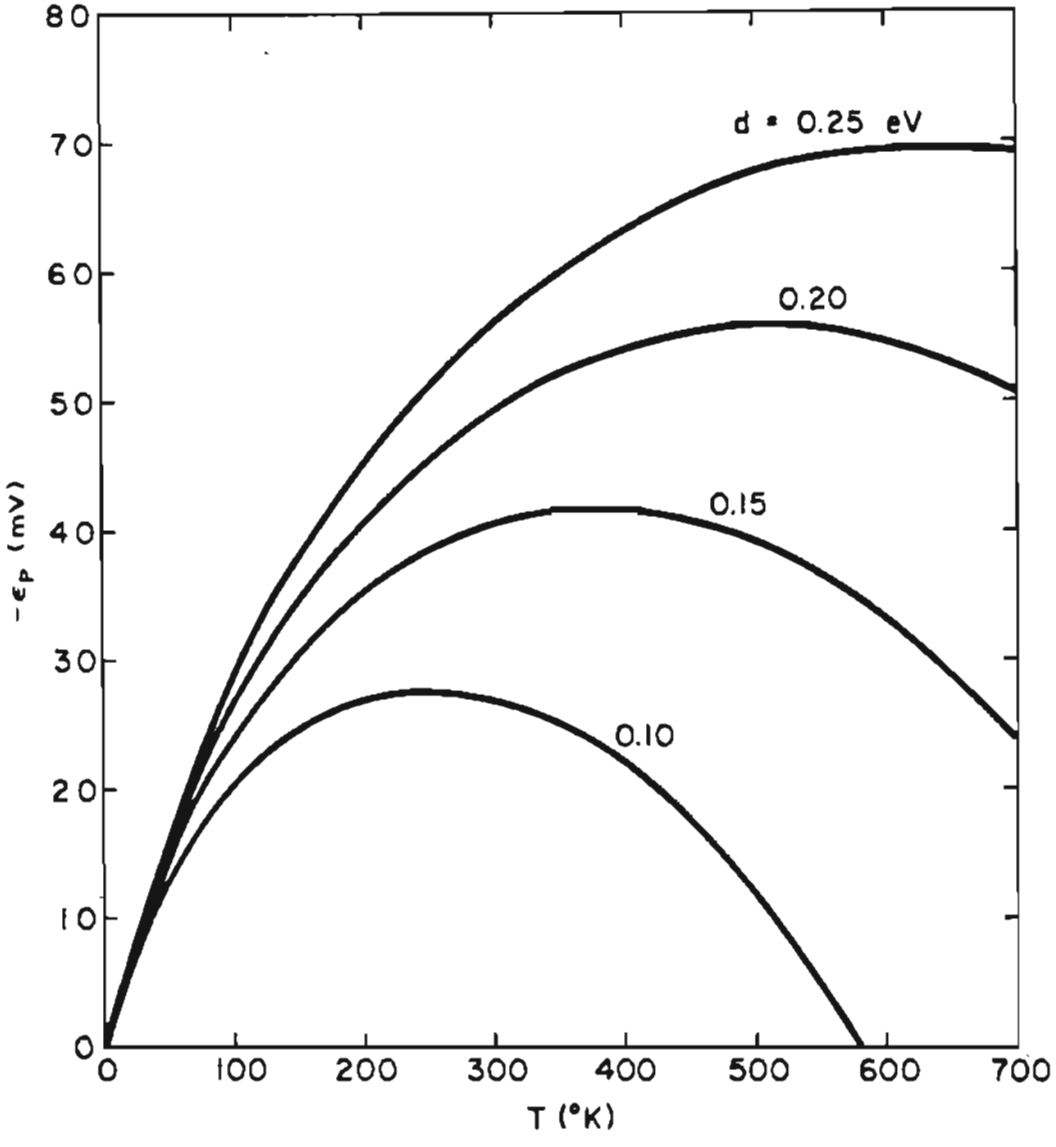

Fig. 25: Energy distribution peak position ε_p as a function of temperature T and distribution parameter d.

i) Experimental setup

The field emission retarding potential (FERP) method of determining absolute single crystal plane work functions is perhaps the most accurate and reliable method available. The procedure is relatively simple and has been described in detail elsewhere.[10]

The vacuum system used for FERP studies also has Auger electron spectrometry (AES) and argon ion sputtering capabilities. With AES, contaminants can be identified and approximate surface stoichiometry revealed. This vacuum system utilizes an ion pump and is capable of attaining pressures in the 10^{-10} torr range with a moderate bakeout. The sample is mounted on a revolving table which can position the crystal for either FERP, AES, or Ar^+ sputtering.

A FERP electron gun similar to that used on this system is shown in Fig. 26. The electronics associated with the FERP gun are diagrammed in Fig. 27. Typical values of lens voltages are given in Table X.

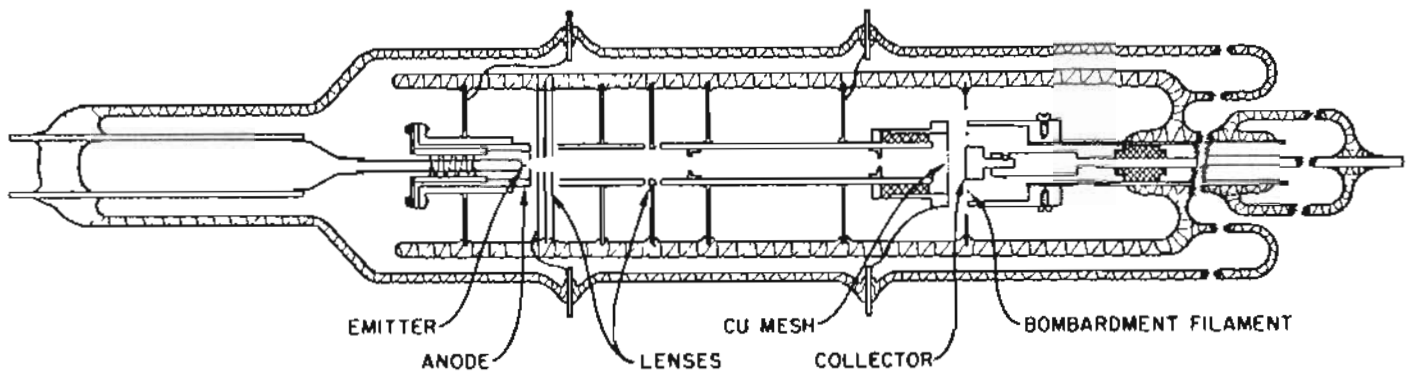

Fig. 26: Diagram of the FERP tube showing the pertinent features of the optical system and collector.

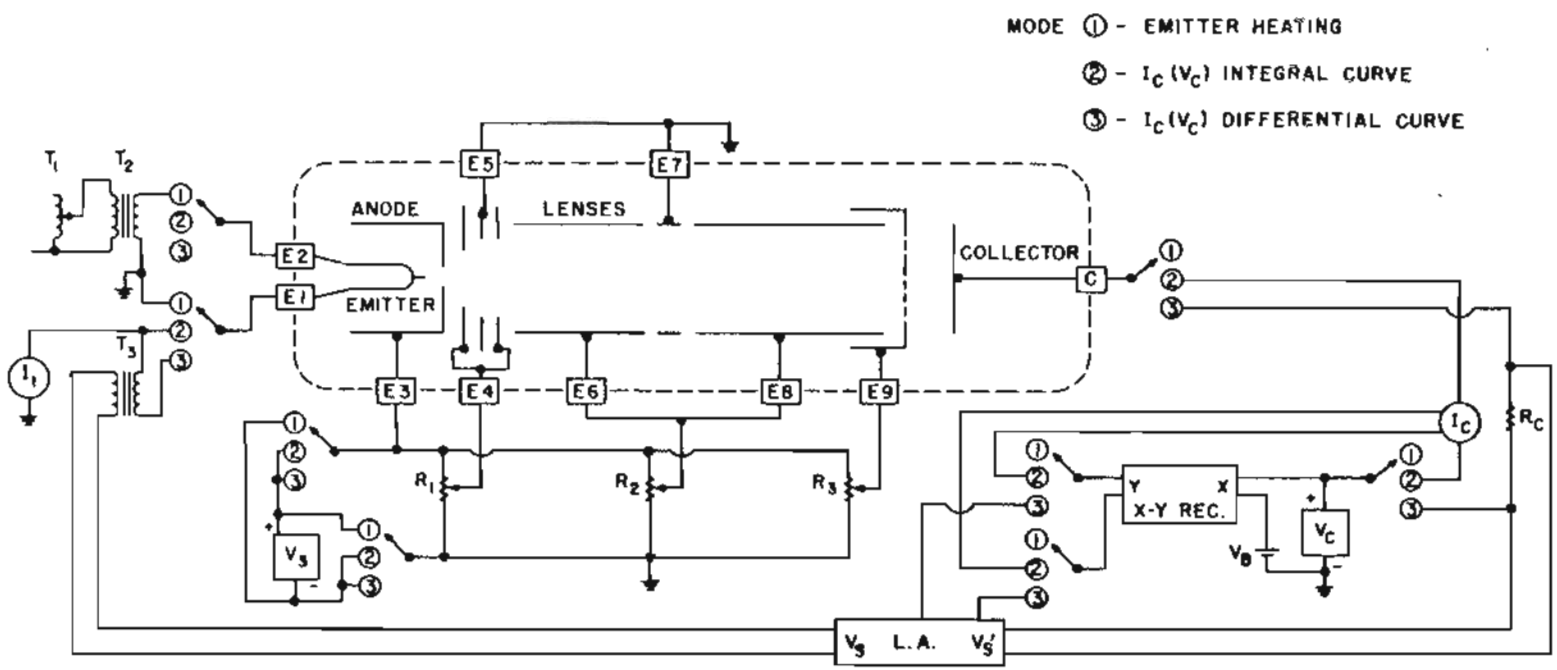

Fig. 27: Diagram of the electrical circuitry associated with the FERP method.

TABLE X: Operating voltages on the extraction and lens elements of the FERP gun. The emitter is at 0.0 V.

Lens elements	Operating voltages
E_4	0.06 E_3
$E_5 = E_7$	0.0 V.
$E_6 = E_8$	0.04 E_3
E_9	5-10 or 130-150 V.

B. AUGER ELECTRON SPECTROSCOPY (AES)

One phase of the research was the manufacture of ZrC emitters for study using the FEM. To make emitters with small enough tip radii for field electron emission, an electrochemical etch was used as previously described. Some emitters so made showed signs of chemical reactants or etchant products on the emitter when viewed under a SEM. This section describes the use of AES to identify the surface contaminants as well as the vacuum and thermal treatment required for their removal. Additionally, AES was used to evaluate surface stoichiometry of the single crystal (100) oriented sample in combination with FERP analysis.

i) Background

The Auger process is a three electron process. An initial core electron is ejected through collisions with a primary bombardment beam of incoming electrons. In a small fraction of cases, a higher level electron drops into this vacant core level. In doing so it yields its excess energy to a neighboring higher level electron thereby ejecting it with energy given by

$$E = E_p - E_k - \phi \qquad (20)$$

where E_p is the primary beam energy, E_k is the energy of the first

ejected electron and ϕ is the surface work function. The higher level ejected electron is called the Auger electron. By analyzing the energy of this electron, it is possible to determine the species of atom from which it came, due to the fact that its energy is determined from the specific, unique energy levels of that atom species.

Auger electrons were first identified in the mass of secondary electrons coming from electron bombarded surfaces by James Lander in 1953.[11] These electron energy peaks are superimposed on the higher intensity spectrum of electron energies which arise from secondary electrons, inelastically scattered electrons, and electrons ejected from the higher or valence electrons in the metal.

In 1968, Lawrence Harris[12] demonstrated that by taking the derivative of the secondary emission distribution, the Auger spectrum could be distinguished in great detail. (see Fig. 28) Auger electron spectroscopy (AES) then became a viable technique for the analysis of compositions of surfaces. Its surface specificity is due to the relatively low energies of the bulk of Auger spectra, up to about 2 keV. These electrons have escape depths of the order of a few atomic layers. The practical detection sensitivity of AES is typically in the range of a few percent of the atoms in this surface region.

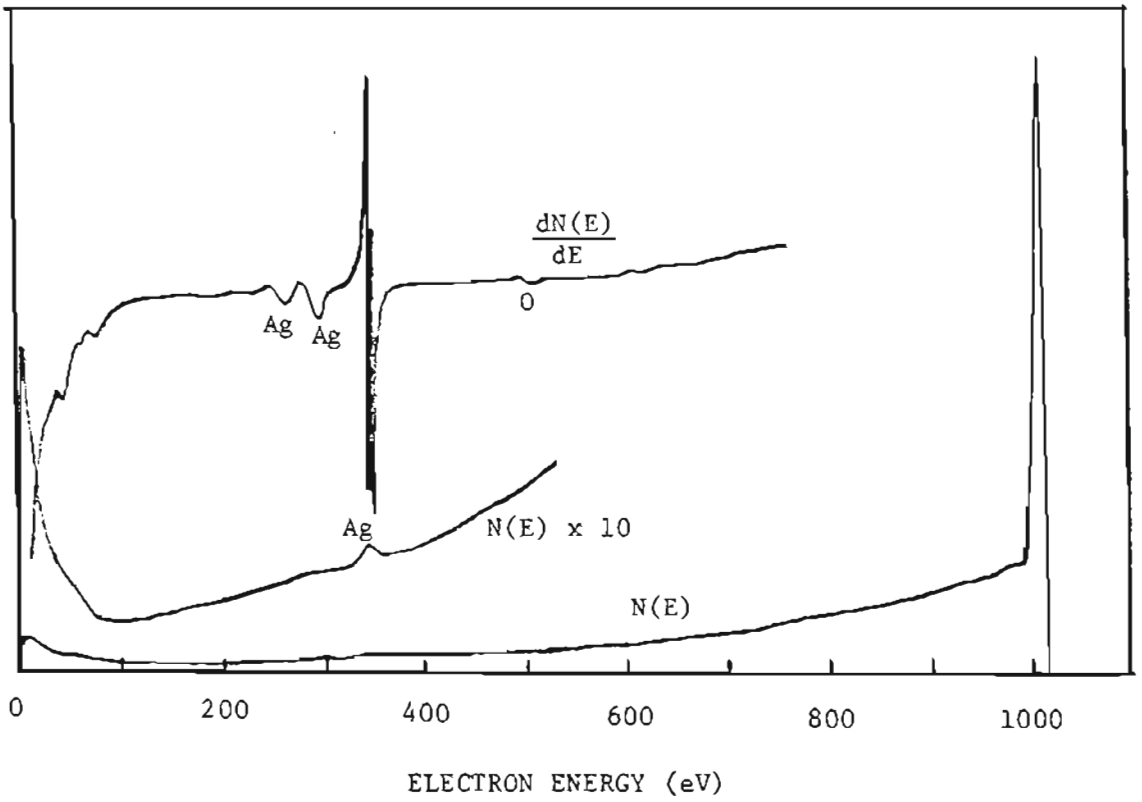

Fig. 28: Energy distribution of secondary electrons:

Target Ag, E_p = 1000 eV.

ii) Experimental Procedure and Results for Etched Sample

The fixed-beam AES analyzer used in this study had a minimum beam spot size of ~100 μm. It was therefore impractical to focus the electron beam onto the shank of an actual field emitter. Instead, a 0.300 inch length of roughly 0.055 inch diameter zone melted ZrC was used as a sample. This piece was mechanically mounted on a standard emitter holder with two wraps of 0.010 inch Ta wire brazed in place with Ta-Co alloy as discussed earlier. (see Fig. 10)

Prior to heating the sample, an AES scan was taken and the adsorbates identified, Fig. 29. Note in particular the presence of Cl from the HCl in the etchant solution, N from the HNO_3 in the etchant solution and/or atmosphere, Zr and a large amount of O, and the absence of peaks indicating carbides.

The ZrC sample was heated to 866 C and, while hot, the next AES scan was taken, Fig. 30. Note in this case the absence of the previously noted Cl peak. Further heating was done in steps with an AES scan being taken soon after the heating current was turned off. A complete summary of the heating sequence is listed below. (Table XI)

TABLE XI: Desorption Temperatures

RUN #	Brightness	Temperature (C)	Filament Current	Figure # for Auger plot
1	no heating	room temp.	---	----
2	no heating	room temp.	---	29
3	835	866	9 A.	30(hot)
4	980	1022	10 A.	---(hot)
5	1050	1098	11.5 A.	31
6	1150	1209	12.5 A.	---
7	1250	1320	13.5 A.	32
8	1350	1433	~ 15 A.	33
9	1410	1502	> 15 A.	34
10	1500	1606	18 A.	---
11	1600	1724	21.5 A.	35

No AES plots are included for those temperature steps where no appreciable changes occurred. The only change noted during the intermediate temperatures was that the peak height of C increased somewhat while that of O decreased slightly, Figs. 31 and 32. The pressure during this time was $< 2 \times 10^{-9}$ Torr.

After heating to 1433 C, dramatic changes were noted, Fig. 33. Specifically, the Zr and C peak heights increased and the development of carbide peaks was first observed, while the O peak height continued to decrease and the small peak of N remained present. This temperature seems to be the desorption temperature for the surface adsorbates.

Following the 1502 C heating, more dramatic changes were noted, Fig. 34, including continued development of the carbide peaks and a marked reduction in the O peak.

Heating to 1724 C resulted in almost complete desorption of N and O, Fig. 35.

In order to view the data in total, the relative percentages of the various components were first estimated. These were calculated using peak to peak heights corresponding to peaks with sensitivities tabulated in the literature[13] and listed in Table XII. Since 4 keV primary electrons were used in this study, a linear interpolation was made based on 3 keV and 5 keV electrons whose elemental sensitivities are given.

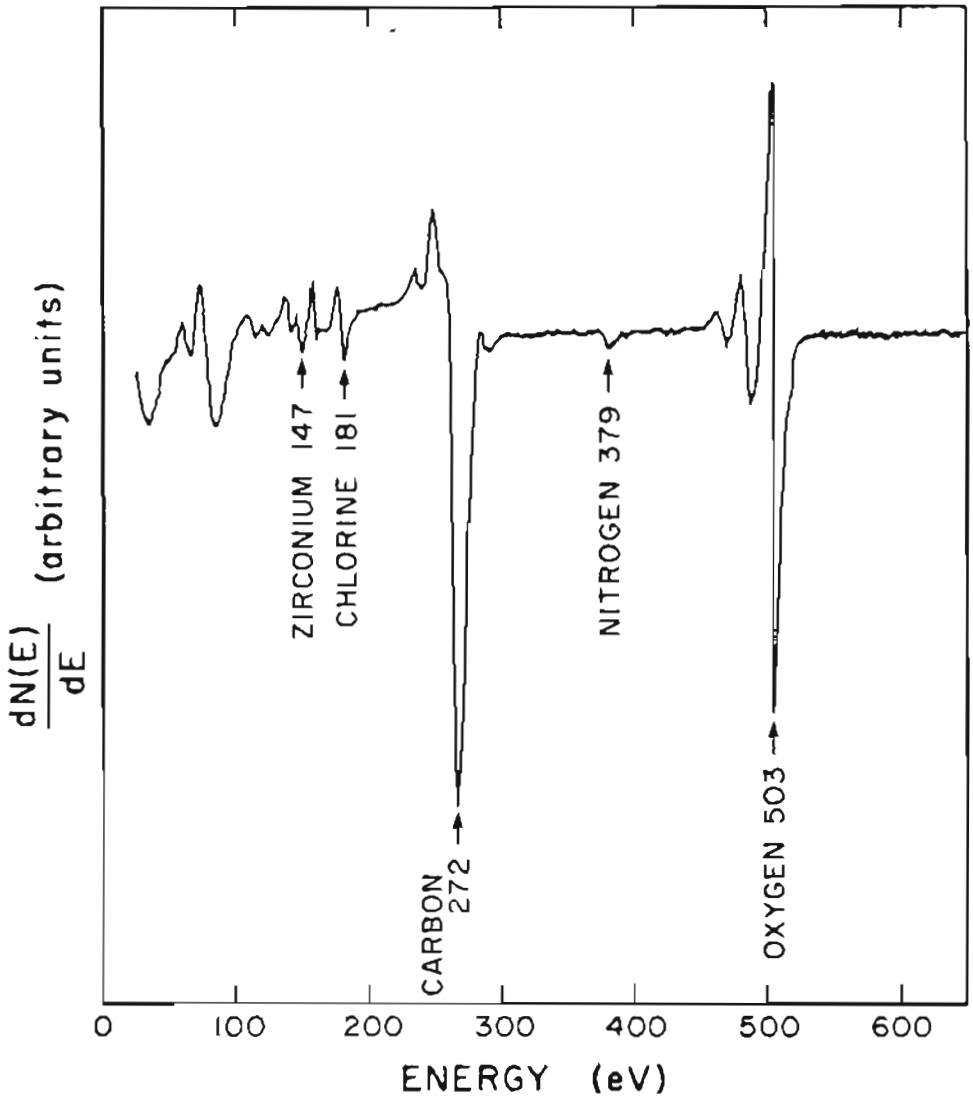

Fig. 29: Auger plot taken before heating on ZrC target.

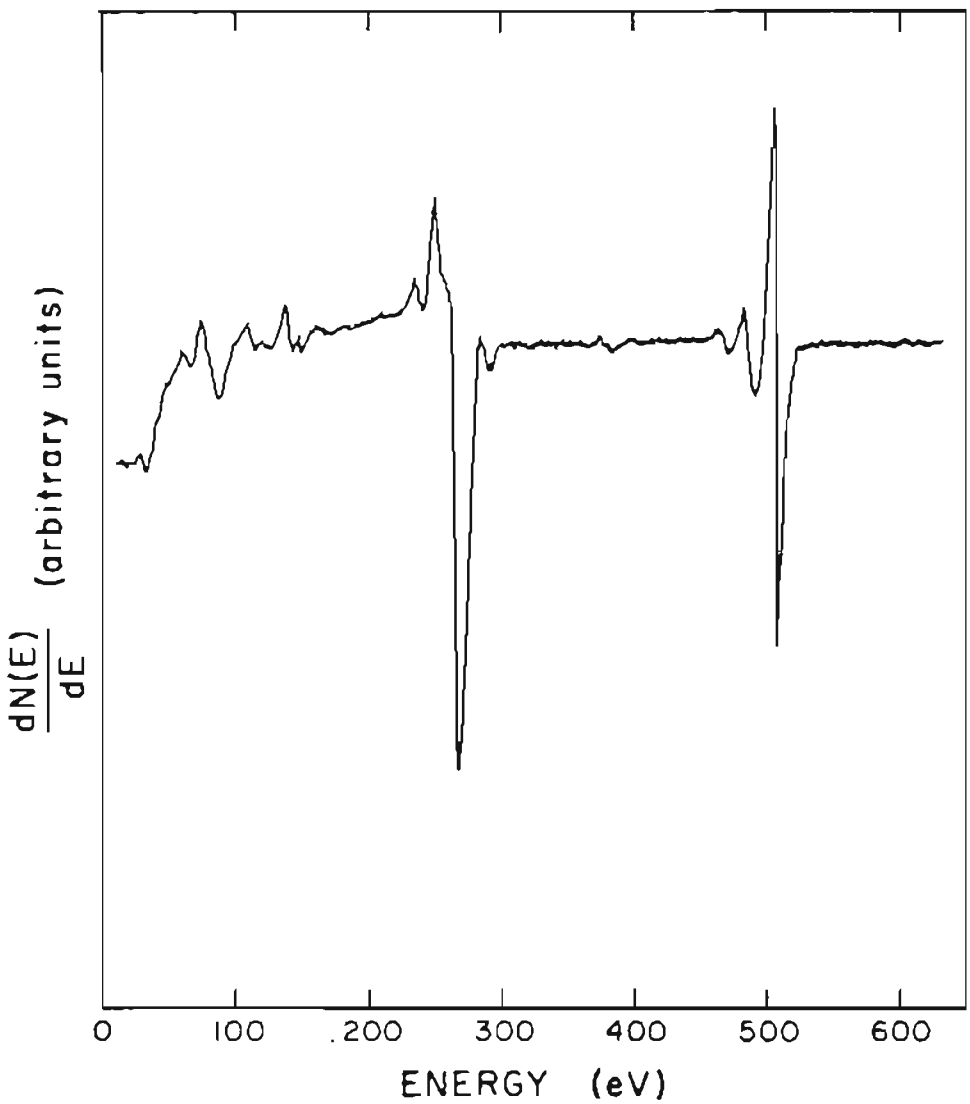

Fig. 30: Auger plot of ZrC target taken while at 866 C.

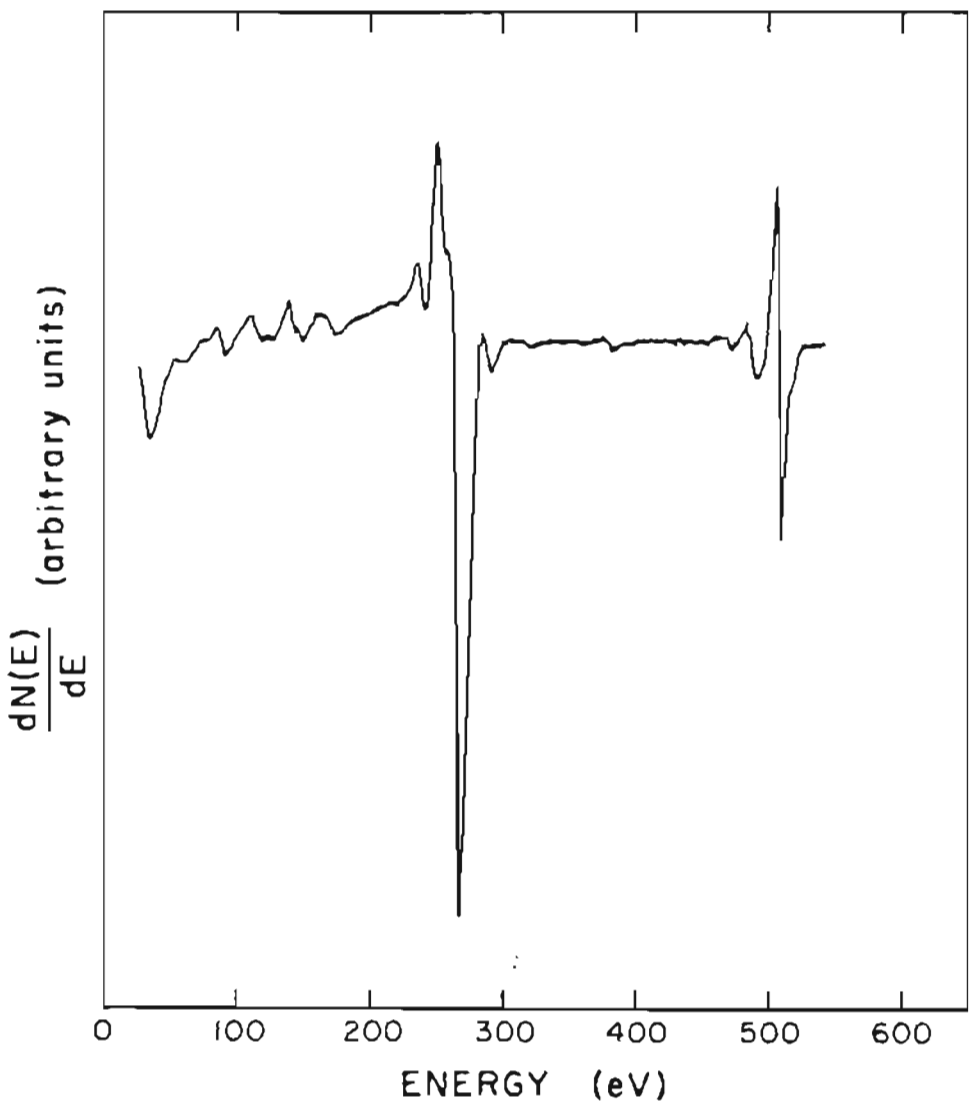

Fig. 31: Auger plot of ZrC target taken after heating to 1098 C.

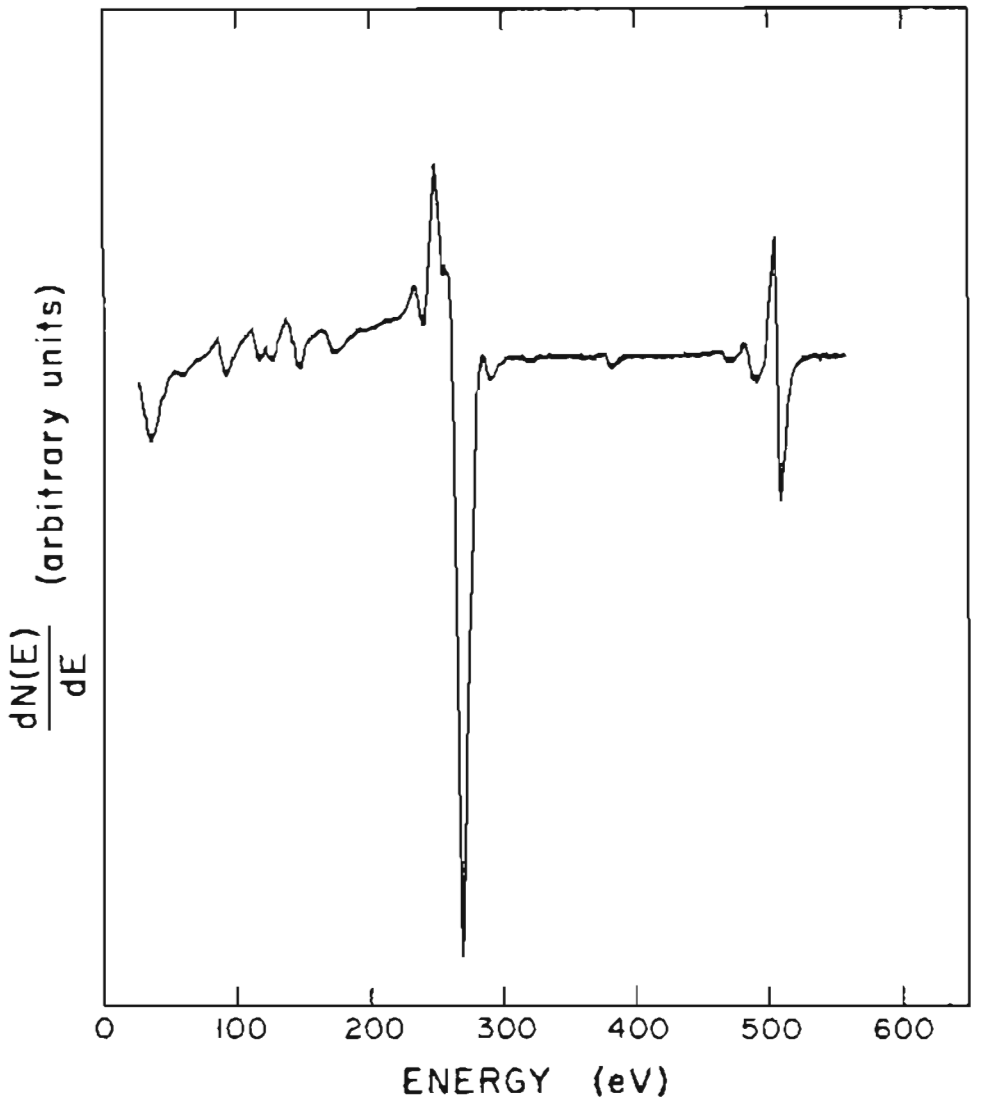

Fig. 32: Auger plot of ZrC target taken after heating to 1320 C.

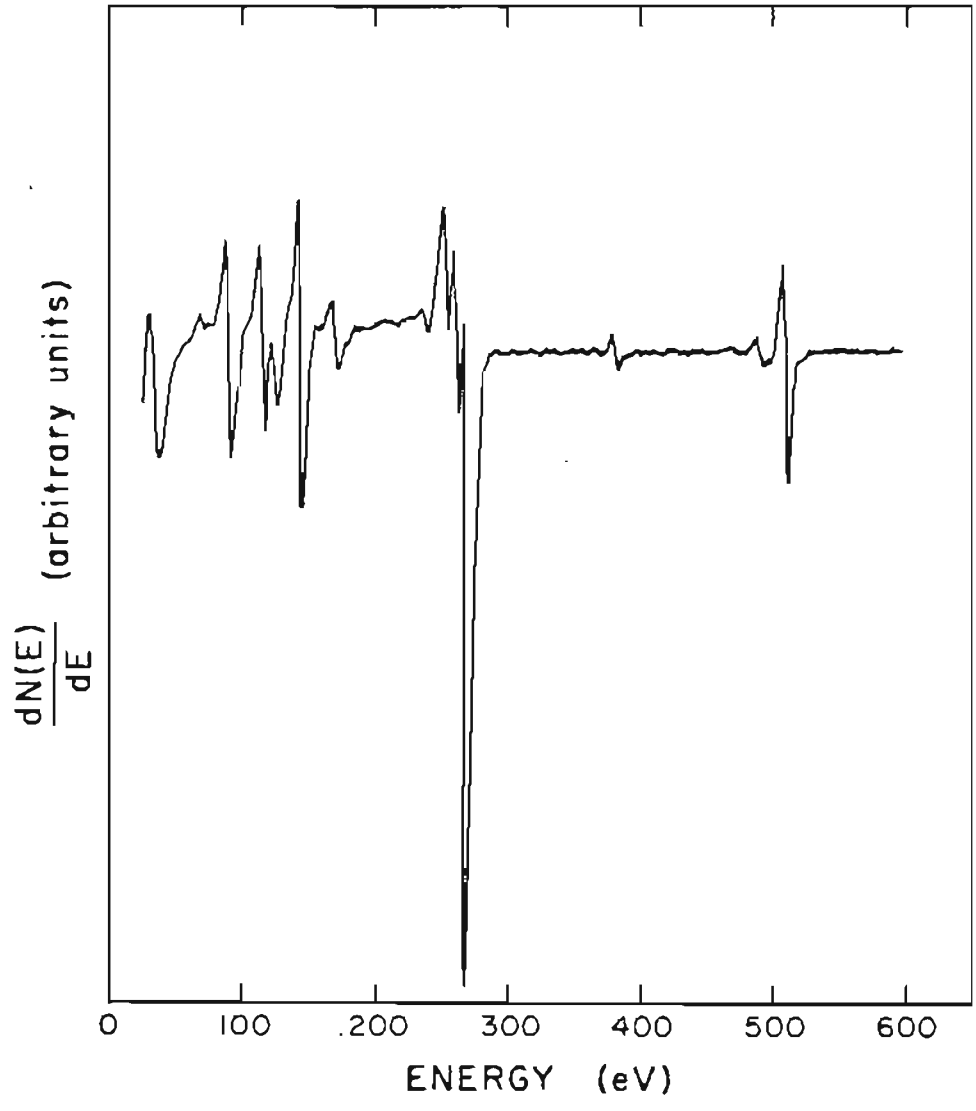

Fig. 33: Auger plot of ZrC target taken after heating fo 1433 C.

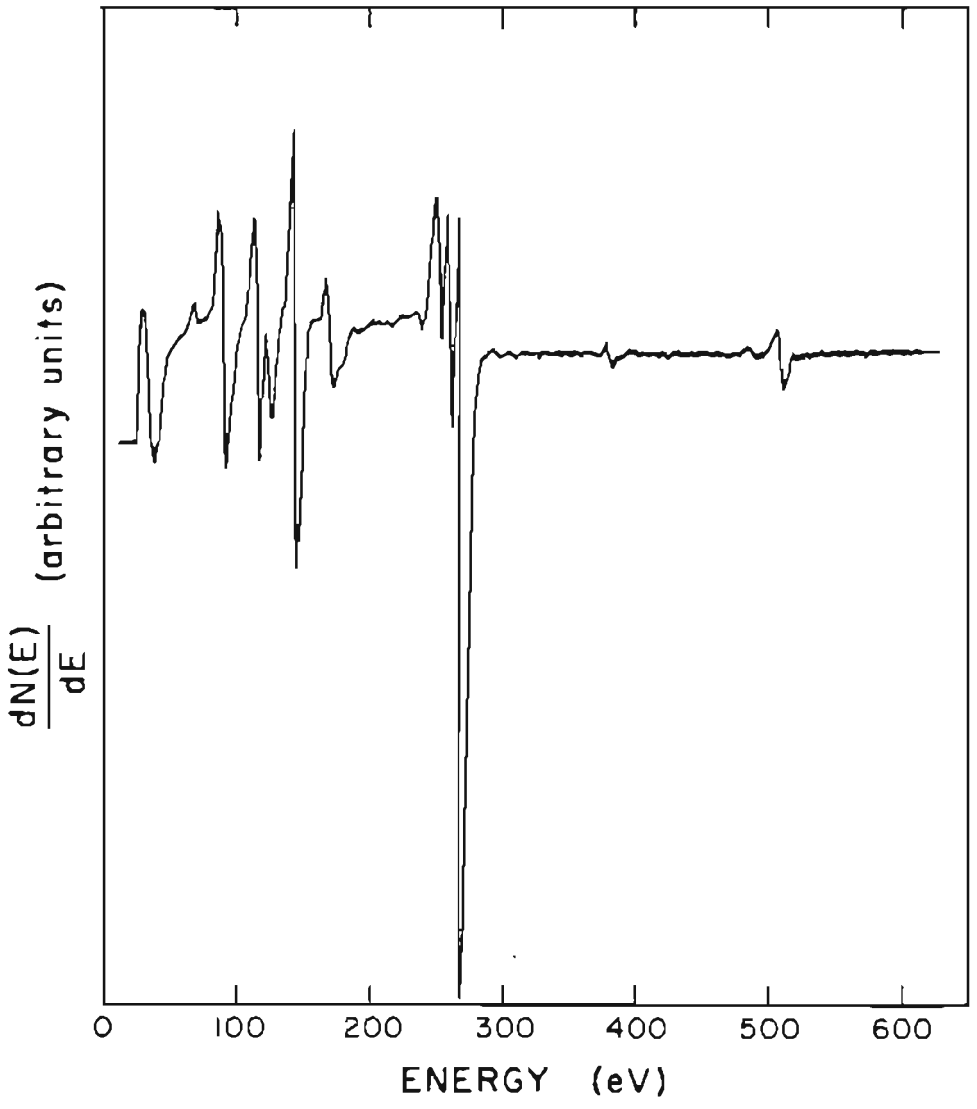

Fig. 34: Auger plot of ZrC target taken after heating to 1502 C.

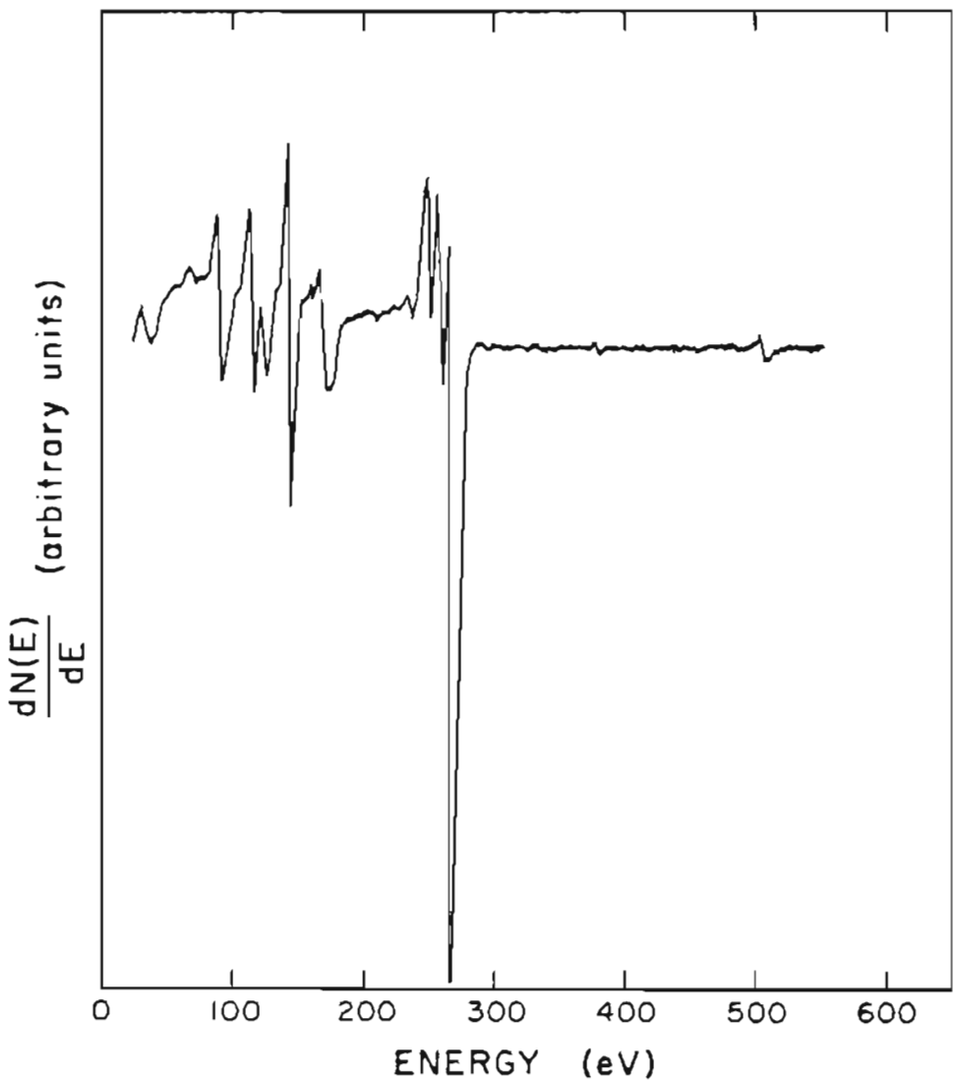

Fig. 35: Auger plot of ZrC target taken after heating to 1724 C.

TABLE XII: Auger Sensitivities[13]

Element	Transition (peak eV)	Sensitivities at: 3 keV	4 keV	5 keV
Zr	MNN (147)	0.22	0.19	0.16
Zr	LMM (1845)	0.015	0.0225	0.03
Cl	LMM (181)	1.0	1.0	1.0
C	KLL (272)	0.18	0.16	0.14
N	KLL (379)	0.32	0.27	0.22
O	KLL (503)	0.5	0.46	0.42
Ar	LMM (215)	1.0	1.0	1.0
Ti	LMM (418)	0.45	0.40	0.35

The surface atomic concentrations were calculated using the formula[13]

$$C_x = \frac{I_x/S_x d_x}{\Sigma_\alpha \, I_\alpha/S_\alpha d_\alpha} \, . \qquad (21)$$

Since

$$d_x = L_x E_{m,x} I_{p,x} \qquad (22)$$

where the lock-in amplifier sensitivity, L_x, modulation energy, $E_{m,x}$, and primary beam current, $I_{p,x}$ used to obtain the spectra were constants, we can cancel these factors because $d_x = d_\alpha$.

The calculated concentrations of the various elemental components are plotted simultaneously versus temperature in Fig. 36. As a further,

and possibly better, means of displaying the data, sensitivity corrected peak to peak heights are plotted versus temperatures for C, Zr, and O in Fig. 37.

These data imply a C/Zr ratio on a thermally cleaned surface of 2.1 to 2.8 (1502 C and 1724 C respectively). While this seems very high the zone melted crystalline material, on the average, had a C/Zr ratio of 1.2, additionally the C/Zr ratio of the sintered stock was 1.5. These analysis were done by the U.S. Bureau of Mines Laboratory in Albany, OR.

While there are uncertainties as to the surface stoichiometry of the ZrC sample both before and after heating, it is clear that flashing to 1700 C is sufficient to remove surface adsorbates. The mechanism of adsorption/desorption is still uncertain, however it seems that the oxygen is desorbing as CO. A means for further analysis might be to use X-ray photoelectron spectroscopy (XPS) to investigate the nature of chemical bonding on the surface. Finally it would be interesting to duplicate this experiment and study the parameters involved with adsorption of oxygen onto a clean ZrC crystal sample.

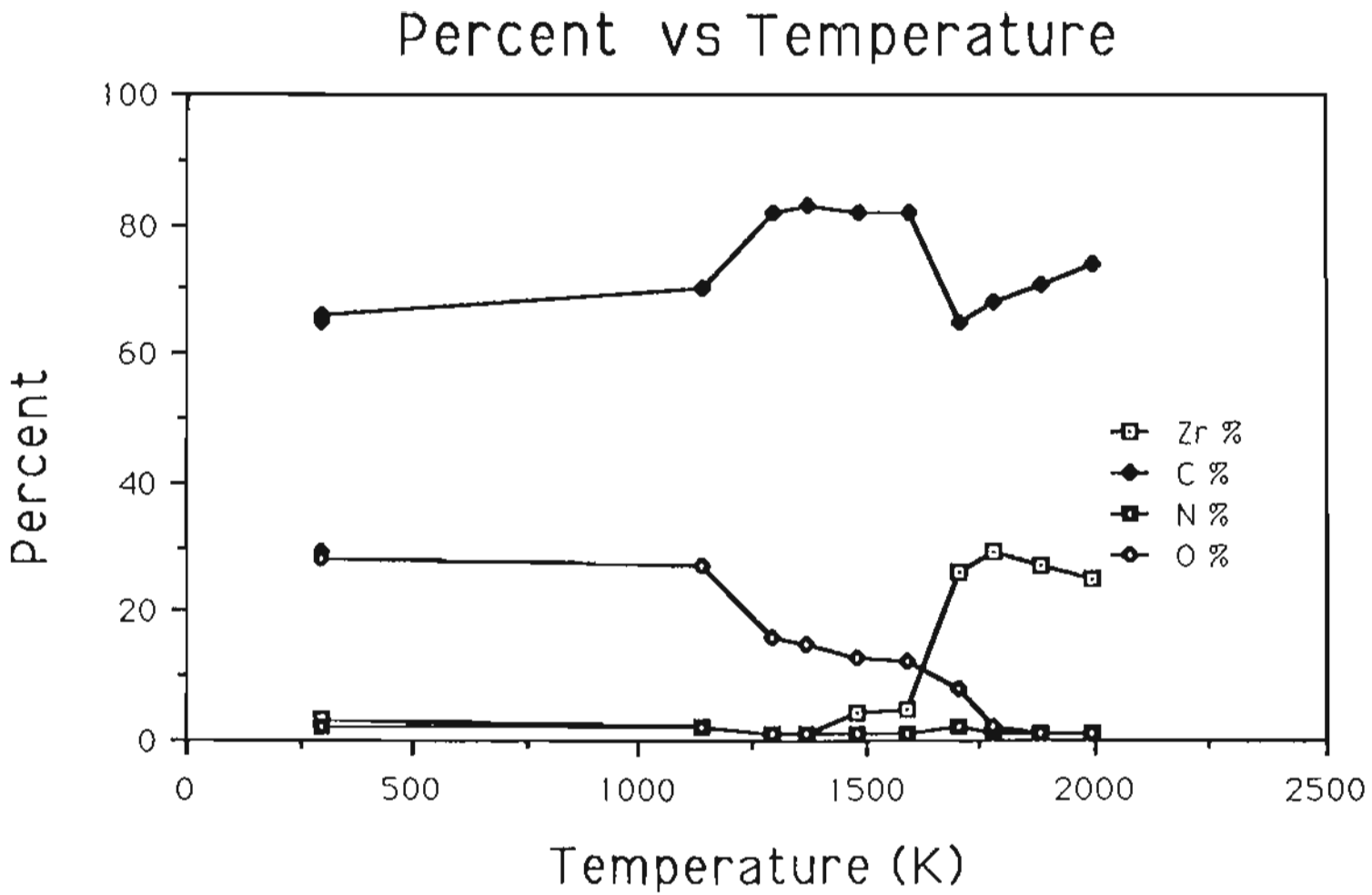

Fig. 36: Thermal desorption from ZrC.

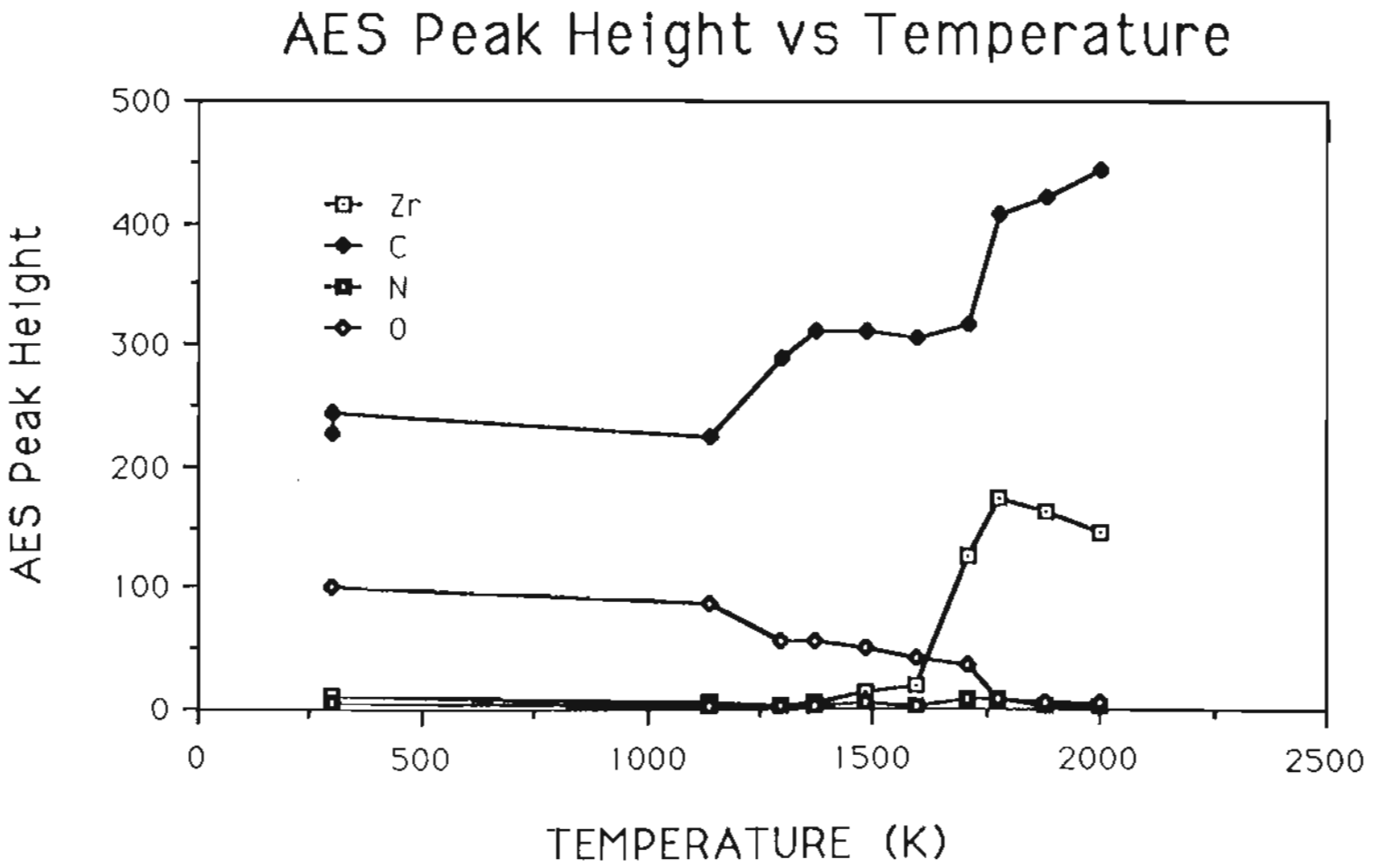

Fig. 37: AES peak height of Zr, C and O as a function of temperature.

iii) Single Crystal FERP/AES Studies

1) Zirconium Carbide

After obtaining pressures of $<2 \times 10^{-10}$ torr and adjustment of equipment, we were able to obtain interesting AES and FERP data. A table of the most informative data can be seen in Table XIII. The chronology of typical events is that immediately after heating an Auger plot was taken. This was quickly followed by FERP work function determination. Occasionally, another AES was scanned to check for contamination during the preceding process. The elapsed time from initial heating until the second AES was checked usually was less than five minutes. Table XII gives the Auger sensitivities used in evaluating these data.

Table XIII: Table of AES and FERP data after each heating/sputtering step. The two C/Zr ratios are explained in the text.

	% Oxygen	% Nitrogen	C(KLL) Zr (MNN)	C(KLL) Zr (LMM)	FERP Peak Position (eV)
Before Heating:	25.0	1.9	8.6	----	----
After Ar ion sputtering & 1376 C heat:	33.7	3.9	1.99	0.85	----
After Heating 1665 C:	2.6	1.7	2.46	1.50	4.50
After 48 hrs at 2×10^{-9} torr:	4.1	3.7	2.47	1.35	4.85
After Heating 1844 C:	2.2	1.3	2.51	1.98	4.08
After 1.25 hrs at 1×10^{-9} torr:	3.2	3.0	2.52	----	4.48
After Heating 2029 C:	0.6	2.1	2.50	----	3.80
After Heating 1998 C:	0.6	0.5	2.77	----	4.03
After Ar ion sputtering:	6.0	3.6	2.1	1.20	5.05
After Heating 1376 C:	1.4	2.2	2.3	1.70	3.53

	% Oxygen	% Nitrogen	C(KLL) Zr (MNN)	C(KLL) Zr (LMM)	FERP Peak Position (eV)
After Heating					
1530 C:	0.8	1.3	2.4	1.60	3.83
After Heating					
1577 C:	2.3	1.6	2.33	1.85	3.62
Exposed to atmospheric pressure of air at room temperature:					
w/o Heating:	31.7	<1.0	4.46	1.62	ZrO present
After Heating					
1044 C:	12.7	<1.0	5.27	1.74	----
After Heating					
1264 C:	5.2	<1.0	2.48	1.37	----
After Heating					
1548 C:	5.7	<1.0	1.82	1.77	----
After Heating					
1724 C:	5.3	<1.0	1.85	1.88	----
After Ar ion					
sputtering	40.0	<1.0	1.67	----	----
After Heating					
1044 C:	2.0	<1.0	2.13	----	----
After Heating					
1320 C:	3.6	<1.0	2.12	----	3.95
After Heating					
1724 C:	3.7	<1.0	1.52	----	5.05

2) Titanium carbide

A very cursory examination of TiC was done. The results are summarized in Table XIV. The percents of the various constituents were calculated using the extrapolated 4 keV auger sensitivities listed in Table XII.

Table XIV: Table of preliminary AES and FERP data after each sputtering and heating step.

	% Titanium	% Carbon	% Oxygen	C(KLL) / Ti (LMM)	FERP Peak Position (eV)
Before Heating:	8.2	66.4	25.4	8.10	----
After Ar ion sputtering:	26.6	70.8	2.6	2.66	----
After Ar ion sputtering:	26.6	69.6	3.8	2.62	4.30
After Heating ~1050 C:	23.1	71.4	5.5	3.09	4.65
After Heating ~1400 C:	18.5	79.3	2.2	4.29	4.15

It should be noted that only one transition peak is available for titanium, unlike the two for zirconium as explained in the Discussion, Part Two, Section IIIA. That is the Ti (LMM) transition yields a 418 eV auger electron.

These data are preliminary and further results are needed before any conclusions can be made.

C. FIELD EMISSION MICROSCOPY

i) Theoretical Background

Determination of the electronic work function through the evaluation of field emitted electrons is more uncertain a task than is measurement via the FERP method, or even through thermionic means.

The equation defining the current density of electrons emitted because of a high field is similar in form to Richardson's equation. It was derived in 1928 by R.H. Fowler and L.W. Nordheim[14] and is given by

$$j = 6.2 \times 10^{6}[(\mu/\phi)^{1/2}/(\mu + \phi)]F^{2} \exp[-6.8 \times 10^{7}\phi^{3/2}/F] \quad (23)$$

(in A/cm^2) for all energies in electron volts and F in volts per centimeter. This equation shows that current densities of 10^2 - 10^3 A/cm^2 can be expected for typical fields of 3 - 6 x 10^7 V/cm.

It should be noted that a first-order image correction factor is usually included in the Fowler-Nordheim equation. Instead of including that factor, Eq. (23) can be simplified as,

$$i/V^{2} = a \exp(-b\phi^{3/2}/\beta V) \quad (24)$$

where a and b are constants, and

$$F = \beta V, \tag{25}$$

β being a geometrical factor for the emitter tip.

A Fowler-Nordheim[15] curve, generated by plotting $\ln(i/V^2)$ versus $1/V$ for measured current/voltage data, yields a slope proportional to $\phi^{3/2}/\beta$. An example of such a plot is shown in Fig. 38.

The uncertainty in accurately obtaining a value for the work function arises because of the β factor in the equation for the field, Eq. (25). At the surface of a free sphere of radius r and potential V, the field F is given by

$$F = V/r. \tag{26}$$

In dealing with an actual field emitter, the presence of the conical shank reduces the field value. The field then can be approximated as,

$$F = V/kr \tag{27}$$

where $k \simeq 5$ near the apex and increases with polar angle.

Charbonnier[16] found an empirical relation for k through an electron-microscopic examination of a large number of emitters. This relation

$$k = 0.59\varepsilon^{1/3}(x/r)^{0.13}, \tag{28}$$

where r (cm) is the tip radius, x (cm) is the tip-to-screen distance and ε (deg) is the emitter cone angle, leads to the value of approximately 5 for the most commonly encountered geometries. (see Fig. 39)

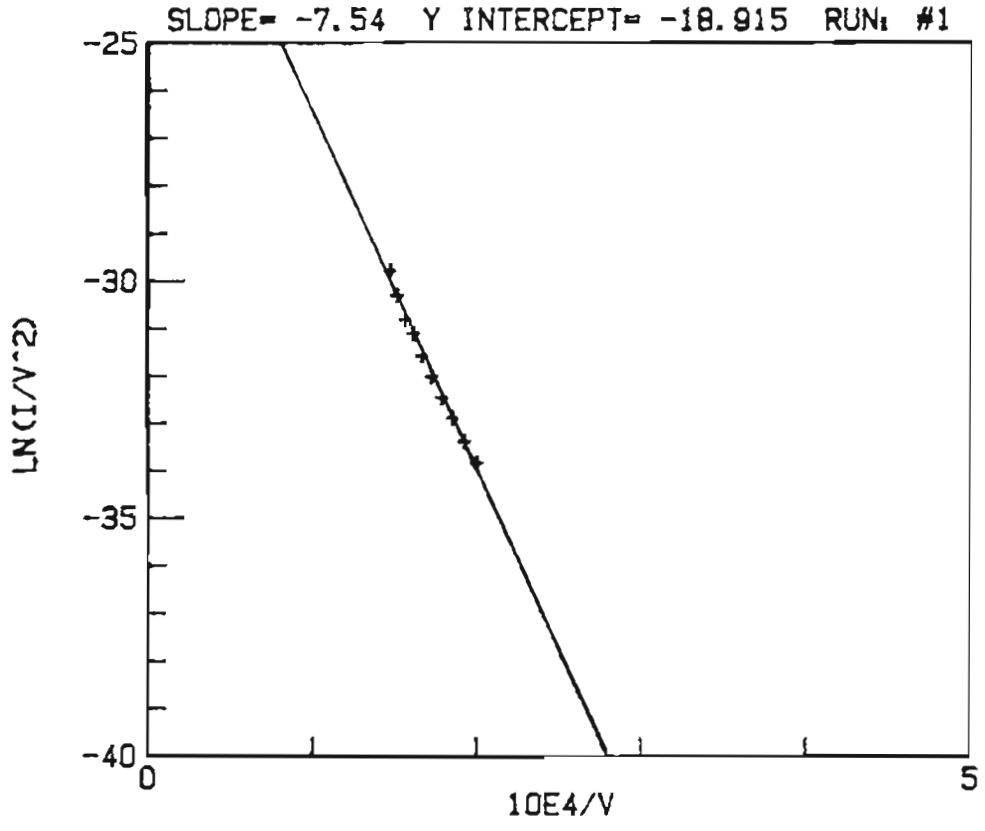

Fig. 38: Fowler-Nordheim curve for a ZrC field emitter.

These approximations lead to uncertainties in the values of the work function. The etched geometries for the carbides are rarely ideal and do not readily conform to any prescribed pattern. Additionally, the end of a field emitter made of transition metal carbides can facet drastically, changing the geometry and the emission pattern. Even so, without a probe type field emission microscope tube, the values obtained tend toward the lowest work functions of the surface. This is because an emitter contains many different crystal planes and field emission is exponentially weighted toward low work function values.

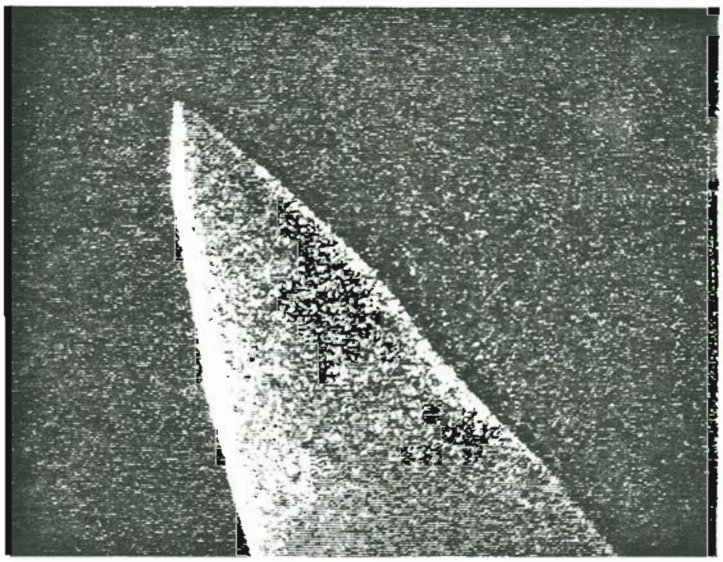

Fig. 39: Scanning Electron Micrograph (SEM) of a typical ZrC field emitter.

ii) FEM Tube Design and Vacuum System

After mounting, etching and micrographing the emitters, they were ready for mounting in the field emission microscope (FEM) vacuum tubes. The mounting was done using Mo connectors with stainless steel 2-56 x 0.125" machine screws. Due to electrical and vacuum leakage problems previously encountered with commercial 7-pin 2.75" flanged feed throughs, we converted all the FEM tubes to glass insulated W feed throughs made in house. (see Fig. 40)

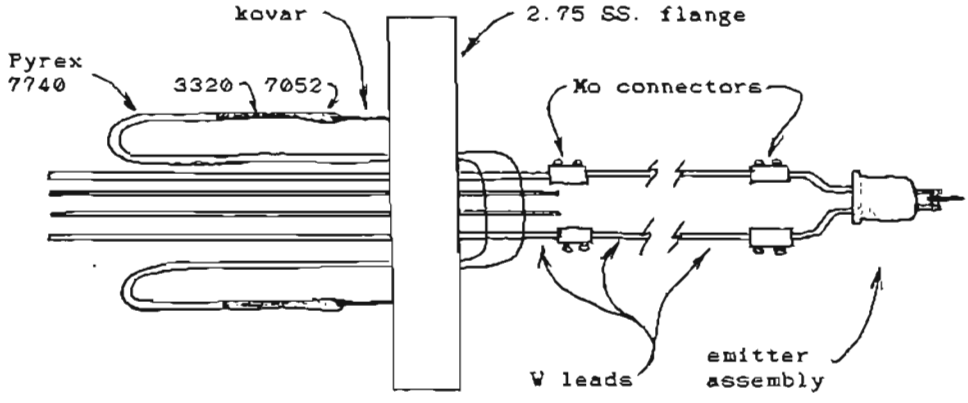

Fig. 40: Design of 4-pin feedthroughs and emitter mount.

The 0.060" or 0.080" W feedthrough leads easily handled the currents, sometimes >20 amps needed to heat the emitters via the double

0.010" Ta filaments.

The FEM tube itself consisted of a pyrex bulb with a Corning 3320 glassed W pin feed through for the screen connection. Inside the tube the W lead was attached to the pyrex envelope via a Pt strip. The screen was composed of two layers. The first layer was a conductive coating deposited at 500 C by puffing vaporized stannous chloride into the hot tube. The second layer was a phosphor type coating, puffed onto the glass at room temperature and then baked at 450 C.

The tube envelope was left attached to the Hg diffusion pumped vacuum system and only the emitter flange was removed to change emitters. Just prior to bolting the flange back onto the system, the Co-Ta alloy braze was applied to the Ta filaments using a slurry of the powdered braze in methanol. Heating of this braze was carried out after a suitable vacuum has been achieved.

Two dozen etched emitters and one ground emitter have been examined in FEM tubes. In some cases no data was obtained due to filament failure while heating the sample for thermal desorption or due to the high voltage needed because of relatively dull emitters, spurious emission from other sources have inhibited the collection of useful information for these emitters. Other emitters have been examined as typically described below.

After mounting emitter assembly on flanged feed throughs, the flange assembly was inserted in tubes previously connected to the Hg diffusion pumped vacuum system. After establishing a preliminary vacuum, the

system was baked at 250 C for the main oven and 200 C for the trap oven. LN_2 is kept on the trap at all other times. Pressures of 1×10^{-9} Torr were easily achieved after bake and outgassing of emitter filaments and getter filament which was also attached to the systems manifold.

The data shown is from a configuration that uses a double 0.010 Ta filament on the crystal shank. In addition to examining the double filament, extreme care was taken to ensure no other sharp protrusions exist which would give rise to the spurious emission.

The above procedures were carried out on the tip ZrC-E6, whose micrographs are shown. (see Fig. 41)

140 X 1400 X 14000 X (r = .9 μm)

Fig. 41: SEM pictures of ZrC-E6 emitter.

This emitter gave an emission current of 0.2×10^{-6} A at a applied voltage of 3500 V. I(V) data were taken, and plotted with the aid of a HP 86B computer.

The Fowler-Nordheim plots (see Figs. 42 and 43), show that temperatures of approximately 1500 C are only needed to obtain reproducible slopes, which could indicate a "clean" emitting surface. This agrees with the AES data.

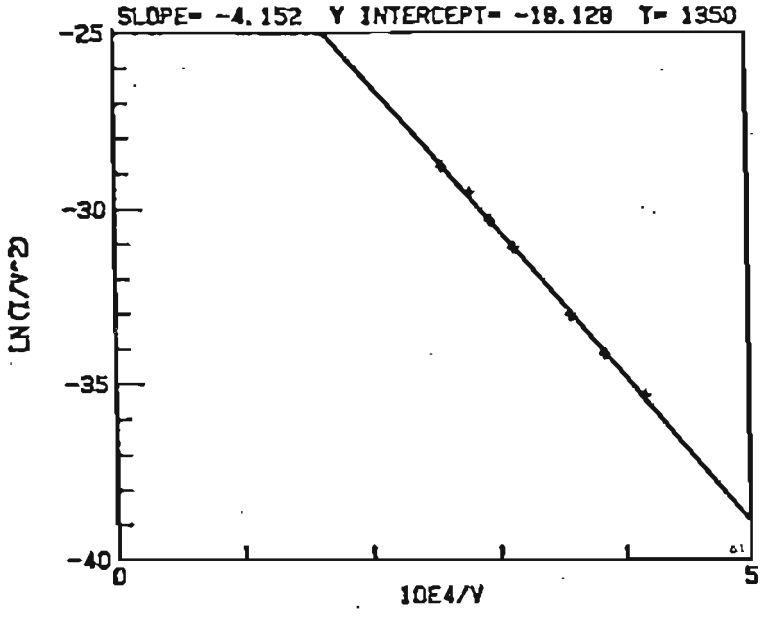

Fig. 42: F-N plot of emitter E6 after 1350 C flash.

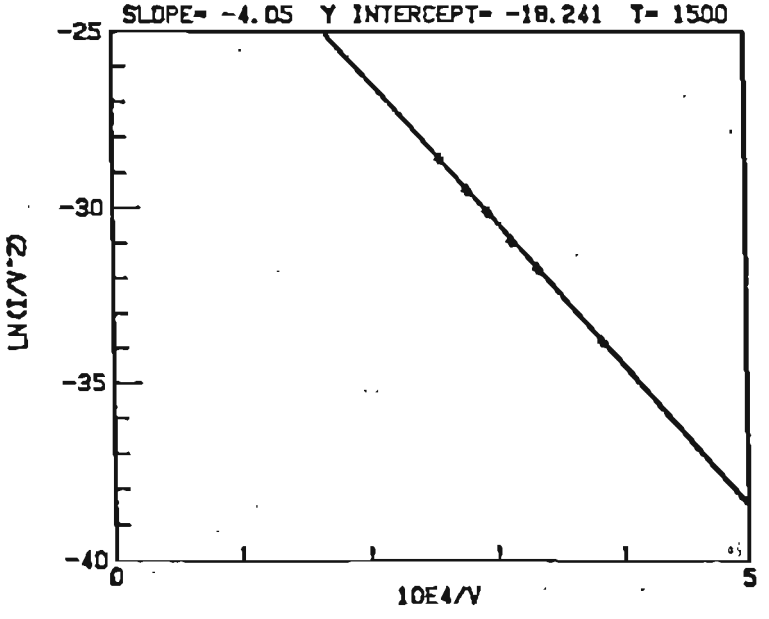

Fig. 43: F-N plot of emitter E6 after 1500 C flash.

Through the use of the double filament configuration, heating the emitter to >2000 C was achieved. Temperature measurements were obtained by use of an optical pyrometer.

The ability to obtain a clean surface is reduced due to the pressure rise while flashing the emitter. Typically P = 8-9 x 10^{-9} torr during a flash to around 1700 C. The emitting patterns obtained were not symmetrical. This could be due to the low self diffusion of ZrC even at elevated temperatures. This notion is further verified by the fact that even after heating to >2000 C the I(V) data were essentially unchanged. (Again high 10^{-9} torr pressures may complicate exact determinations.)

In an attempt to obtain a symmetrical emission pattern, and to evaluate its utility, field desorption was tried. After field desorbing at +30,000 volts (relative to the tip) the patterns were markedly changed and a centered pattern was obtained. While not completely symmetrical, patterns were obtained which "filled" the screen with an emission pattern centered about high current density spots at the screens center. Again F-N plots were taken (see Figs. 44 and 45).

A micrograph of the tip was taken, to note any geometrical changes associated with the field desorption. The tip had obviously dulled since 6800 V. was needed to yield an emission current of 0.54 microamps. The observation was that the uncentered protrusion which yielded the uncentered emission pattern was field desorbed, thereby changing the tip to one with a larger tip radius. While symmetrical patterns were not obtained with these methods, the cathodes examined have exhibited good

temporal stability, compared with W cathodes, at pressures even as high as 8×10^{-8} torr.

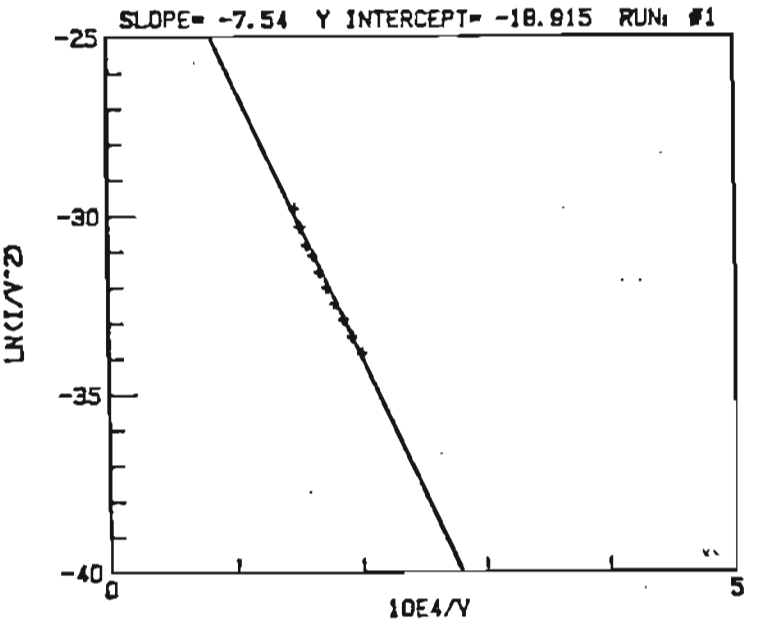

Fig. 44: F-N plot of emitter E6 after field desorption.

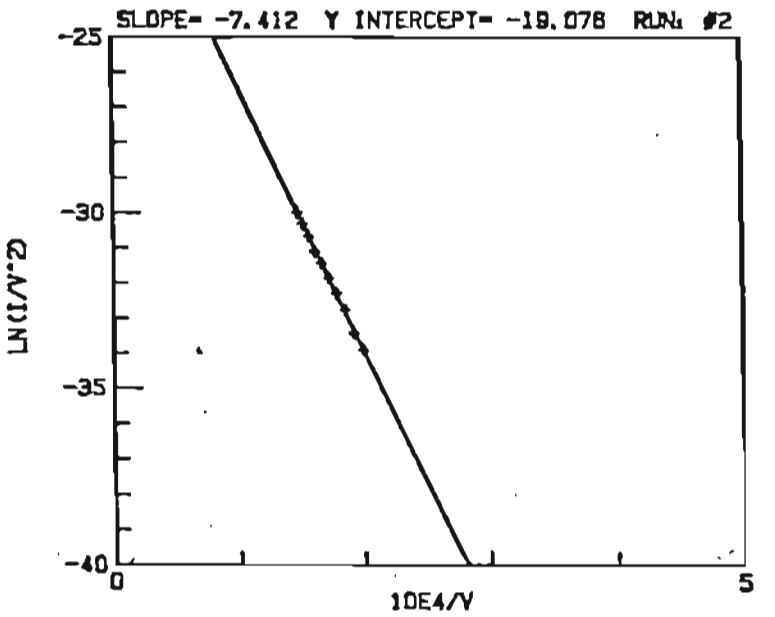

Fig. 45: F-N plot of emitter E6 after field and thermal desorption.

iii) Neon Ion Sputtering and Results

As previously stated, more than two dozen etched emitters have been examined. During this time many attempts were made to obtain a reproducible and symmetrical field emission pattern. Combinations of flash heating from moderate to high temperatures, extended heating to outgas and field desorption at voltages to 30 kV were tried. In each case and with every combination of procedures the desired result was not obtained. What finally was the key procedure in developing a symmetrical and stable emitter end form turned out to be Ne ion sputtering.

Several articles by Kubby and Siegel[17] on ion bombardment structuring of tungsten emitters have been published. Similar papers dealt with the theory and practice of emitter sharpening by ion milling. In addition Janssen and Jones[18] published a paper describing the use of neon ions formed by collisions with field emitted electrons. A third paper[19] was also found where He ion sputtering was used.

As computed by Janssen and Jones the reduction rate of the radius of a tungsten tip is proportional to the neon pressure as given by

$$- dr/dt = K P_{Ne} \qquad (29)$$

where $K = 4.6 \times 10^5$ A/min/torr, using a sputtering current of 10^{-5} A. They found a non-linear dependence upon the emission current. They

reported using a neon pressure of 5×10^{-5} torr.

To date we have used a similar technique with several different ZrC emitters. After evacuation and thermal cleaning, the emitters have been viewed in the FEM. Attempted field desorption and repeated flashings generally have not yielded a "clean" symmetrical pattern. I(V) data are taken to detect changes in emitter end-form. Neon pressures used have been between 0.5 to 10 $\times 10^{-5}$ torr with a typical pressure being 5×10^{-5} torr. Usual sputtering times ranged from 5 to 30 minutes. After which time re-evacuation, tip cleaning through heating and "field desorption", and taking I(V) data is performed.

The best pattern emerged from twice bombarding with neon ions for 20 minute intervals. The sequence of events leading to the pattern as shown in Figure 46 is listed below in Table XV.

TABLE XV: Field Emission Tip Cleaning Procedure

Procedural step	I(V)
after thermal & F-D cleaning	0.5 uA at 3 kV
neon sputtering 9×10^{-5} torr for 20 minutes	--------
after flashing	0.5 µA at 2400 V
after 30 kV F-D	0.5 µA at 3900 V

Drastic pattern changes noted.

after flashing	0.5 μA at 2700 V
after thermal F-D cleaning	0.5 μA at 4500 V
Pattern "almost" as in Fig. 46	
neon sputtering 5 x 10^{-5} torr	
for 20 minutes	--------
after thermal & F-D cleaning	5.0 μA at 5 kV

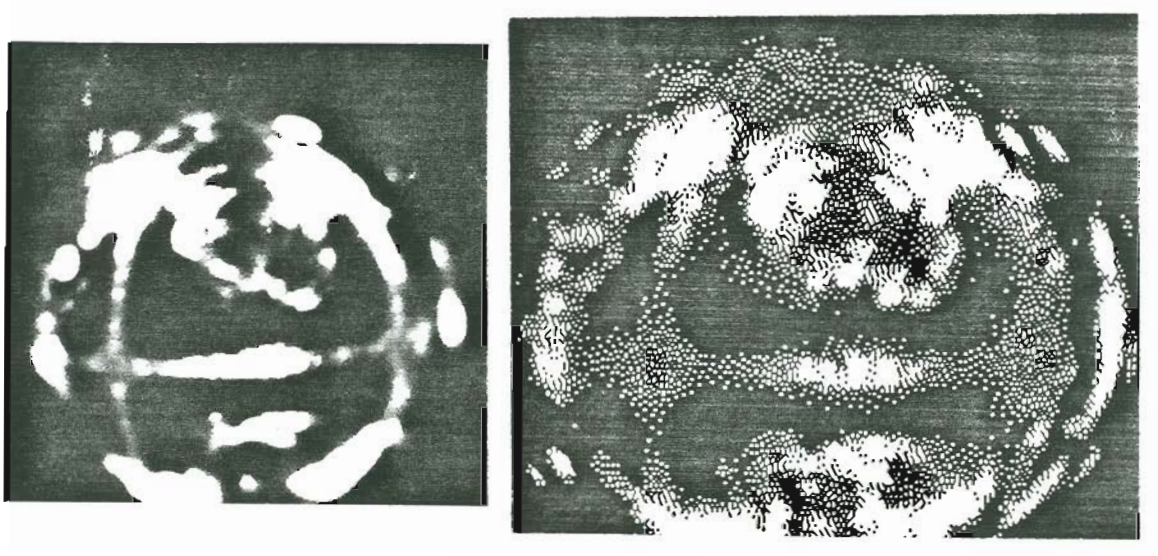

Polaroid photo (focus and reproduction have impaired quality)

Video frame, contrast enhanced and printed using MacVision

Fig. 46: ZrC emitter #104 after neon ion sputtering (approximate C/Zr ratio; 0.92) Note; axis approximately [110], two (100) planes (4-fold symmetry) located on either side of central (110) plane (2-fold symmetry).

It is interesting to note that the pattern only emerged after the attempted 30 kV field desorption. Thermal flashing alone (to approx. 1700 C) did not yield the desired "clean" emitter end-form. In each case where a symmetrical pattern has been obtained a series of neon sputtering, "field desorption", and thermal flashing has been employed. (The term "field desorption" has been given in quotes because for a 3 to 4.5 kV tip, r = 0.35 μm, 30 kV does not seem high enough for true field desorption of the emitter surface. However, some desorption of protrusions and/or other surface irregularities evidently takes place.)

Figs. 47 and 48 show the changes in emitter end shape due to neon ion sputtering for two emitters. In Fig. 47, the "q-tip" shape has been sputtered back to yield the smooth end giving the pattern shown in Fig. 46. (and F-N of Fig. 49) Fig. 48 has changed to show a terraced step end-form. This is somewhat similar to that found in neon sputtering of W as reported by Janssen and Jones. The stepped form could be explained by the differential sputtering rates along different crystallographic directions.

Repeated thermal cleaning dulled the emitter to give 0.6 μA at 5800 V. After allowing the emitter to be exposed for >24 hours to pressures of 1×10^{-9} torr, the first Fowler-Nordheim data were taken. Upon thermal cleaning and "field desorption", the second set of data were taken and are displayed in Fig. 49.

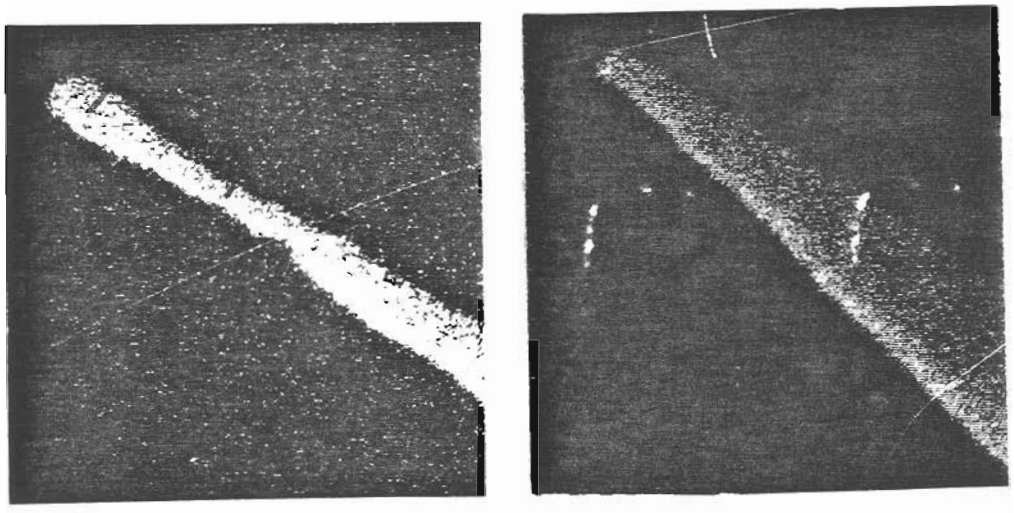

Fig. 47: ZrC emitter #104 before and after neon ion sputtering. Magnification (tip radius)

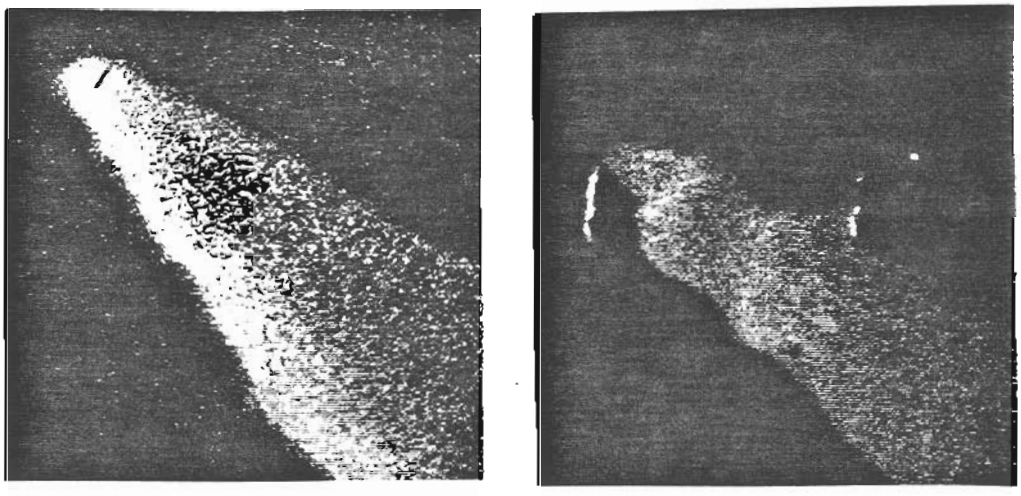

Fig. 48: ZrC emitter #108 before and after neon ion sputtering. Note terraced steps after sputtering. Magnification (tip radius)

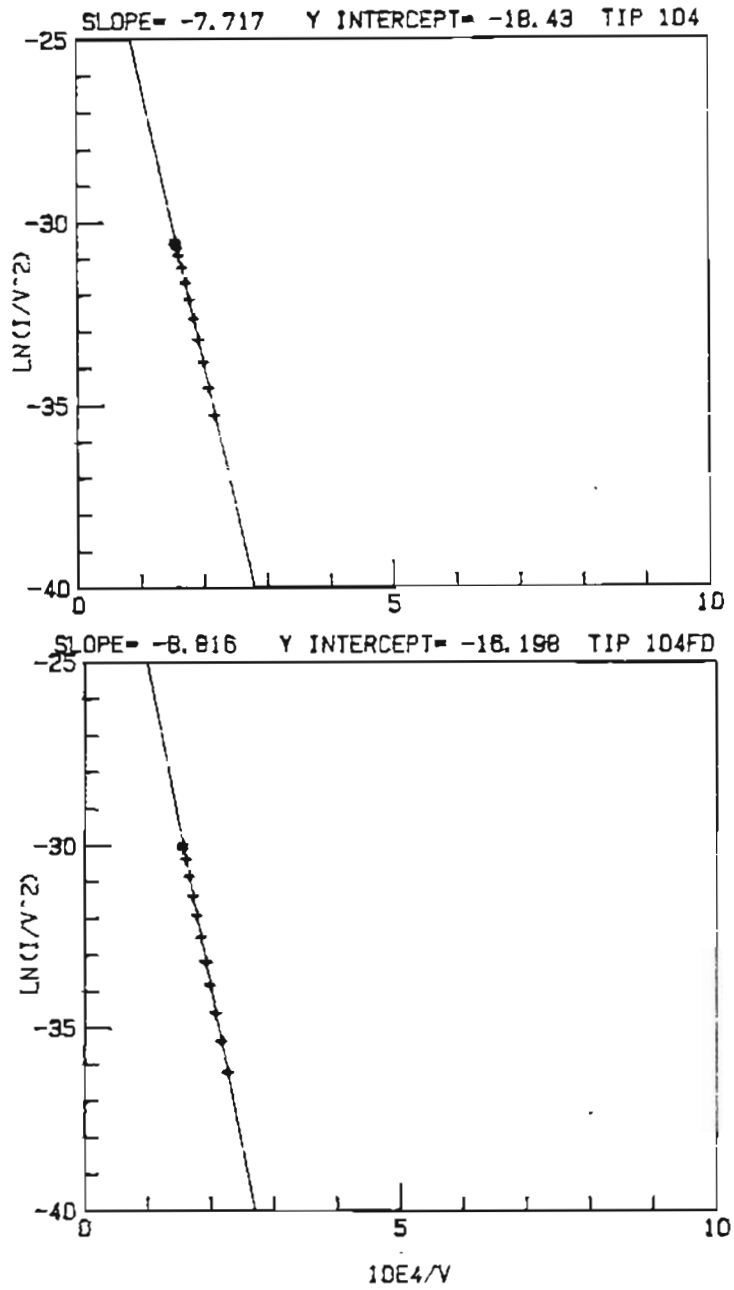

Fig. 49: Fowler-Nordheim plots of ZrC emitter #104. Top; after exposure to 10^{-9} torr for >24 hours but before heating or F-D. Bottom; after heating and 30 kV F-D.

iv) Discussion of FEM Results

Determination of the average work function from the Fowler-Nordheim plots is difficult due to the uncertainty in the beta factor as discussed earlier. While the micrographs yield tip radius and cone angle values, there is error in them and in the form taken by β.

Even though uncertainties exist, we can use a value for the β-factor as contained in Eq. (27), ie. $\beta = 1/5r$. From the Fowler-Nordheim plots, the slope can be equated with $\phi^{3/2}$ as was presented in section IIC. From Eq. (24), we see that the slope of the F-N plot is

$$m_{F-N} = b\phi^{3/2}/\beta \qquad (30)$$

were $b = 2.66 \times 10^7$. With r given in centimeters, ϕ would be given in eV.

Solving Eq. (30) for ϕ therefore yields

$$\phi = [m_{F-N}/2.66 \times 10^7(5r)]^{2/3} = 3.838 \times 10^{-6}(m_{F-N}/r) \qquad (31)$$

Table XVI contains the results of these calculations derived from the F-N plots already given.

TABLE XVI: Calculated Field Emission Work Function

Averages over Exposed Crystallographic Directions

F-N Fig. Number	Emitter #	r (cm)	m_{F-N} (x 10^4)	ϕ (eV)
42	E6	9×10^{-5}	4.152	2.29
43	"	"	4.05	2.25
44	"	$\sim 9 \times 10^{-5}$	7.54	3.41
45	"	"	7.412	3.37
49 a	104	4×10^{-5}	7.717	5.95
49 b	"	$\sim 4 \times 10^{-5}$	8.816	6.50

The current as a function of time was also monitored. While there is initial decline, the noise level of the total emitted current was approximately 4%. This seemed quite good considering a pressure of 5×10^{-9} torr during much of the 2 hours in which the current was monitored.

Further data will need to be gathered to establish trends with any certainty. From the pattern, it would appear that the (110) work function is lower than that of either the (100) or (111) crystal planes.

To generate these distinctions, a clean, reproducible pattern is needed as well as I(V) data from each plane via a FEM probe tube.

D. THERMIONIC EMISSION MEASUREMENTS

i) Thermionic Theory

Through the heating of a metal and its surface, electrons are thermally induced to occupy higher energy levels. If the temperature is high enough to excite Fermi sea electrons to energy levels above the potential barrier at the metals surface, then they are free to escape. The current density of these emitted electrons is a function of the temperature of the metal as well as the "surface" work function. This current density is given by Richardson's equation,

$$J = A(1 - r)T^2\exp(-e\phi/kT). \qquad (32)$$

The factor A is a constant, $(4\pi ek^2/h^3)$, equal to 120 A $cm^{-2}deg^{-2}$, and r is the reflection coefficient. This latter factor may be included to account for any quantum mechanical reflection possible as electrons arrive at the potential barrier.

In order to overcome space charge, that is the build-up of electrons at the cathode surface, an electric field needs to be applied. This field however would tend to lower the potential barrier at the surface and increase the current density over that predicted by Richardson's equation at some given temperature. The potential lowering is known as the Schottky effect and the added field changes the equation for the

current density to

$$J = A(1 - r)T^2\exp\{-e[\phi - (eF)^{1/2}]/kT\}, \qquad (33)$$

where F is the applied field.

To overcome this added complexity, the current density is extrapolated to a zero field value. This is done with the aid of Schottky plots, ln(I) versus $(V)^{1/2}$ for a given temperature. Computer generated least squares fitting is used on the linear portion of the curve to obtain the theoretical current available when the field is zero.

A standard Richardson plot of $\ln(J/T^2)$ against 1/kT, shown later in Figs. 68 and 69, which yields a slope equal to $-e\phi$ and a $\ln(J/T^2)$ intercept equal to the constant A, could then be used in analyzing these data. However if a temperature dependence to the work function is anticipated, an alternate method is employed. The Richardson equation constant is assumed to have the value of 120 A $cm^{-2}deg^{-2}$ and the reflection, which should be small, is assumed to be zero.

With the current density given as the current (I) divided by the emitting area (a) the remaining Richardson's equation can be solved for the work function, yielding

$$\phi_e = -kT \ln[I/(120aT^2)] \qquad (34)$$

Here k is Boltzmann's constant, $k = 8.617 \times 10^{-5}$ eV/K. Equation (34)

yields what is known as the effective thermionic work function, ϕ_e, which can be determined as a function of T.

ii) Experimental Systems

1) Thermionic Projection Microscope Tube

A thermionic emission microscope (TPM) tube was utilized to investigate the variance in work functions found over various crystallographic directions. This method has been used to examine the thermionic emission patterns of LaB_6.[20]

Light emitted from the incandescent ZrC crystal would mask the pattern on a conventional FEM tube, an alternate system had to be devised. An old FEM tube was modified for this purpose, by using an opaque conductive coating made of vapor deposited aluminum and a heavier and opaque phosphor material. A drawing of this tube is given in Fig. 50.

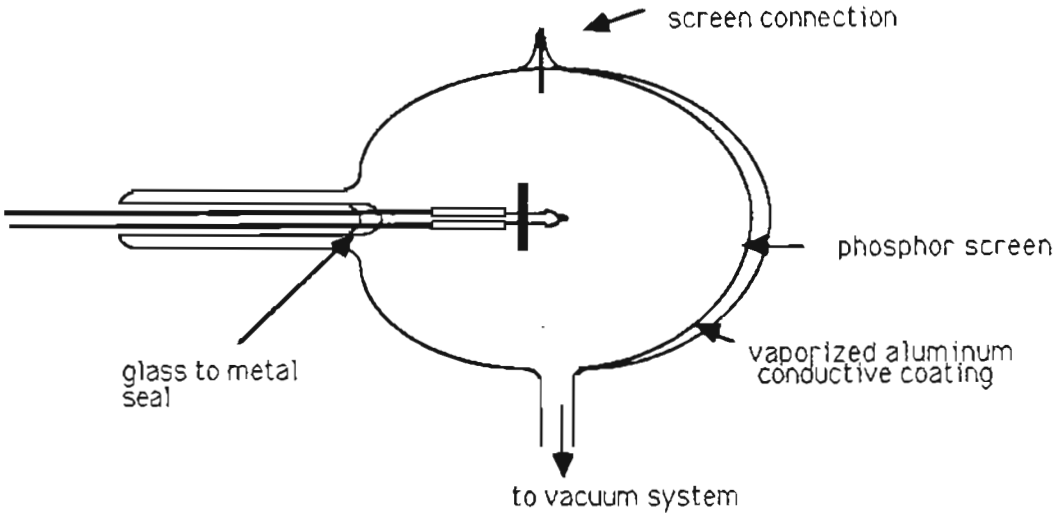

Fig. 50: Thermionic projection microscope tube.

2) Effective Work Function Samples

The apparatus used for the thermionic work function measurements was contained within a 1.5 inch diameter stainless steel cross evacuated through one 2.75 inch flanged port. Viewing and temperature measurements were made through a pyrex window on the opposite port. The collector was mounted on the bottom port and consisted of a massive Cu, electrically insulated rod with a W insert in the center. The emitter base assembly was flange mounted through the top port. (see Fig. 51)

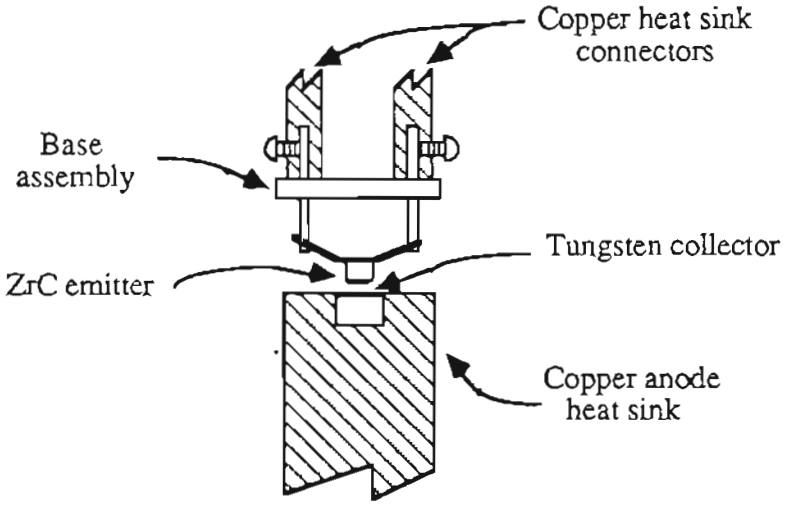

Fig. 51: Cross section of emitter/collector apparatus. Typical spacing between emitter and collector was 0.010 to 0.020 inches.

The electrical circuitry consisted of a current regulated filament supply, a 10 kV pulser which supplied a 20 μs wide pulse with 20 ms

between pulses, and a two channel oscilloscope. A precision resistor calibrated to five significant figures was used to measure current. The circuit is depicted in Fig. 52.

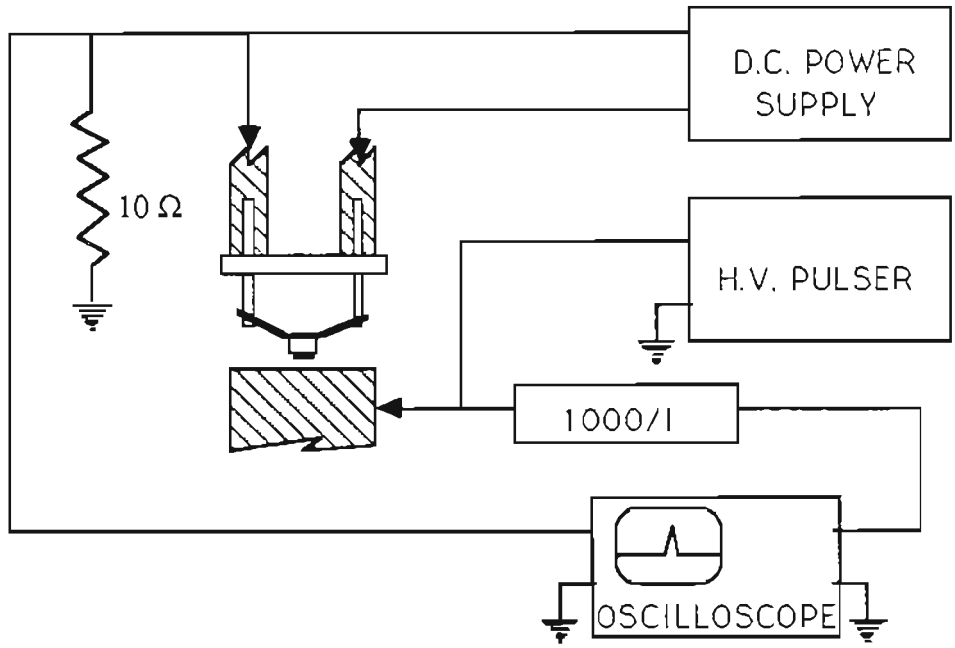

Fig. 52: Circuit diagram for current/voltage measurements of thermionic emission.

iii) Results

1) Thermionic Projection Patterns

The results of analyzing the pattern taken from the screen of the thermionic projection microscope gives a vivid depiction of the variation in surface work function over different crystal planes. In addition it also is useful in determining the relative changes brought about by the adsorption of gas on the surfaces of a ZrC crystal.

Fig. 53a shows the pattern of a clean surface, after the crystal was heated to temperatures greater than 1700 C. At this temperature most surface contaminants are removed as has been verified by AES. Beside the photo (see Fig. 53b), is a crystal plane map indicating the planes observed in the photo of the screen. Through inspection of this photo, relative ordering of single crystal plane work functions of ZrC is possible. The observed ordering for low index planes is,

$$\phi_{(110)} < \phi_{(100)} < \phi_{(111)}.$$

The exact ordering of the higher index planes is less certain. However, the values predicted later, in Section IIIB, of the (210), (211), (310), and (311) seem to correspond to ordering observed here.

The projection microscope was also run while O_2 was admitted to the tube through a gas inlet leak valve. The O_2 was allowed to reach a pressure of 5×10^{-5} torr, and was then was pumped out. The photographs shown in Fig. 54 are a sequence showing 1) the initial clean surface, 2)

the surface during the maximum pressure of O_2, 3) the O_2 exposed surface after a moderate amount of heating to approximately 1500 C and 4) the O_2 exposed surface after repeated thermal cleaning to at least 1700 C.

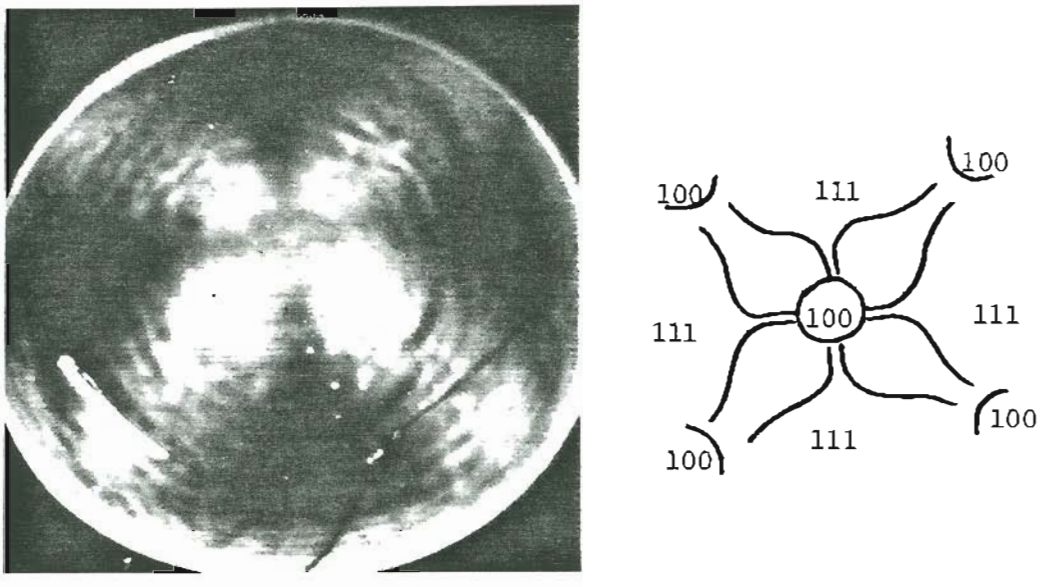

(a) (b)

Fig. 53: a) Hemispherical thermal emitting microscope image of clean zirconium carbide. b) Depiction of the same image with crystal planes identified.

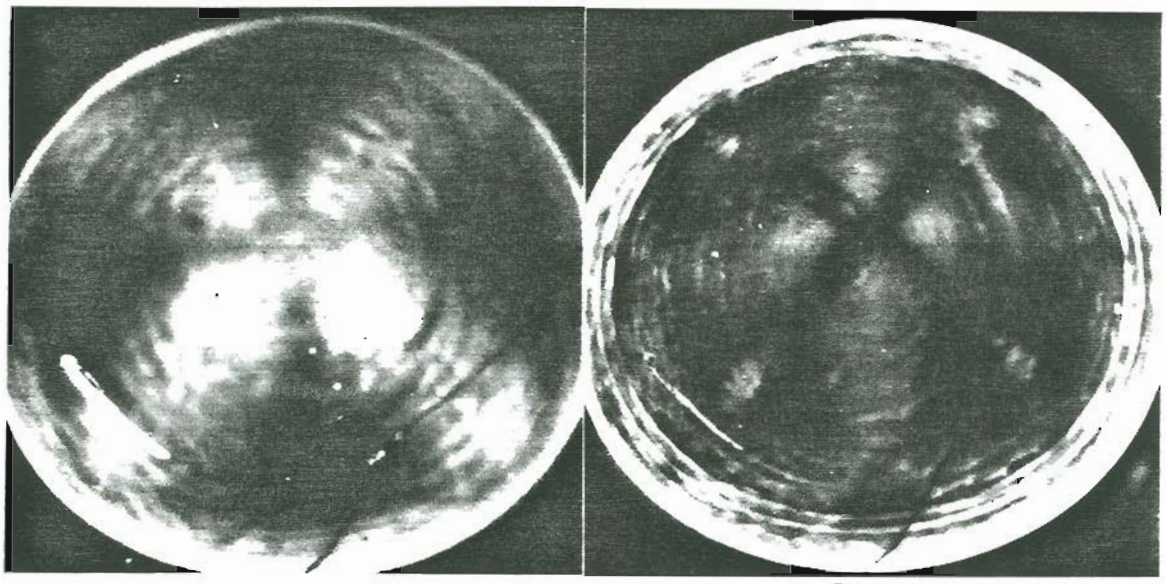

Before O_2 exposure

During 10^{-5} O_2 exposure

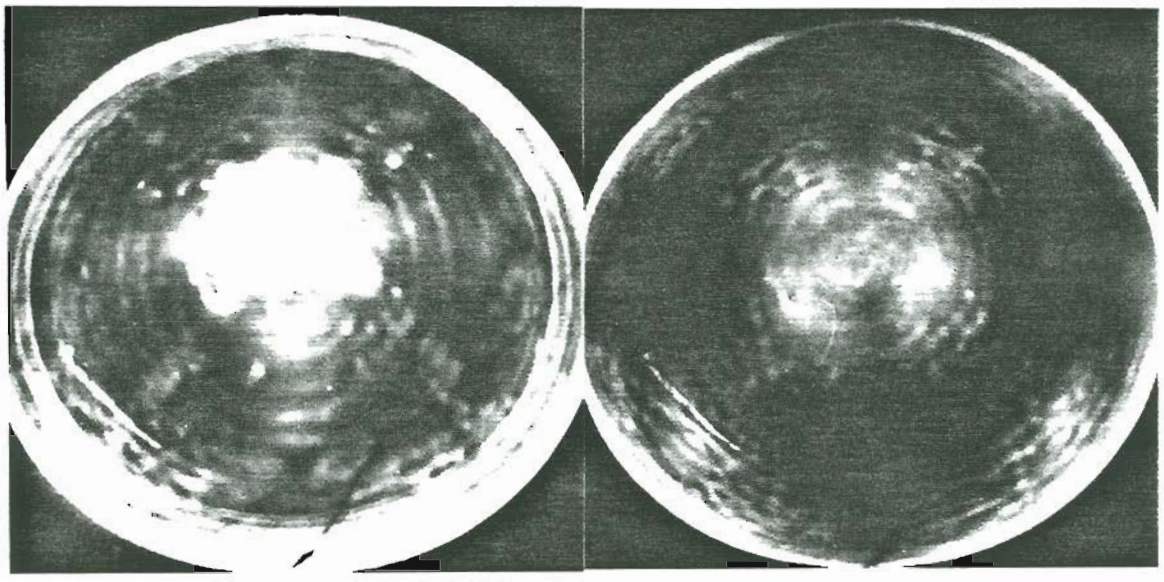

After 1400 K heating

After extended 2000 K heating

Fig. 54: Sequence of photographs showing the work function distribution before, during and after oxygen adsorption. Crystal planes can be identified by referring to Fig. 53b.

As can be seen, O_2 adsorption drastically changes the emission pattern from that of a clean surface. It is interesting to note that the ordering of work function values of the different crystal planes has almost reversed over that of a clean surface. If the assumption which will be made in the prediction model development is valid (see Section IIIB), the odd planes have C outermost on the clean surface. Hence, with the addition of O_2 a Zr oxycarbide may be formed, with an associated lowering of the work function on some of the crystallographic directions.

Note that the final pattern resembles the initial clean one, but is not exactly the same. This result could be due to Zr-O bonding in the vacant surface carbon lattice sites, a possibility which will be discussed in more detail in a following section.

2) Single Crystal Effective Work Functions

Thermionic work function measurements have been performed on five ZrC crystal samples prepared as discussed in Part One. The C to Zr ratio of the zone melted material averaged 0.896. Current/voltage data were taken for temperatures in the range 1800 to 2500 K and were analyzed using Schottky plots and Richardson's equation with the pre-exponential constant equal to 120 $A\text{-}cm^{-2}K^{-2}$ as discussed earlier. Best results were obtained from measurements of the (100) and (210) crystal planes. These results are plotted to show the temperature dependence of the work function.

The first crystal to be examined was heated only to 1600 K to outgas components and clean the surface. Data were taken at this and increasingly higher temperatures. As a result of this low temperature cleaning the data yield a wide variation in the work function.

In retrospect, this variation should not have been surprising. In the studies done on the large (100) oriented single crystal of zirconium carbide, wide variations of the work function were found until the surface was cleaned of oxygen and other adsorbates. Those studies used the FERP method of determining the work function and AES for determining surface contaminant levels. Prom that study, oxygen levels did not decline to acceptable values (<1%) until temperatures of >1800 K were reached.

Because of prior studies and the variations obtained with the

first sample, all subsequent samples were thermally cleaned prior to the taking of any data. This cleaning was done after the sample was mounted in the experimental thermionic apparatus. After evacuation to $<2 \times 10^{-8}$ torr, the sample was typically heated in the 1900-2000 K range for a period of approximately 3 hours. After this treatment, the work function variations were reduced or eliminated. Emission current, and therefore the work function, remained virtually constant over time at the initial temperature of around 2000 K.

After the thermal cleaning described earlier, the voltage across the signal resistor was measured at various anode potentials, starting at the thermal cleaning temperature. These data points were taken from alternating scope traces at identical delay times, toward the end of each pulse.

Two pyrometer readings were made, before and after each I(V) run. The filament current was then increased, with temperature and I(V) data again taken. This process was repeated usually until the filament melted. When this happened, either the filament was repaired and remounted, or a different sample was inserted into the system.

Considerable difficulties occurred at the high temperatures required for these measurements. In addition to the filaments simply melting, if a small amount of the braze material inadvertently got on the filament, the filaments were dissolved at that point and failed. These two types of filament failure were easily distinguished by inspection. The Co etched the filament, while melting smoothly rounded the wire ends.

To obtain temperatures >2500 K the proper relation of radiative heat loss from the crystal sample and conductive heat loss from the support rods needs to be achieved by careful balance of the filament size, thermal conductivity and resistivity. Ideally, the aim was to keep the cup at the hottest spot on the filament.

The collected data were analyzed and plotted with the aid of a Hewlett-Packard 86B computer. Schottky plots are shown in Figs. 55 to 63. Points which fall below the Schottky line due to space charge effects at low voltages were eliminated by visual inspection. The remaining points were used for a linear least squares fitting using the computer.

Once the Schottky plots and straight line fit had been obtained, the extrapolated zero field current (log I-intercept) was used to obtain the work function using Equation (34) as described earlier. The area was calculated from dimensions obtained prior to mounting and verified using SEM micrographs.

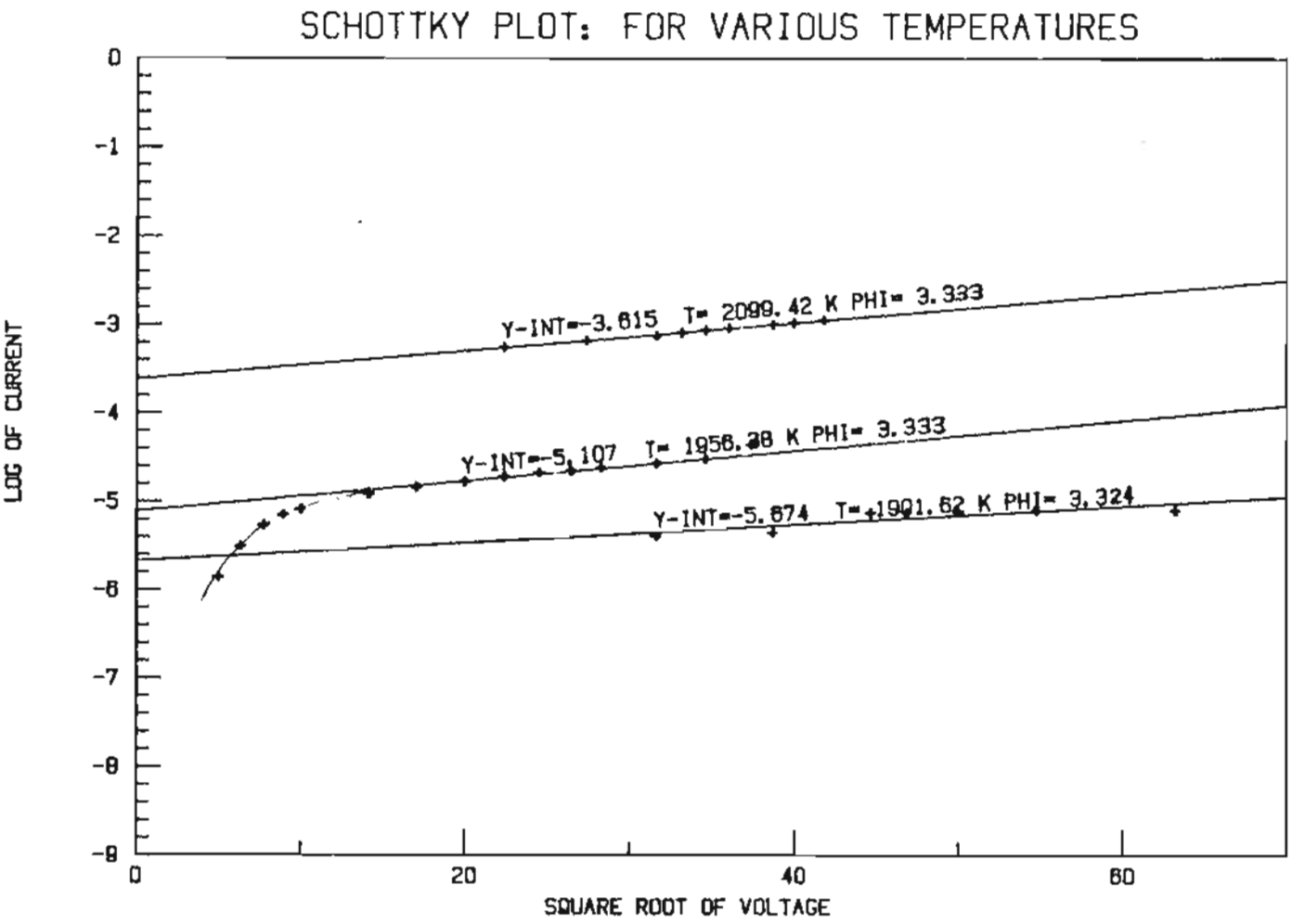

Fig. 55: Schottky plots, ZrC (100), sample 1, run 1.

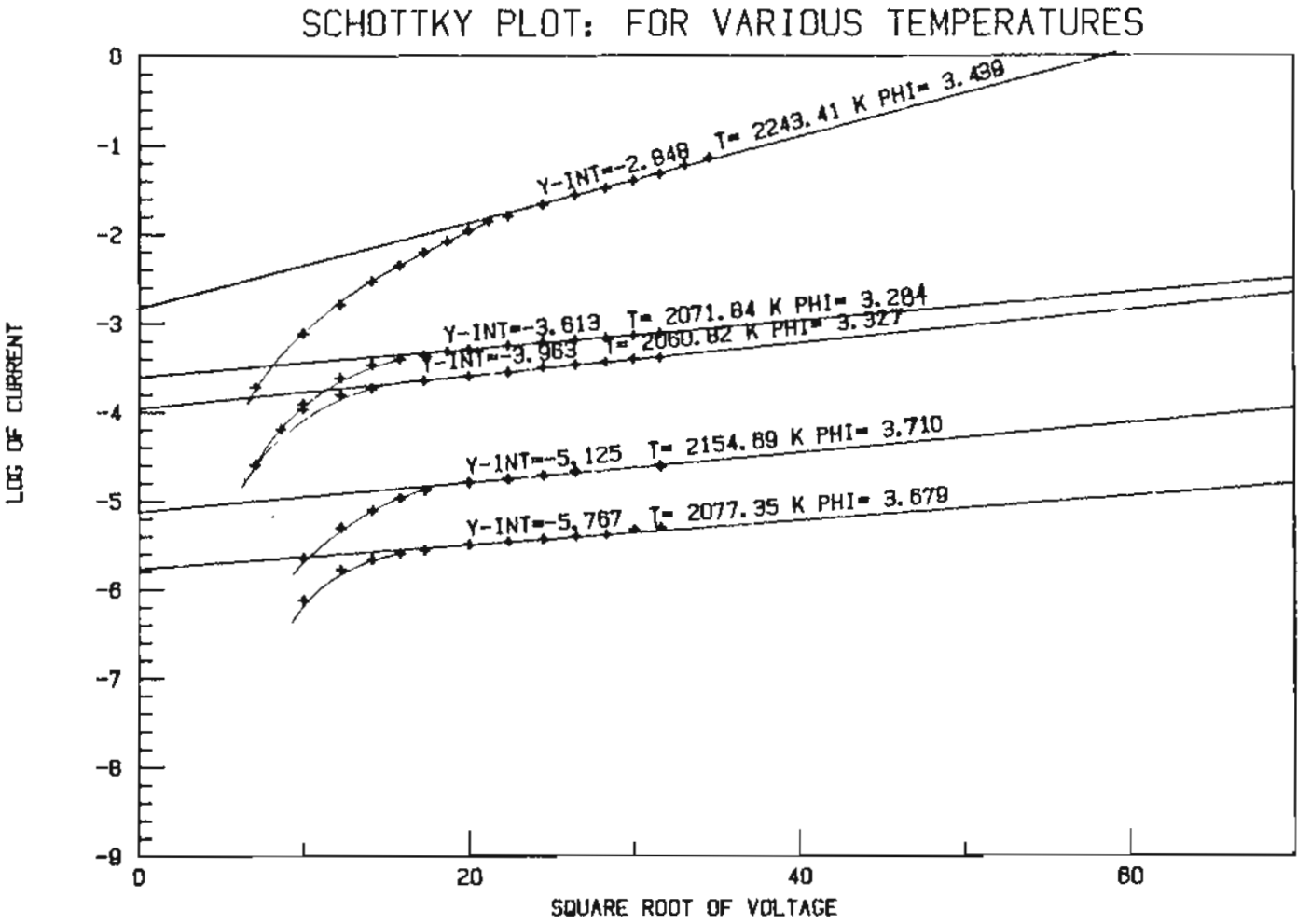

Fig. 56: Schottky plots, ZrC (100), sample 1, run 2.

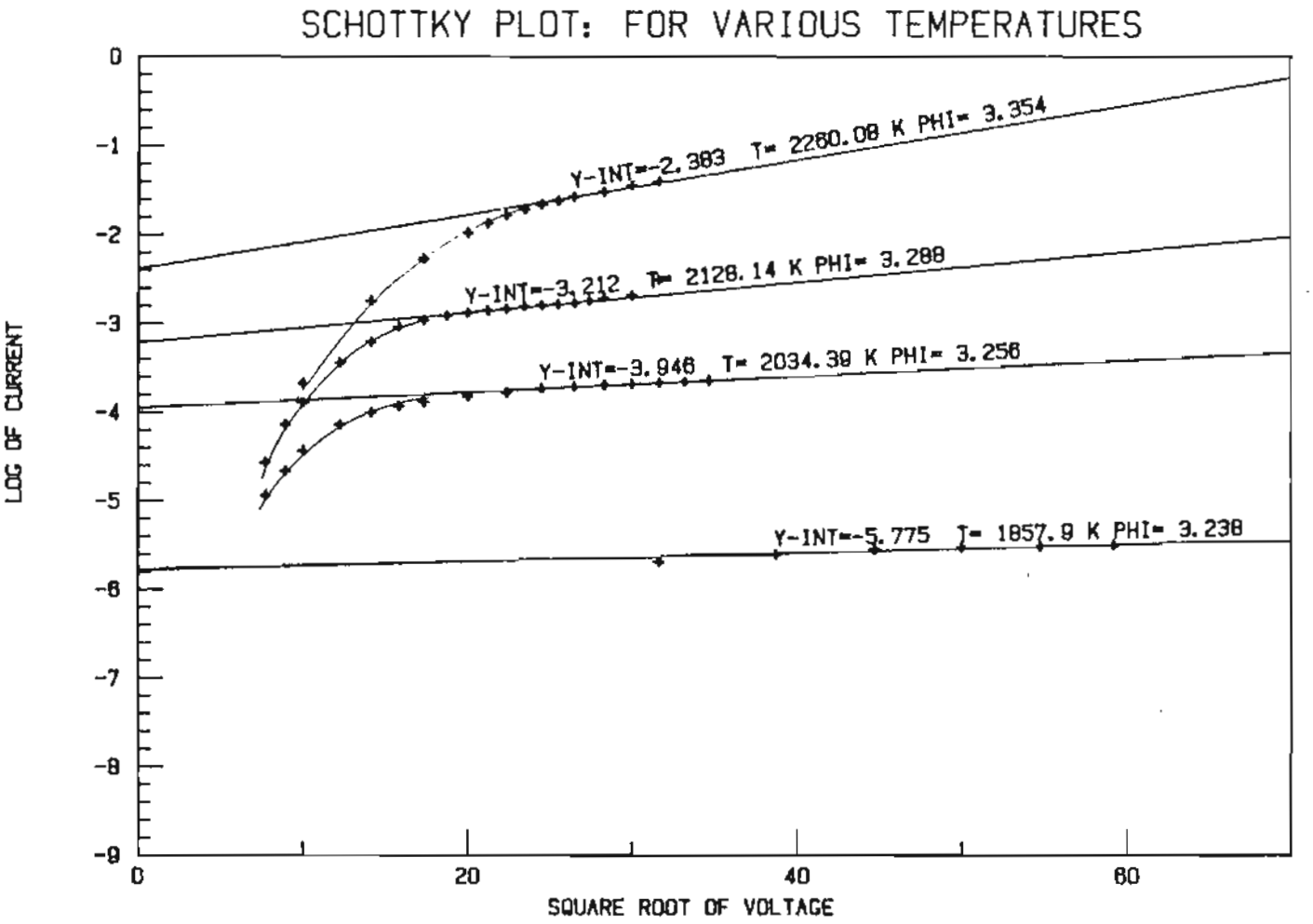

Fig. 57: Schottky plots, ZrC (211), sample 2, run 1.

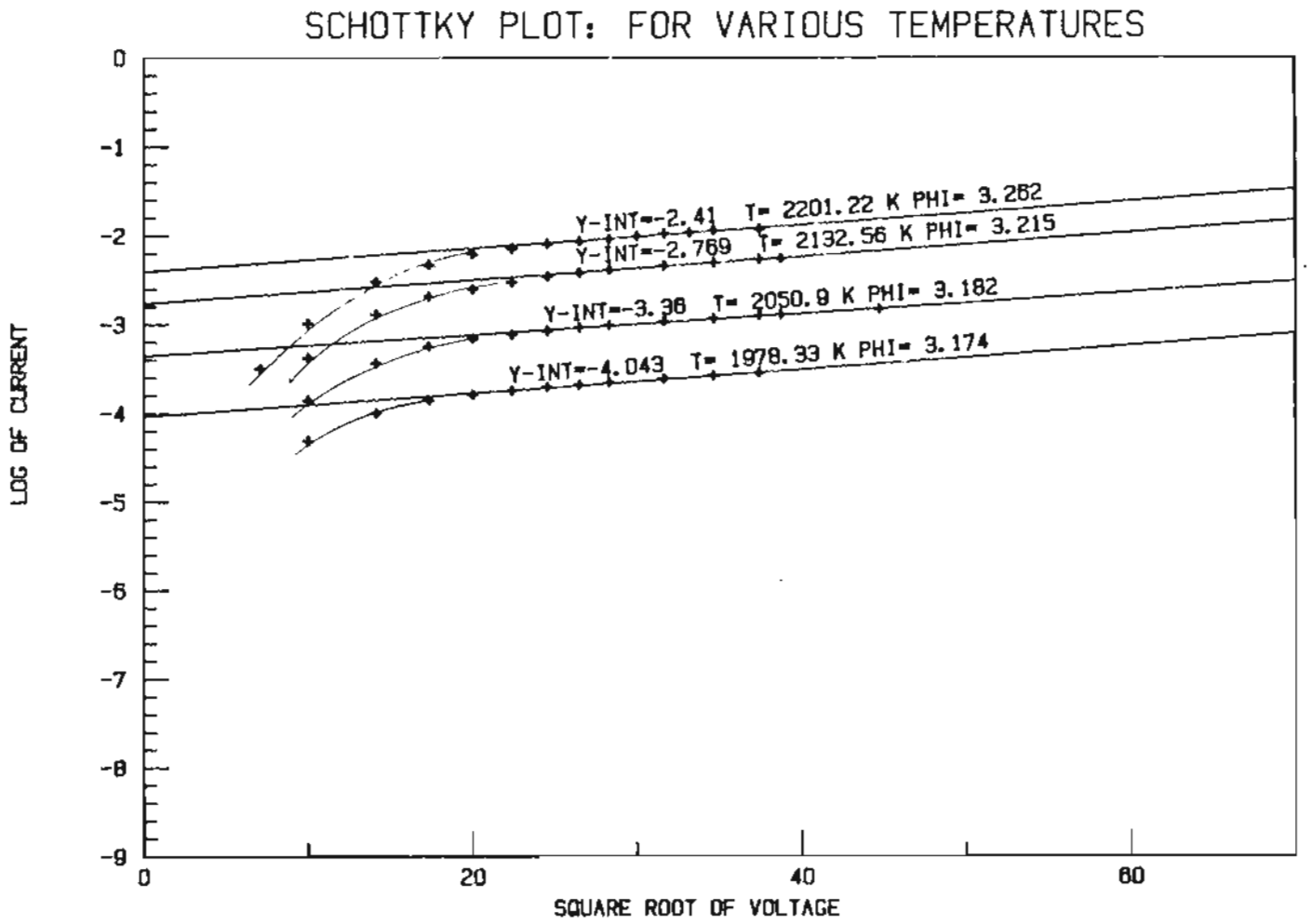

Fig. 58: Schottky plots, ZrC (211), sample 2, run 2.

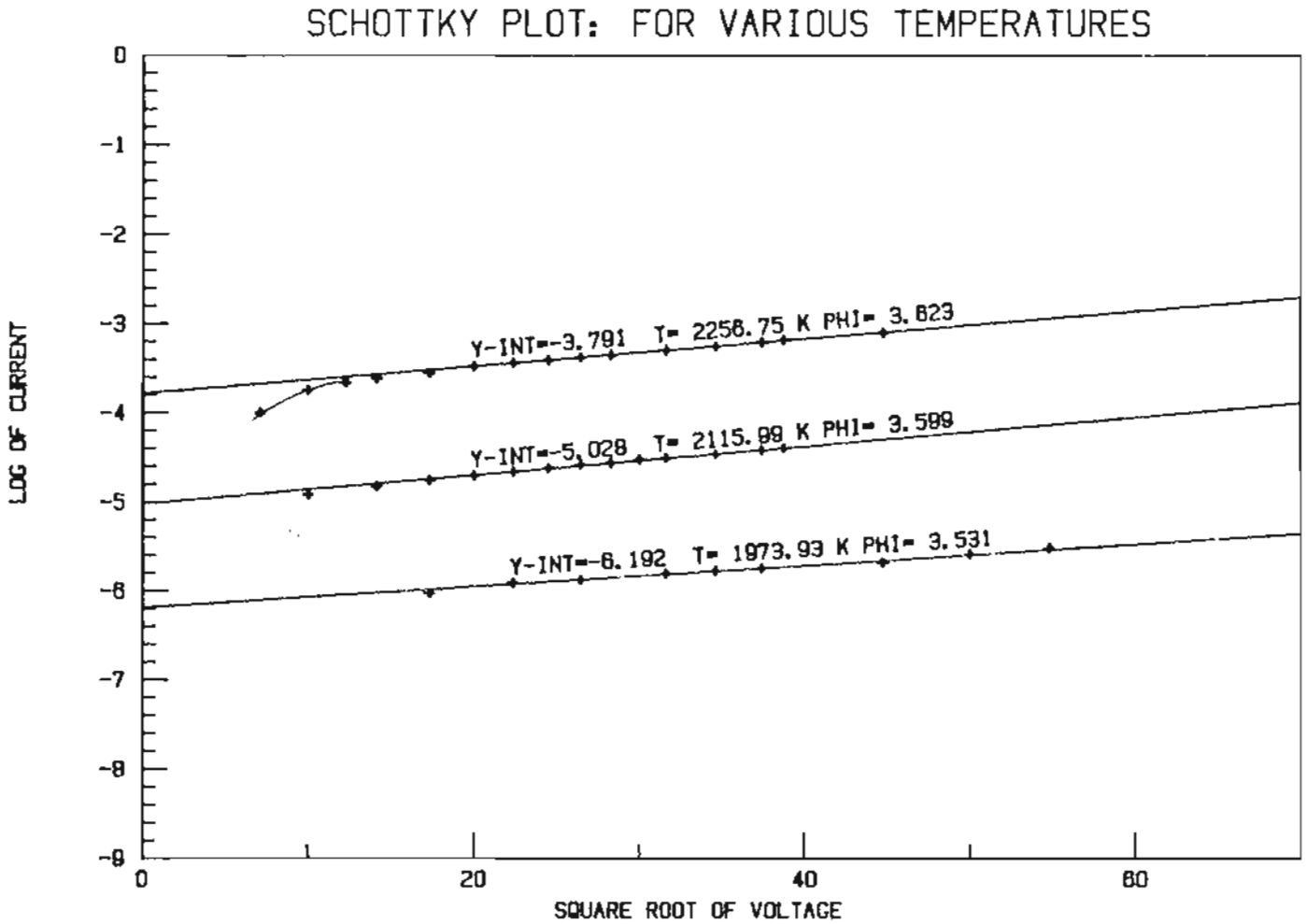

Fig. 59: Schottky plots, ZrC (100), sample 3, run 1.

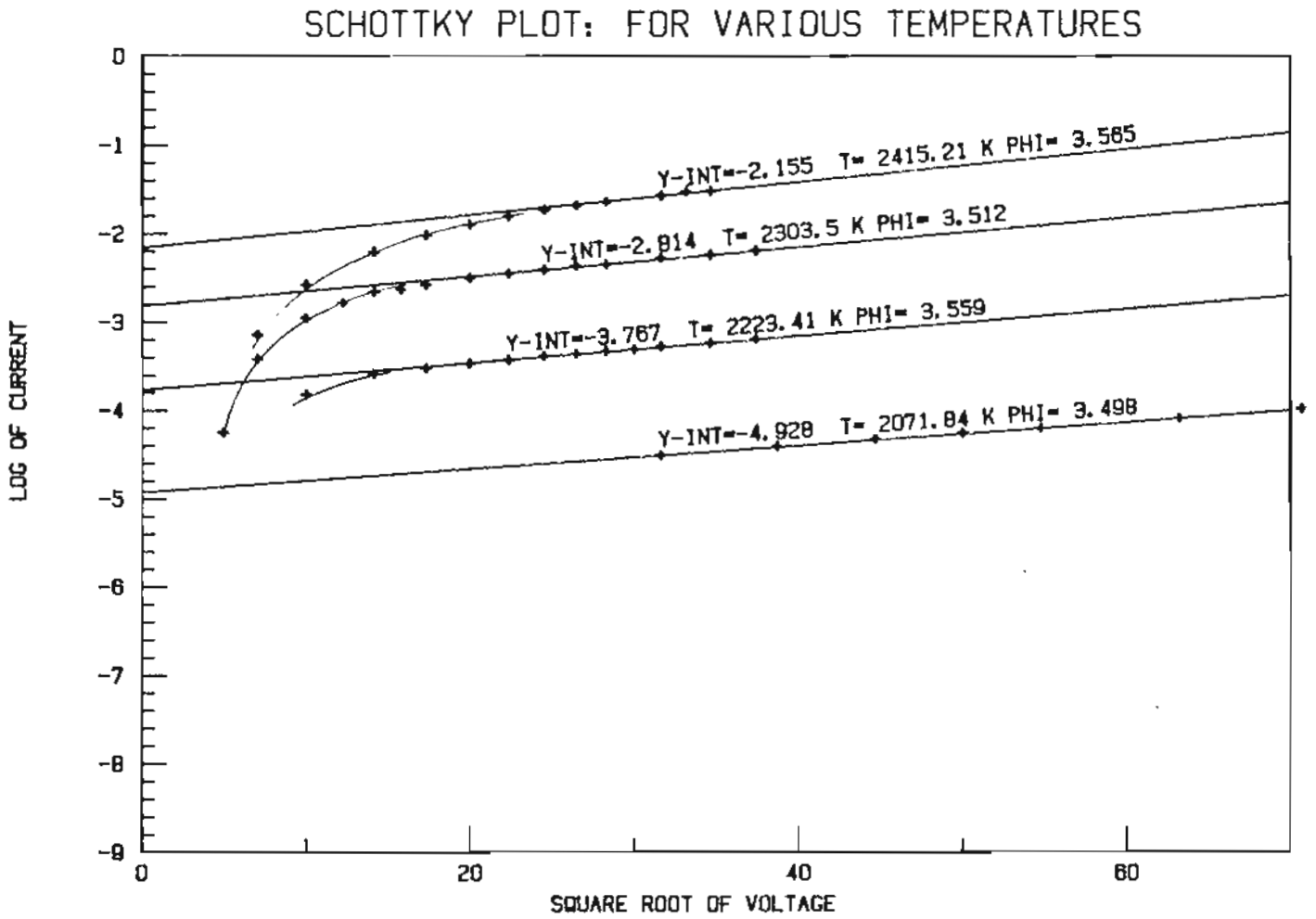

Fig. 60: Schottky plots, ZrC (100), sample 3, run 2a.

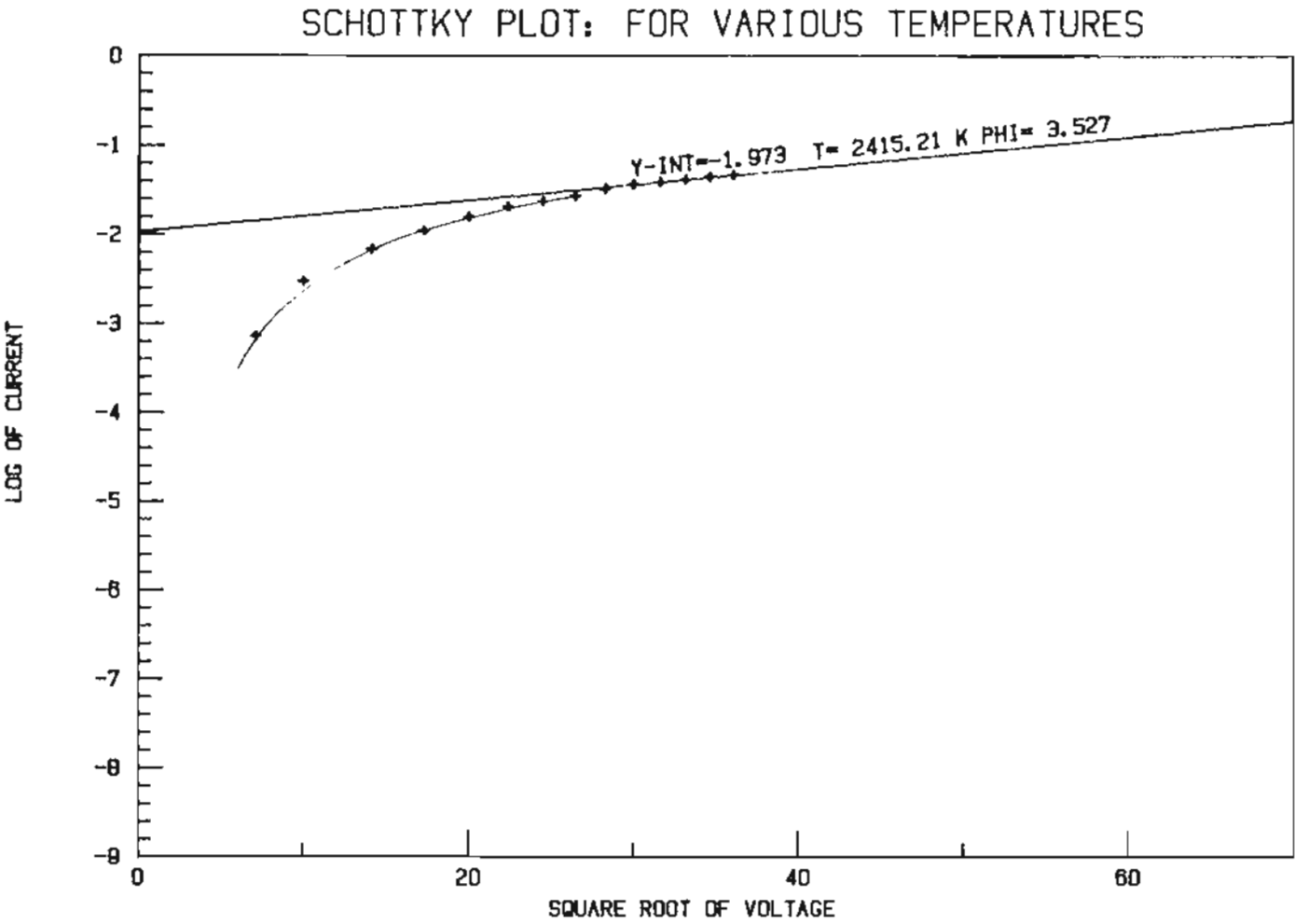

Fig. 61: Schottky plot, ZrC (100), sample 3, run 2b.

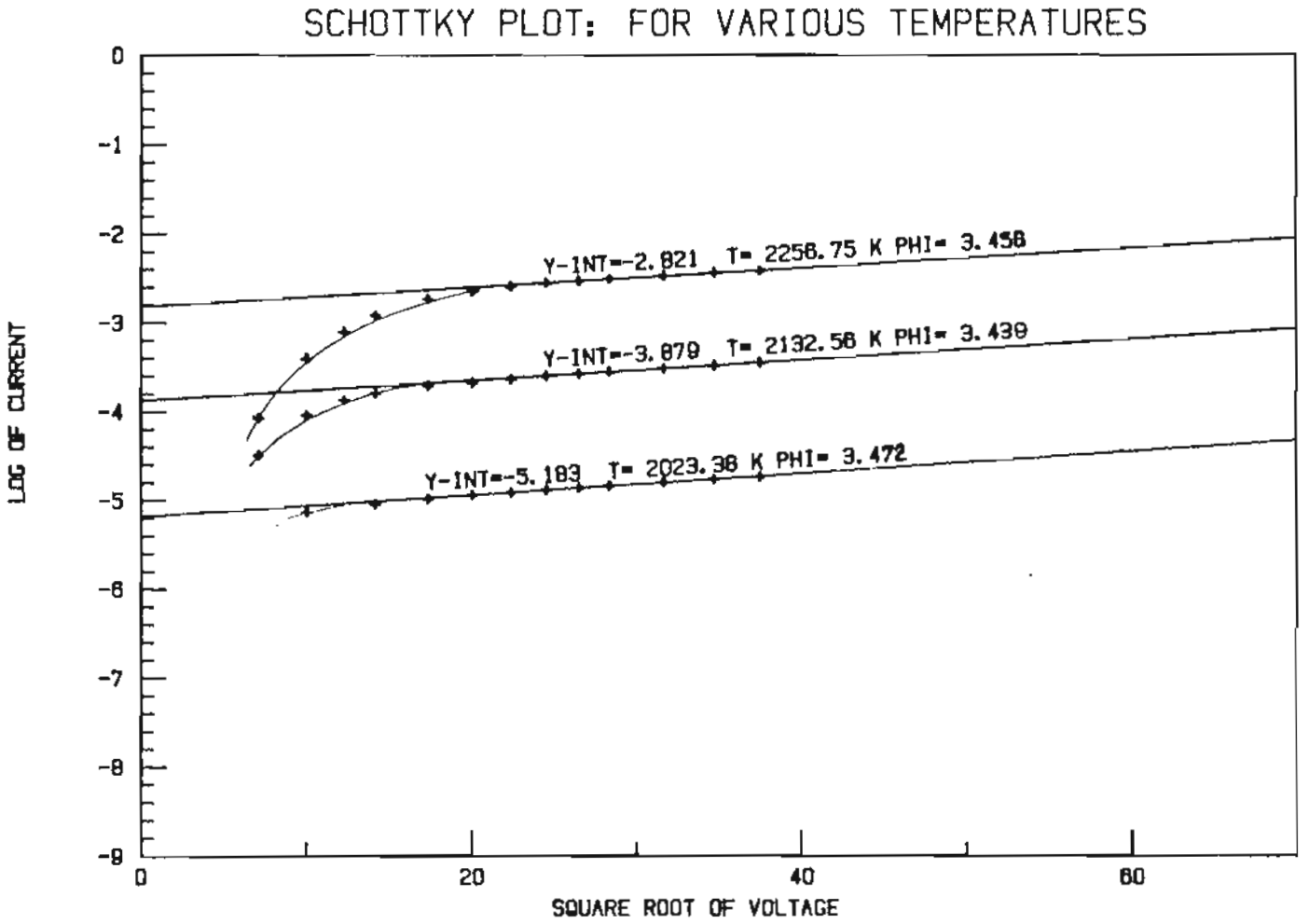

Fig. 62: Schottky plots, ZrC (100), sample 4.

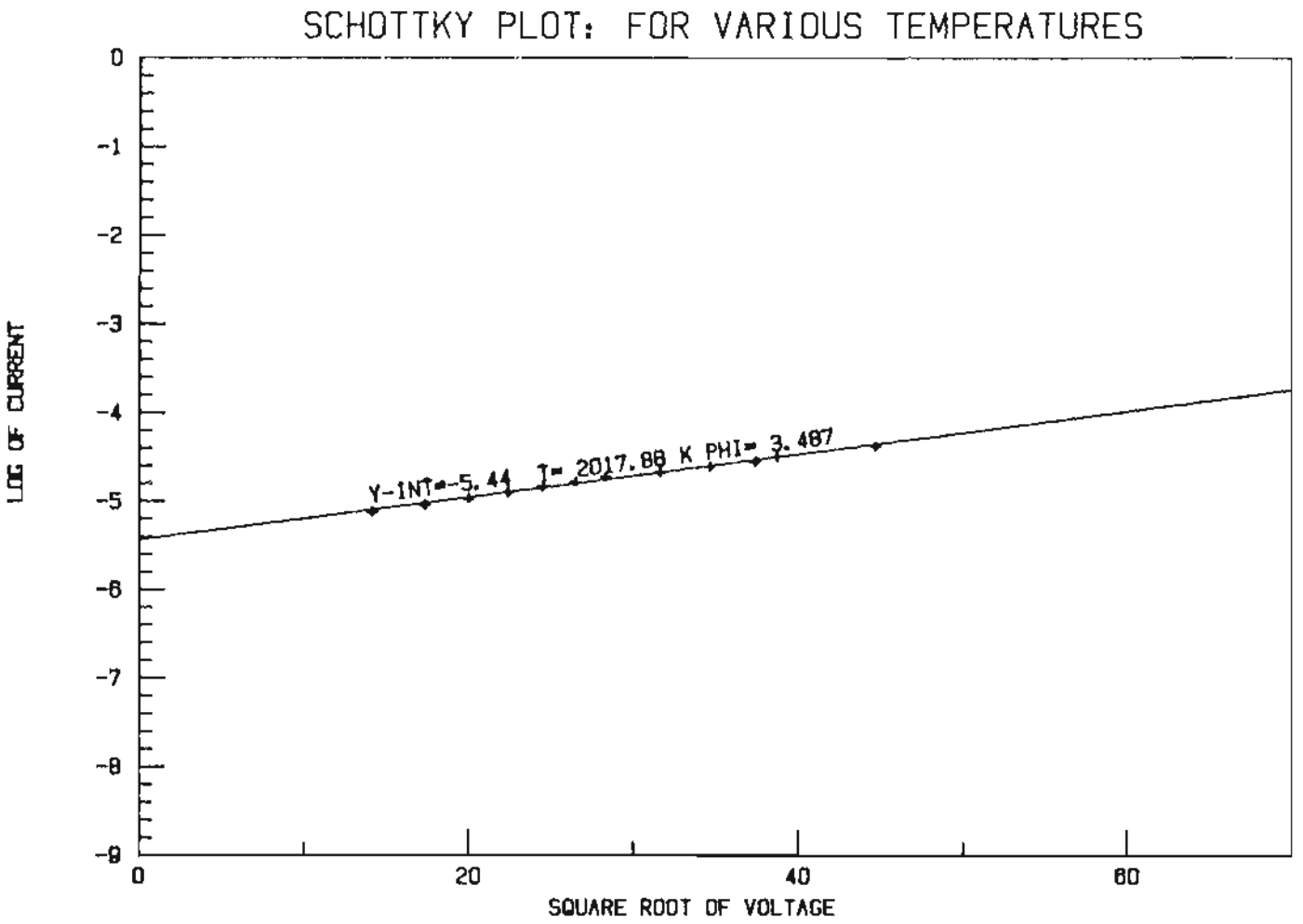

Fig. 63: Schottky plot, ZrC (311), sample 5.

The temperature conversion from degrees Celsius brightness pyrometer reading to true temperature in degrees Kelvin was made using the formula[21]

$$T(K) \simeq (C/\lambda)/\{\ln[\varepsilon \exp(C/\lambda T_{br})]\} \quad (37)$$

where $C/\lambda = 2.212 \times 10^4$ degrees for $\lambda = 0.65$ μm radiation wavelength. Inserting a factor τ for the reduction in intensity due to the pyrex window ($\tau = 0.916$ for 2-5 mm pyrex), one obtains

$$T(K) = (2.212 \times 10^4)/\{\ln[\varepsilon \tau \exp(2.212 \times 10^4/T_{br})]\} \quad (38)$$

Using an emissivity $\varepsilon(T)$ function obtained from data collected in another set of experiments reported in the Appendix, we obtain the temperature and effective work function values listed on the Schottky plots. Table XVII summarizes the data, giving sample number, crystal orientation, temperature and work function ranges, and figure numbers for Schottky plots. Note that each Schottky figure represents a different run. In Figure 64 to 67, the $\phi(T)$ data are presented, sample #'s 1,3 and 4 are $ZrC_{(100)}$ and sample #2 is $ZrC_{(210)}$. Figs. 64 to 66 represent two data runs for each of the samples. Usually, the sample's filament failed at the next higher attempted temperature. As a result, the sample was removed from the vacuum system for either repair or replacement.

TABLE XVII: Data summary for thermionic work on ZrC.

ZIRCONIUM CARBIDE: THERMIONIC DATA SUMMARY

SAMPLE #	Emitting Surface On/Off Axis	Protrusion From Cup	Orientation (via Laué)	Amount Stated Orientation Off From Surface	Number Of Runs	Figure Number(s)	Temperature Range (K)	ϕ (eV) Range
1	off-axis (fractured plane, 20-30°)	~0.025"	(100)	0°	3	55,56	1750-2350	3.41-3.85
2	on-axis (ground)	0.018"	~(210)	8° (est.)	2	57,58	1900-2350	3.26-3.49
3	on-axis (ground)	0.004"	(100)	2-3°	2	59-61	2000-2530	3.61-3.77
4	off-axis (fractured plane, 25-30°)	~0.015"	(100)	0°	1	62	2080-2350	3.56-3.61
5	on-axis (ground)	0.005"	~(311)	~7°	1	63	2075	3.59

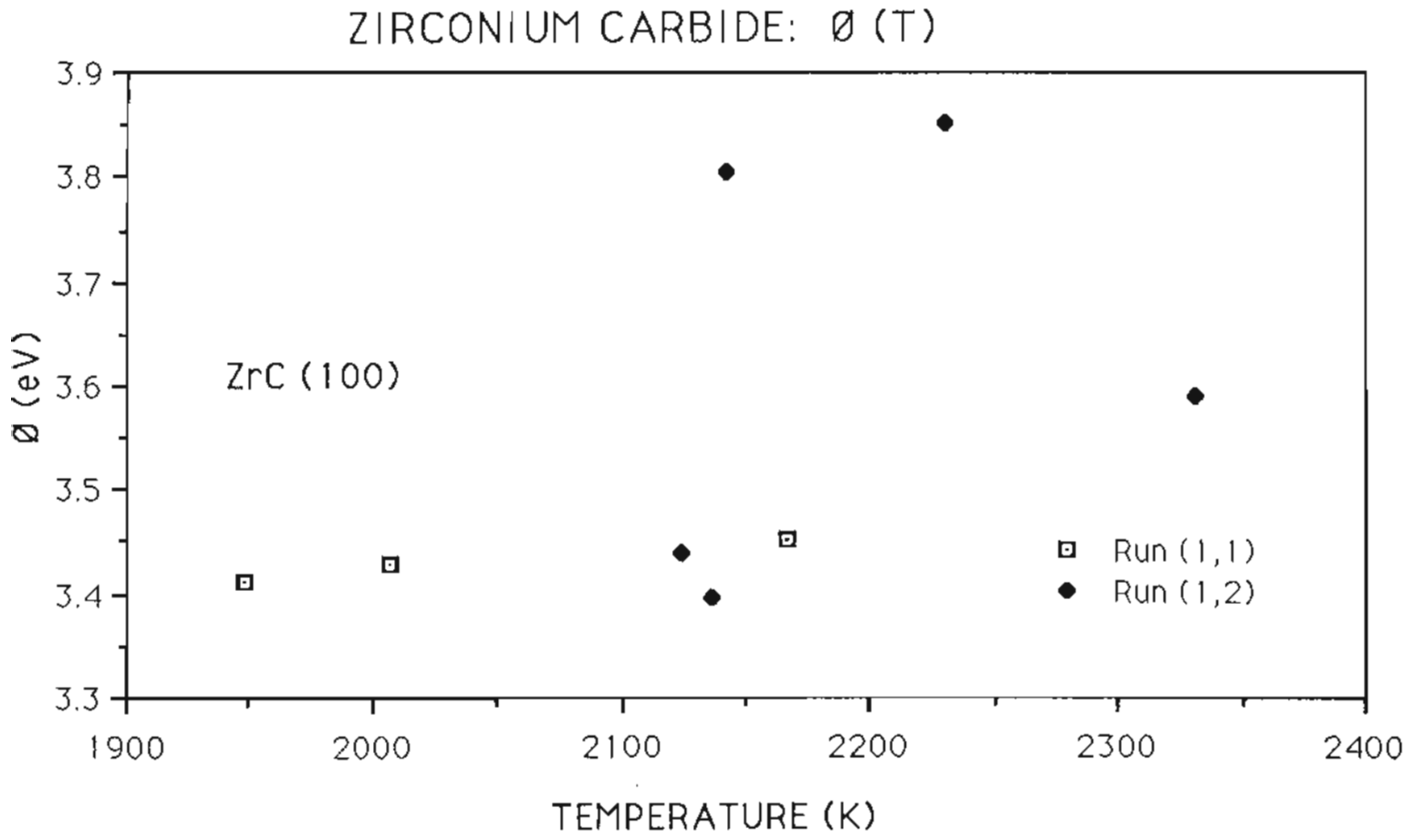

Fig. 64: Ø(T) for ZrC (100) sample 1.

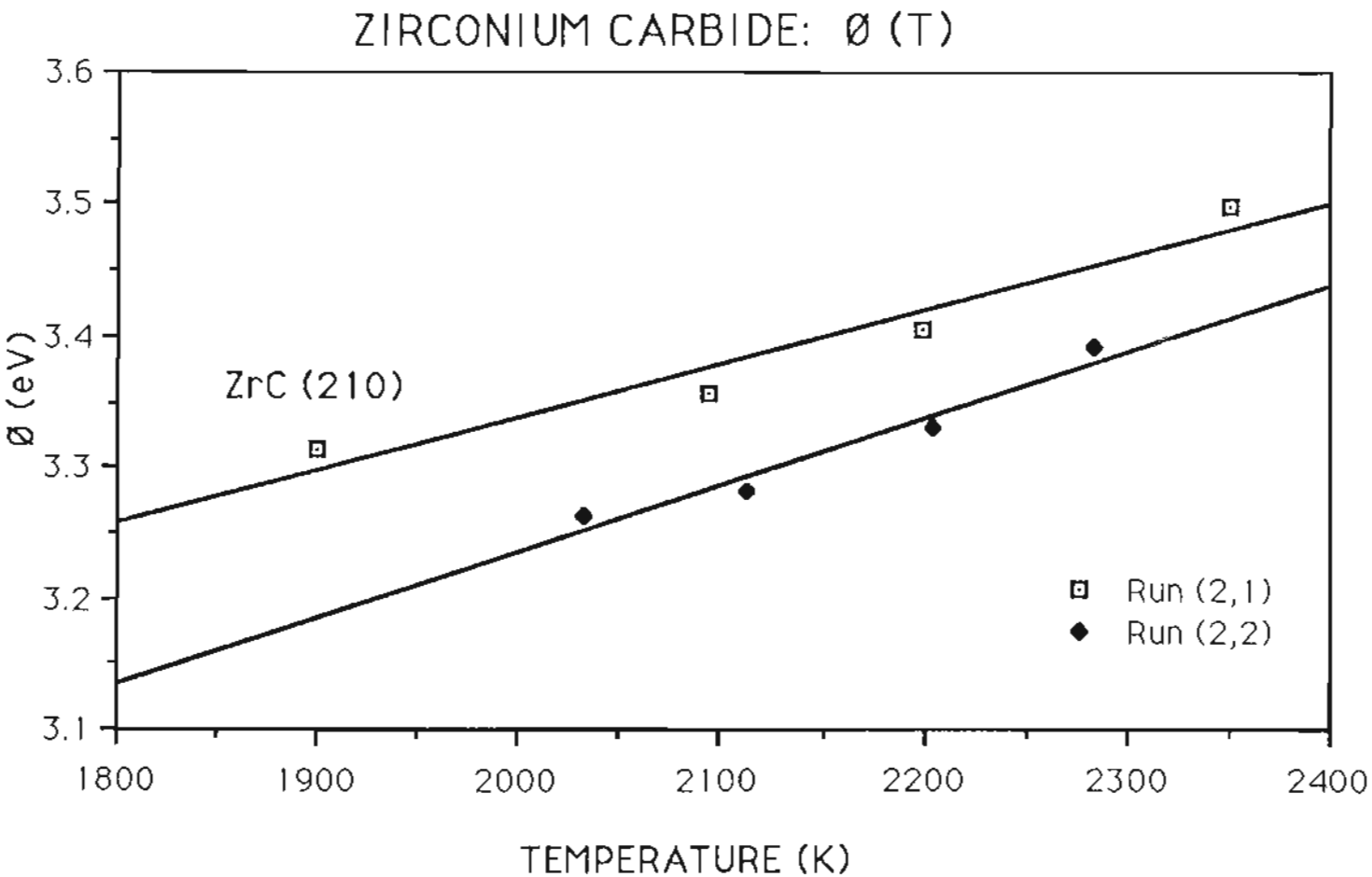

Fig. 65: Ø(T) for ZrC (210) sample 2.

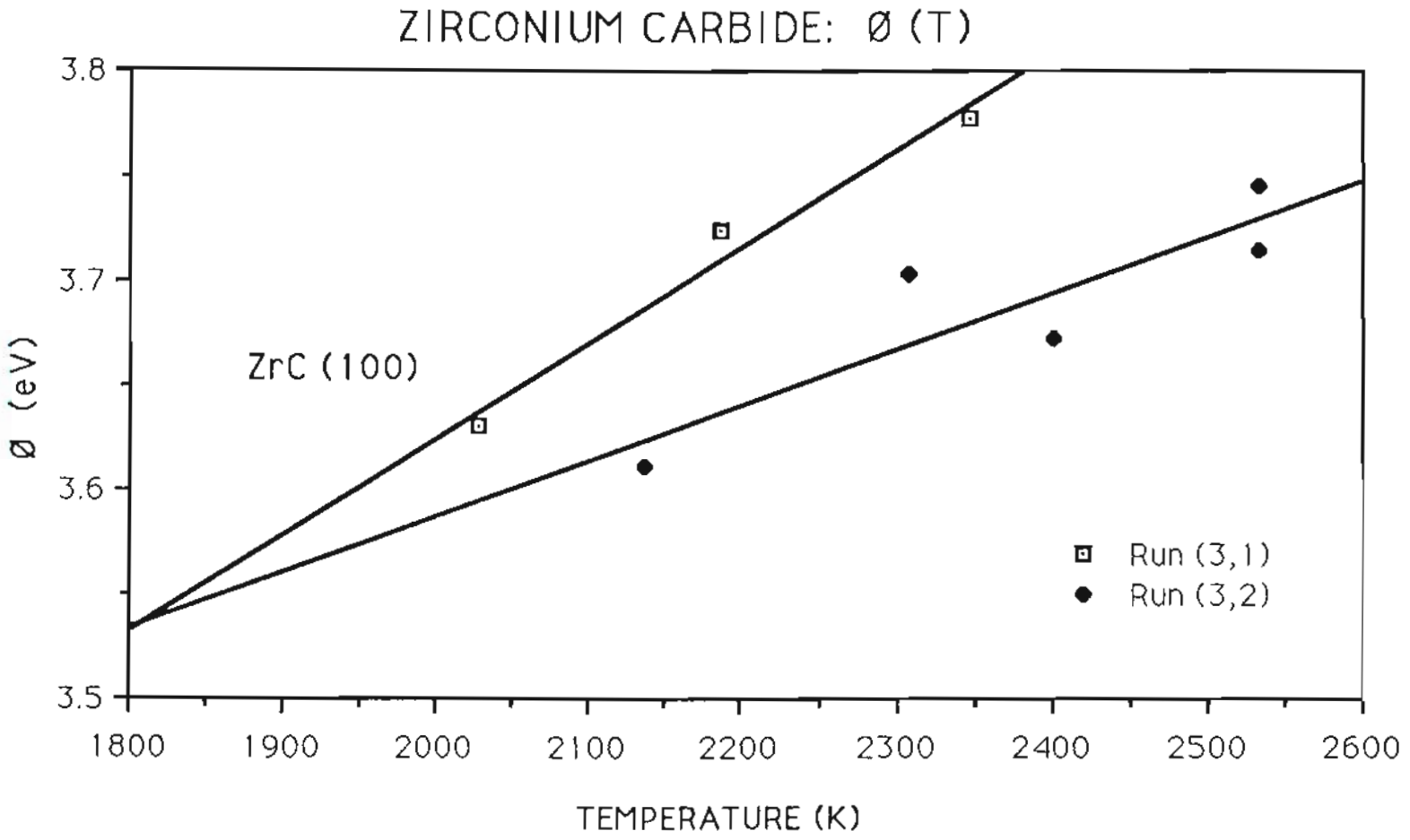

Fig. 66: Ø(T) for ZrC (100) sample 3.

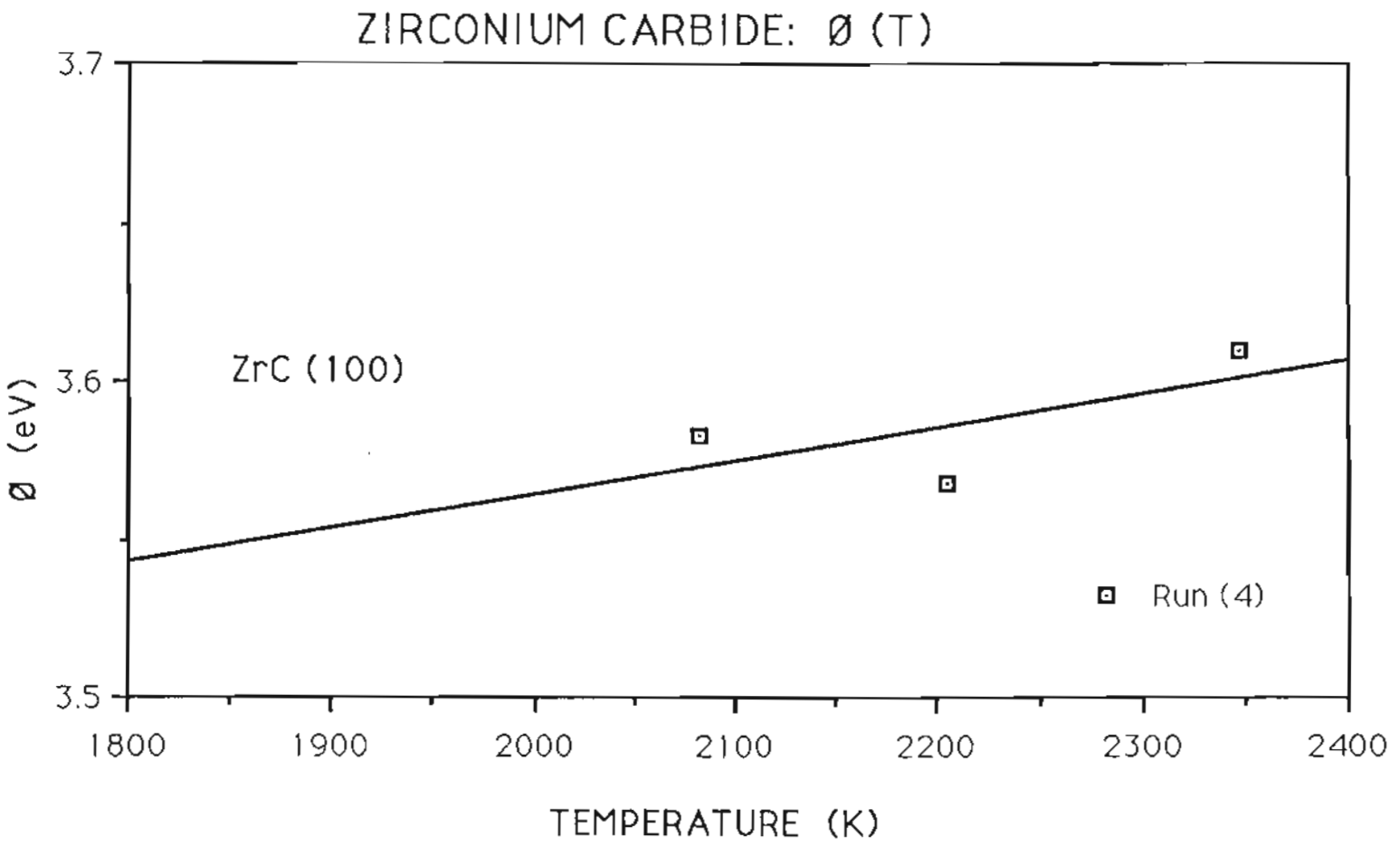

Fig. 67: Ø(T) for ZrC (100) sample 4.

iv) Analysis and Conclusions

The data clearly demonstrate the work function range for zirconium carbide at high temperatures. The values obtained for the (100) plane correspond well with those obtained under the previous room temperature study using FERP analysis. (See Section IV, the Conclusion and Summary, for a complete comparison of the data with predicted values.)

As mentioned earlier, the values for sample #1 may not be reliable. First, it is assumed that extended thermal cleaning is necessary to stabilize the surface and yield repeatable results. This was not realized for the first run of this sample. Second, the mounting necessitated by the crystal geometry could have introduced error. Since it was a cleaved plane off-axis, it is possible that edge effects could have been introduced. Sample #4 was also a cleaved (100) plane, off-axis. The $\phi(T)$ curve looks good and is plotted in Fig. 67. For the (311) sample two runs were tried, only one run is reported, and consists of but a single point. (see Table XVII)

Again, the data presented in Figs. 65 and 66 for the ZrC_{210} and ZrC_{100} samples respectively, represents the most reliable data. The geometry was good in that the emitting surface normal was on-axis, therefore minimizing edge effects. Also, two runs were taken for each sample.

There is a source of uncertainty worth noting. One wonders as to the slight differences in values from one run to the next. Its cause

may be the exposure to air between runs. If the surface stoichiometry has changed due to the elevated temperatures, oxygen or possibly other adsorbates collected between runs could effect the surface stoichiometry in some subtle manner. Some indication of this was noted in the previous FERP and AES study.

The between data run exposure to O_2 in air could have formed a zirconium oxy-carbide, which high temperatures failed to remove, thereby causing a lowering in ϕ_e. Evidence of this possibility was noted in the patterns of the thermionic projection microscope as well as the FERP/AES study.

It has been demonstrated that ZrC holds promise for use as high temperature thermionic cathodes, possibly for use in thermionic energy converters. A calculation of the current densities for $ZrC_{(100)}$ and $ZrC_{(210)}$ at 2500 K yields values greater than 10 and 50 A/cm^2 respectively for clean surfaces and greater than 25 and 85 A/cm^2 respectively for the suspected zirconium oxy-carbide surface.

In addition to finding the effective thermionic work functions, Richardson's plots were generated for samples 1,2,3 and 4, and are given in Fig. 68. Since the intercept of the curves represent the ln(A) where A is the "constant" 120 $A\text{-}cm^{-2}\text{-}K^{-2}$, another set of plots were made to show the intercept for each of the curves. (see Fig. 69) Since the slope of Richardson's plot is equal to $-e\phi$, these values are generated and listed in Fig. 69 in units of eV.

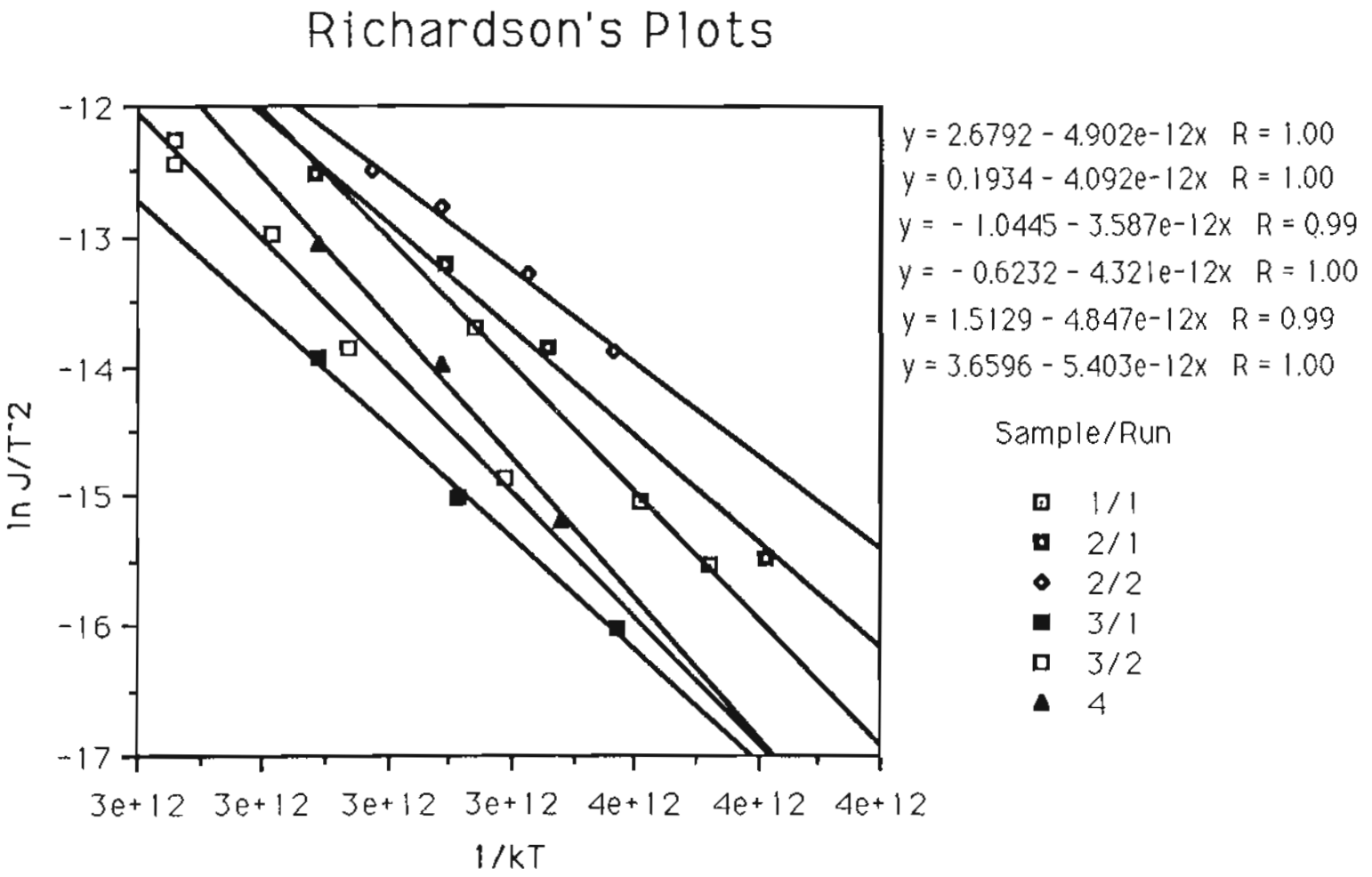

Fig. 68: Richardson's plots for ZrC samples 1 through 4.

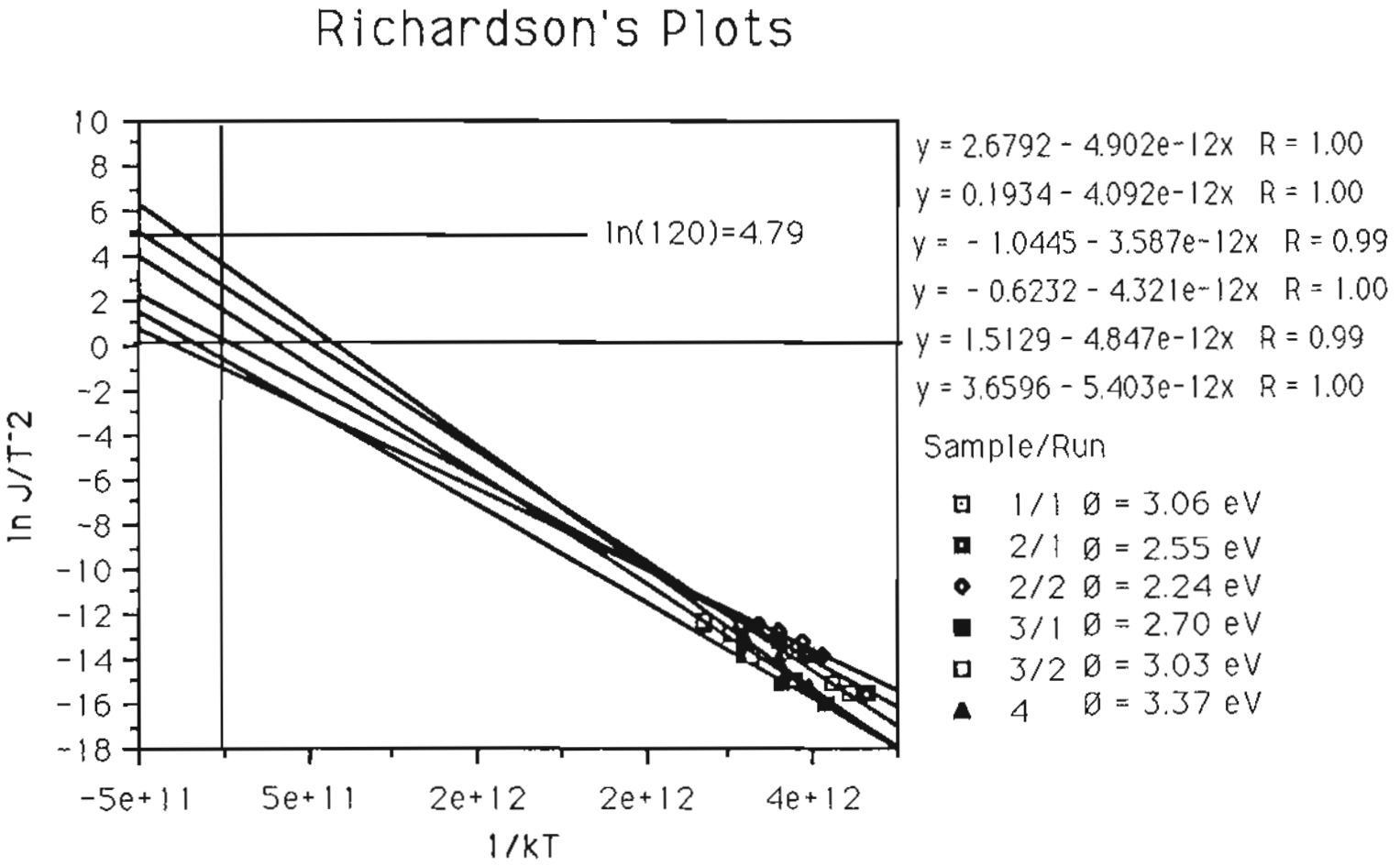

Fig. 69: Richardson's plots showing intercepts and Ø.

III. DISCUSSION

A. COMPARISION OF DATA

While more data are needed to clarify the surface of ZrC and the nature of any surface reconstruction, a few conclusions can be made.

1) A temperature of 1500 C seems adequate to remove most surface contaminants including N and O.

2) After thermal cleaning, which must alter the ZrC surface, and then exposure to air at atmospheric pressure the O remains on the surface even after heating to temperatures >1700 C. Only after argon ion sputtering does heating to 1500 C restore the surface to its previously "clean" condition. A possible explanation is that the oxygen has combined in the crystal lattice in vacated carbon sites.

3) It is interesting to note that a thermally cleaned ZrC surface, exposed to air at atmospheric pressure then shows ZrO bonding as is evident from the zirconium Auger peak structure. (see Fig. 70) This structure had been heretofore unseen. A substantiation of this can be found in a paper by Axelsson[22].

4) By subtracting 0.030 mV from the peak height, we can approximate the absolute work function as described in Part Two, Section IIB. The lowest FERP work function obtained for the $ZrC_{(100)}$ plane was 3.50 eV, this agrees well with the value of 3.4 eV reported in the Journal of Soviet Physics.[23] It also corresponds with the effective value of

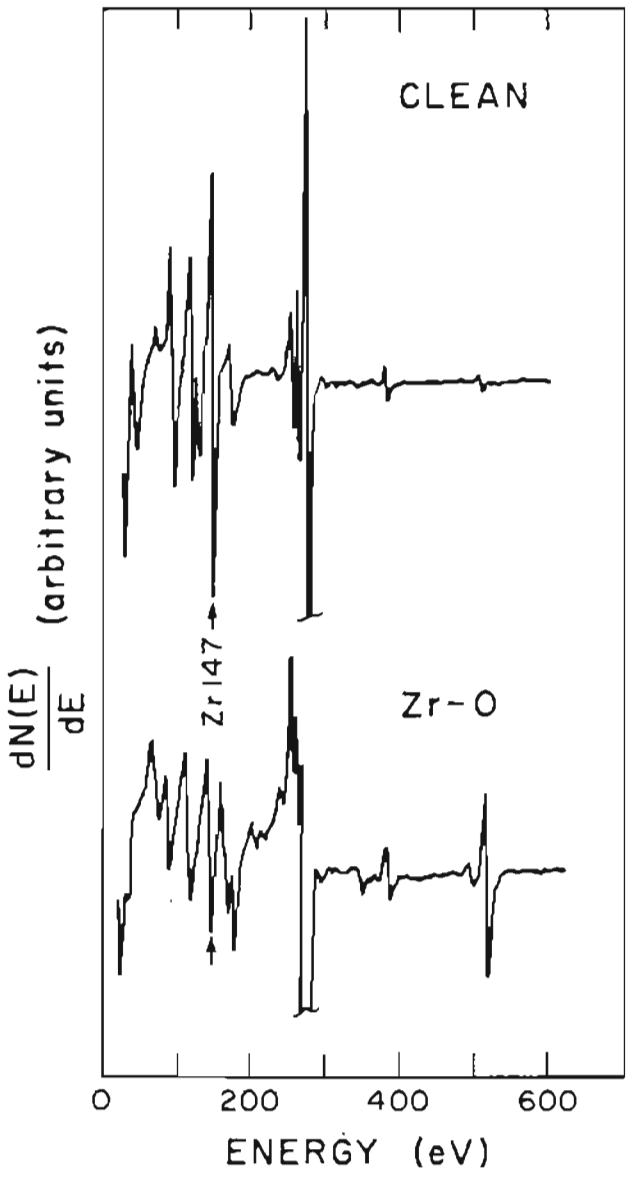

Fig. 70: Auger spectra of clean ZrC before exposure to oxygen (in air) and after oxygen. Note presence of ZrO peaks.

3.53 eV, at 1800 K, obtained via thermionic means. (see Part Two, Section IID) If the stoichiometric variations as well as temperature are factored in as per the model, the agreement is excellent. (See model predictions in the last section.)

5) The ratios of C/Zr were taken for two different values of zirconium (see Table XIII). The Zr(MNN) peaks are from low energy electrons and therefore come from only the first few surface layers. The Zr(LMM) peaks on the other hand represent higher energy electrons and therefore are representative of zirconium levels originating at a greater depth from the surface. The Zr(LMM) may then be thought to be more reflective of the bulk, while the Zr(MNN) is definitely reflective of the surface.

6) Since the bulk stoichiometry on those samples has been determined to be $ZrC_{0.91}$ the accuracy of the C/Zr ratios is confusing. Only the initial value obtained from the C(KLL)/Zr(LMM) ratio (see Table XIII) is even close to the value obtained through chemical analysis. Even if the bulk Auger C/Zr ratio obtained for the 3.50 eV work function were shifted to agree with the chemically analyzed stoichiometry, the surface Auger C/Zr ratio always appears higher.

7) In determining the C/Zr ratios and the percent of oxygen or nitrogen, the Auger sensitivities extrapolated as shown in Table XII were used. These values may lead to some of the uncertainties in the C/Zr ratios. There can be attenuation of the ejected Auger electron signal as they escape from the bulk or surface layers. The physical

nature or topography of the surface, matrix effects on escaping electrons, and chemical bonding at the surface can also lead to errors in the ratios and percents reported.

B. WORK FUNCTION THEORY

The work function of a material is a surface phenomenon, brought about by the vacuum/solid interface. It is formed by the raising of a potential barrier at the edge of the array of atoms comprising the material. If we consider a metallic crystalline material, such as ZrC, then the atomic array making up the bulk is uniform and orderly.

To determine the energy levels of the electrons, we need to solve Schroedinger's equation given a potential inside the solid which assumes the periodicity of the crystal lattice. The repeating potential is truncated at the metal's surface, as is depicted in Fig. 71, and leads to the potential barrier seen by the conduction band electrons which approach the surface from the inside. The height of this barrier from the top of the conduction band, the highest energy level of electrons existing in the metal at a temperature of zero degrees Kelvin, is known as the work function.

This electronic work function is thus directly influenced by the properties of the atoms and the atomic lattice making up the bulk of the solid. A second factor, the surface potential χ, is sensitive to the surface only and reflects the variation in structure and composition which can be generated at surfaces.

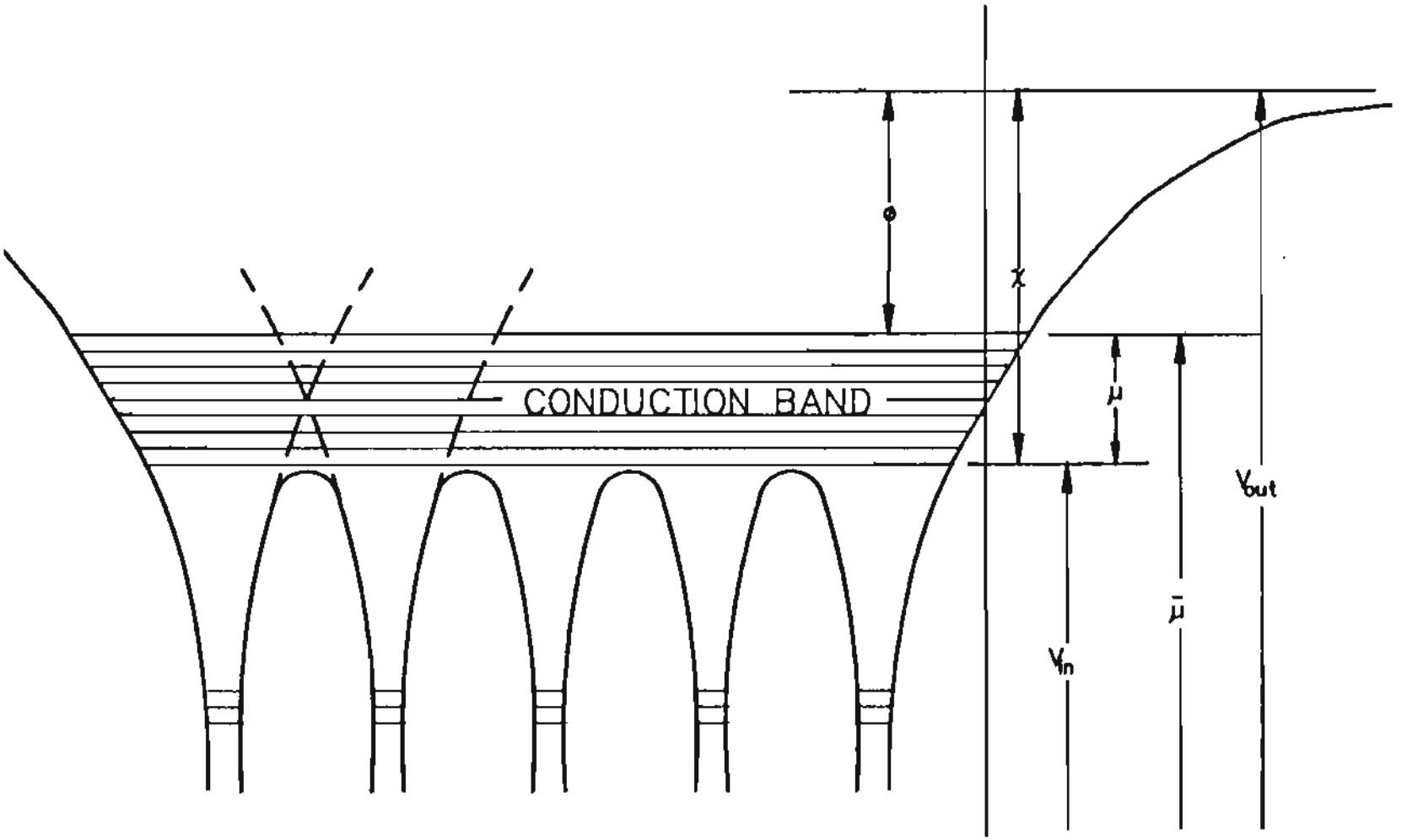

Fig. 71: Schematic energy diagram of metal surface.

i) Historical Overview

"genius is one percent inspiration and ninety-nine percent perspiration." T. Edison

It was T. A. Edison in 1884 who first observed the effect of thermally emitted electrons while experimenting with an independent electrode near a heated carbon filament in his electric lamp.[24] The mechanism of this "Edison effect" was found by J.J. Thompson in 1889 to be the emission of electrons.

In 1901, O.W. Richardson first derived an equation relating the current density of these thermally emitted electrons to the temperature of the emitting surface. However, the present form of "Richardson's equation" was not brought forward until much later. Refinements on Richardson's initial attempts based on P. Drude's free-electron theory were made in 1912, again by Richardson, in 1918 by M. von Laue, in 1923 by Dushmann using quantum mechanical analysis, and finally corrected in 1929 by R.H. Fowler to the present form.

During the 1930's, E. Wigner, F. Seitz, and J. Bardeen developed what was to be the foundation of modern theories of work function. Their treatment is based on a self-consistent field solution for electrons in a metal and includes the exchange and correlation effects in addition to allowing for surface-dipole calculations.

Through the 1930's and 1940's various calculations and work function

predictions were made based on modifications to the free-electron model of Fermi-Thomas. Of particular note is the work done in 1941 by R. Smoluchowski, who calculated the variations in work function for different crystal faces of the same material.

ii) Current Theories

The electronic work function has been described[25] as the change in the Helmholtz free energy of a system when an electron is removed from the system at constant temperature and volume. The Helmholtz potential, F, is defined as F = U - TS, with U the energy, T the temperature and S the entropy.

If we assume the surface under consideration to be "clean", with no adsorbates present, then the change in Helmholtz free energy is by definition the electrochemical potential μ,

$$\mu = (\partial F/\partial n)_{T,v} \qquad (39)$$

Requiring that $(\partial S/\partial n)_{T,v} \rightarrow 0$ as $T \rightarrow 0$, implies that for a metal of constant volume the electrochemical potential is the work done in bringing an electron from infinity and adding it isothermally to a metal.

From Fig. 71, we can see that the work function can be written as

$$\phi = V_{out} - \bar{\mu}/e \qquad (40)$$

The chemical potential, μ is defined as

$$\mu = \bar{\mu} - eV_{in} \quad (eV). \qquad (41)$$

Letting χ, the surface potential, be the difference in the average potential seen by an electron outside the surface and inside the metal lattice ($\chi = V_{out} - V_{in}$), we then arrive at a working definition of electronic work function as

$$\phi = \chi - \mu/e \quad (eV) \qquad (42)$$

The chemical potential term, μ/e, is a bulk property of the material being studied and is independent of surface effects. The surface potential, χ, is primarily dependent on the surface in question, and varies both with surface adsorbates and with crystallographic direction.

In principle, μ can be obtained from the Fermi distribution function. If the bottom of the conduction band is taken as the zero of energy, then the value of μ is the energy difference between an electron at the Fermi level and an electron in the lowest energy level of the conduction band. (see Fig. 71)

The surface potential term has a factor which is due to the

asymmetrical electron distribution arising from truncation by the surface of the regular lattice array found in the bulk. A surface dipole is set up by this charge asymmetry. This dipole effect, D, varies with the different atomic spacings found for surface atoms of different crystallographic planes, and is given by

$$D = \pm 4\pi M. \tag{43}$$

The double layer of charge gives rise to the moment, M, perpendicular to the surface. The sign of the above expression varies with the sign of the outer-most charge. By definition, we assign a positive value to the case where a positive charge is outermost.

This dipole surface layer is affected not only by the crystallographic direction but by adsorbates on the surface as well. It has been shown[26] that the change in work function, $\Delta\phi$, associated with surface adsorption can be related to σ, the number of dipoles per unit area,

$$\Delta\phi = \Delta\chi = \pm 4\pi\sigma\mu_e. \tag{44}$$

Here μ_e is the effective dipole moment, $\mu_e = qd$, the product of the charge, q, of the adsorbed molecule and the separation, d, of the two charged layers.

The work function change on adsorption can then be written as a function of the fractional coverage, θ, as

$$\Delta\phi = \pm 4\pi\theta\sigma_o\mu_e \qquad (45)$$

where $\theta = \sigma/\sigma_o$ (σ_o is the number of adsorption sites per unit area).

At this point it seems that the equations of greatest utility are the latter ones, those giving a value for the change in work function for a given surface adsorbate. They have been used extensively by Swanson, et al[27] and others to predict and verify experimental work function changes with adsorbates on various refractory metal surfaces. At present, our ability to accurately predict the electronic work function from first principles for a particular metal and a given crystallographic direction is poor. Various models have been devised to approximate a metal: the jellium model, the Wigner-Seitz cell model, etc. These models require gross approximations to yield results. The problem of solving Schroedinger's equation with the intricate periodic potentials found in the bulk, and the complexity in dealing with the crystallographic surface makes solutions virtually impossible without simplifying methods. The added problem involved with a binary compound of varying stoichiometry, such as ZrC, requires a different approach.

iii) Transition Metal Carbide Work Function Theory

There is an entirely different approach open in the search for a work function theory with greater practical utility. There are several

empirical or semi-empirical approaches that have proved fruitful, many of which involve the concept of electronegativity of the element.

In 1956, W. Gordy and W.J.O. Thomas noted the empirical relationship of electronegativity to work function.[28] The simple linear relationship is

$$\phi = 2.27x + 0.34 \qquad (46)$$

where ϕ is the work function in electron volts and χ is the electronegativity in Pauling units. While showing good agreement for many elements, it could not predict single crystal plane differences.

Electronegativity is a property of an atom which has been described by Pauling[29] as the "power of an atom in a molecule to attract electrons to itself." The key concept is that electronegativity can be associated with an atom in a molecule rather than with an isolated atom. In general, the electronegativity of an element is different depending on whether it is isolated or bound in a molecule or other structure. It is precisely this view that lends itself to using the concept of electronegativity for the computation of the electronic work function.

According to Fig. 71, the emission would be depicted as coming from a sea of electrons, whose top is described as the Fermi level. However, we could view electron emission from a more physically descriptive viewpoint. Considering the atomic lattice found in crystalline materials, we can view electron emission as originating from a valence orbital of a surface atom. A valence electron is removed from a surface

atom, and its energy is determined by considering electron interactions with all of its neighboring atoms. The energy of this valence electron would differ from that of an electron in an isolated atom. During the electron emission it is assumed that the energy of the surface atom would not change. This assumption is valid if the crystalline structure under consideration is metallic where the valence (conduction) electrons are free to move and replace electrons removed in the emission process.

In this view, the electronic work function is described as the work required to remove a valence electron from a surface atom without altering the energy state of the atom. Work function calculations are therefore simplified to calculations of the energy per valence electron of a surface atom. This can be done for binary compounds through a modification of the steps outlined first by Steiner and Gyftopoulos in 1967.[30] The method they used dealt with extending the concept of electronegativity, or neutral electronegativity, which is developed next.

In 1963, Hinze, Whitehead and Jaffe[31] defined the quantity x(q) as the orbital electronegativity of an atom. It is given by

$$x(q) = (I + A)/2 + (I - A)q/e \qquad (47)$$

and represents the energy per valence electron with q being the charge population of the orbital. I and A are the ionization potential and electron affinity respectively. Their analysis made possible the

introduction of fractional charge, q, into modeling of the electronegativity and later the work function. It follows that the desired neutral electronegativity, x(0), would be just the average of I and A.

Since the quantities I and A are not measurable, especially for a surface atom bound in a crystalline structure, an alternate method is needed. In 1946, W. Gordy[32] published a paper with a new method of defining the electronegativity of a neutral atom in a molecule. His reasoning led to the potential $(Z_{eff})e/r$, where $(Z_{eff})e$ is the effective nuclear charge of the atom. The effective charge then would act over the distance from its nucleus equal to its single bond covalent radius, r.

Gordy made the assumption that every electron other than the valence electrons screens completely a nuclear charge and that the screening constant of one valence electron for another is one half, so

$$Z_{eff} = v - 0.5(v-1) = 0.5(v+1). \qquad (48)$$

Here, v is the number of electrons in the valence shells.

Substitution led Gordy to tentatively define electronegativity as

$$x = (Z_{eff})e/r = k(v + 1)/r \qquad (49)$$

where k = 0.5e. However, plotting (v+1)/r versus x for various elements

revealed a linear plot with different constants of proportionality,

$$x(0) = 0.31(v + 1)/r + 0.50 \qquad (50)$$

It was from this equation that Steiner and Gyftopoulos started. Their basic assumption was that "the neutral electronegativity may be interpreted as the work required to remove a valence electron from an atom without altering the energy state of the atom."[30] Since the electron comes from the metal's surface, it follows that the bare work function, ϕ, equals the neutral electronegativity of the surface atom. They therefor wrote,

$$\phi = 0.98(v_s + 1)/r + 1.57 \quad (eV), \qquad (51)$$

where v_s is the number of electrons per surface atom which participate in bonding. The effective radius, r, was assumed equal to the atomic radius as given by Slater,[33] and the constants are changed to give ϕ in eV.

To determine the surface valence, v_s, we first need to consider the bulk valence v. For elemental metals, Steiner and Gyftopoulos first used Pauling's[29] empirical relation

$$D_2 - D_1 = 0.26\ln(n_1/n_2), \qquad (52)$$

where the fractional bond numbers n_1 and n_2 are associated with interatomic spacings D_1 and D_2 respectively. Then, since the metallic valence, v, is defined as the number of electrons per atom which participate in bonding in the bulk of the metal, the fractional bond numbers must total the bulk valence when the appropriate nearest and next-nearest neighbors are considered. That is, if interactions further than next-nearest neighbors are assumed small, then

$$v = N_1 n_1 + N_2 n_2, \tag{53}$$

where N_1 and N_2 are the number of nearest and next-nearest neighbors respectively.

Since v, N_1, N_2, D_1, and D_2 are known, n_1 and n_2 can be found using Eqs. (52) and (53). Finally, crystallography determines the number of nearest and next-nearest neighbors for surface atoms (N_{s1} and N_{s2} respectively), hence the surface valence is given as

$$v_s = n_1 N_{s1} + n_2 N_{s2}. \tag{54}$$

This is assuming that the fractional bond numbers of the surface atoms are identical to those of bulk atoms.

In this manner the bare metal work functions as a function of crystallographic direction can be generated. This method has proved useful and has been used by Swanson, et al.[34] to closely predict the

work functions of some binary compounds, such as LaB_6. However, for the carbides some additional modifications are suggested and are outlined in the following section.

iv) Predictions

So far we have followed the historical development of semi-empirical work function theory. The material's electronegativity is crucial in this development. We now have a satisfactory equation which takes into account surface crystallography. However, stoichiometric variations of binary compounds in general are not dealt with using this method as it now stands.

Yamamoto, et al.[35] did try a method of work function prediction, using Gordy's equations. While their predictions broadly fit with experimental data, no provision is made to account for variations with crystal direction.

Several assumptions are needed to yield a viable model for work function predictions of transition metal carbides. First, the assumption is made that the Steiner-Gyftopoulos analysis is applied with respect to the valence orbitals of the surface zirconium or transition metal atoms only. This assumption is not unreasonable due to the excess electrons over filled shells and due to their larger atomic radius, clearly depicted when viewing models of various surface planes. (see Tables XVIII and XIX and Fig. 1)

TABLE XVIII: Electron shell occupations for carbon and the transition metals.

		ELEMENTAL ELECTRON CONFIGURATION																							
		K		L			M			N				O			P							
		s		s	p		s	p	d	s	p	d	f	s	p	d	s							
Carbon	6	2		2	2																			
Titanium	22	argon core								2		2												
Vanadium	23	argon core								3		2												
Zirconium	40	krypton core								2	-	2												
Niobium	41	krypton core								4	-	1												
Hafnium	72	xenon core															2			2				
Tantalum	73	xenon core															3			2				

TABLE XIX: Atomic radii in Angstroms of pertinent elements. (from Slater[33])

Element	radius (Å)	Element	radius (Å)
C	0.70	Nb	1.45
Ti	1.40	Hf	1.55
V	1.35	Ta	1.45
Zr	1.55		

Second, it is assumed that less than 1% of the charge is involved in bonding to atoms further than next nearest neighbor.

The third assumption is that the bulk valence v of zirconium is equal to three. This assumption is made without a definitive theoretical calculation, from band structure for instance, but a rough empirical calculation can be made based on the concept introduced first in 1957 by J.K. Wilmshurst.[36] He generated an effective valence number for a component A in a radical AB, where the effective valence of A consists of three parts: nonbonded electrons, bonded electrons, and resonance electrons. Depending on the parameters chosen in Wilmshurst's equation, a fractional effective valence of approximately three is obtained. The primary rationale, however, for using a bulk valence of three for a zirconium atom bound in a ZrC crystal lattice was empirical, as discussed below.

The radius r used in this model was derived from consideration of the lattice parameter of ZrC. Zirconium carbide has a cubic (NaCl type) crystal structure. (see Fig. 1) The lattice parameter varies very slightly with stoichiometry, but insignificantly over the range of stoichiometries from C/Zr = 0.7 to 1.0. (see Fig. 2) The value of the lattice parameter was taken to be 4.70 Å.[1] This distance is that of a zirconium plus a carbon diameter, as is depicted in Fig. 72. Based on this information as well as that of Slater[33] and Coulson[37] the atomic radius of zirconium in the ZrC lattice is taken to be 1.64 Å.

The last factor to account for is that of stoichiometry. Zirconium

carbide as well as other transition metal carbides can exist over a wide range of stoichiometries, by the removal of carbon atoms from the carbon sublattice.[1] Since substoichiometric ZrC was used in this research, the effect of varying the C/Zr ratio needs to be integrated into the work function model.

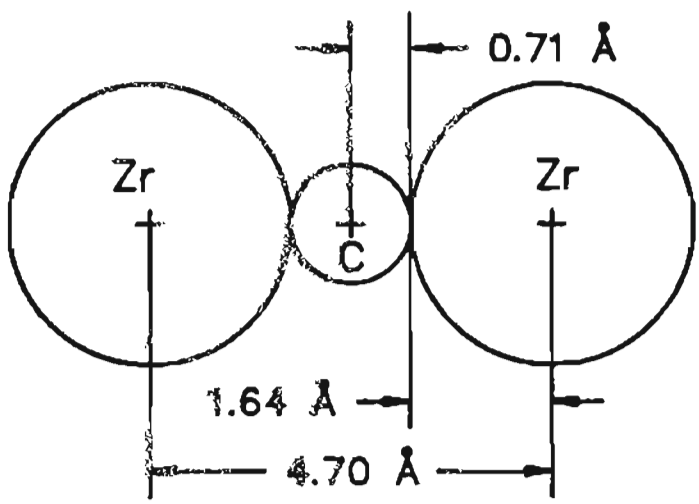

Fig. 72: Spacing of zirconium and carbon sites in ZrC lattice of typical stoichiometry.

Equation (54) relates the number of nearest and next-nearest surface atoms to a zirconium atom under consideration. Since every nearest atom is of the opposite species (carbon) and every next-nearest atom is of the identical species, the C/Zr ratio is inserted as a factor in the first term of equation (54), giving us

$$v_s = (C/Zr)n_1N_{s1} + n_2N_{s2}. \qquad (55)$$

Table XX gives the values for the number of nearest and next-nearest neighbors for specific surfaces of zirconium carbide.

TABLE XX: LIGANDS FOR SURFACE ATOMS

# of neighbors on surface	Orientation (100)	(110)	(111)	(210)	(211)	(310)	(311)
nearest							
N_{s1}	5	4	3 (6)	4	3 (6)	4 (5)	3 (6)
next-nearest							
N_{s2}	8	7	9 (10)	6	7 (11)	6 (8)	7 (8)

Values for N_{s1} and N_{s2} for use in Eq. (55) for zirconium carbide. Numbers in ( ) are for cases where a different count is obtained when carbon is terminating the surface.

There remains one last problem, that of determining the proper surface configuration, where there is a choice. Without the availability of definitive surface studies, an empirical approach was used. Thermionic emission patterns were studied from a hemispherical,

(100) oriented crystal. The patterns obtained with the TPM, in section IID, gave an indication as to the relative work functions. Each of the options in Table XX was evaluated using the model. Comparing these with the ordering demonstrated by the thermionic emission data yielded a rational for selection of proper surface counts. Based on this method the odd planes; (111), (211) and (311) appeared to demonstrate the carbon atoms to be outermost. Interestingly, though LaB_6 has a different cubic lattice, the (111) face was verified as behaving in a similar manner.[34]

Using 2.35 Å for the nearest neighbor spacing and 3.32 Å for the diagonal, next-nearest neighbor spacing (see Fig. 72), Eqs. (52) and (53) are simultaneously solved. This yields fractional bond numbers of 0.4774 and 0.0113 for n_{s1} and n_{s2} respectively. These combine in Eq. (55) with the selected count from Table XX to give the surface valences. The predicted work function values, listed in Table XXIa, are then obtained using Eq. (55). The C/Zr ratio used was 0.896, which is a typical value for the stoichiometry of the samples used experimentally.

Varying the stoichiometry causes the work function to vary. (see Table XXIb) However, at the congruently vaporizing composition, the work function may be at its minimum. Any further stoichiometric lowering of the bulk, would at first tend to shift the emitting surface to the congruent value. Finally, if the stoichiometry changes far enough, the crystal structure reverts to that of zirconium, which has a HCP type lattice.

TABLE XXIa: Predicted Work Function Values for Surfaces of $ZrC_{0.896}$

Orientation	Work Function (eV)
(100)	3.50
(110)	3.24
(111)*	3.77
(210)	3.23
(211)*	3.78
(310)	3.23
(311)*	3.76

* carbon atom assumed outermost

TABLE XXIb: Predicted Values Over a Range of Stoichiometries for ZrC_x

Orientation	C/Zr = 1.000	23/24	11/12	5/6
	work functions (eV)			
(100)	3.65	3.59	3.53	3.41
(110)	3.36	3.31	3.26	3.17
(111)*	3.95	3.88	3.80	3.66
(210)	3.35	3.30	3.25	3.16
(211)*	3.95	3.88	3.81	3.67
(310)	3.35	3.30	3.25	3.16
(311)*	3.93	3.86	3.79	3.65

* carbon atom assumed outermost

Using Eq. (51) the work function for pure zirconium can be predicted;[30] $Zr_{(0001)}$ = 4.04 eV and $Zr_{(0101)}$ = 3.89 eV. With these and the values in Table XXIb, we can sketch a cursory relation between the work function and stoichiometry. With the assumptions that 1) the congruent vaporization point is $ZrC_{0.86}$, and 2) the (100) plane of zirconium carbide would go to the (0001) plane of zirconium, the work function dependence is depicted in Fig. 73. The exact behavior in the dashed portion has not been predicted, but it would vary as pure zirconium with added carbon as an impurity over the initial portion of the dashed curve.

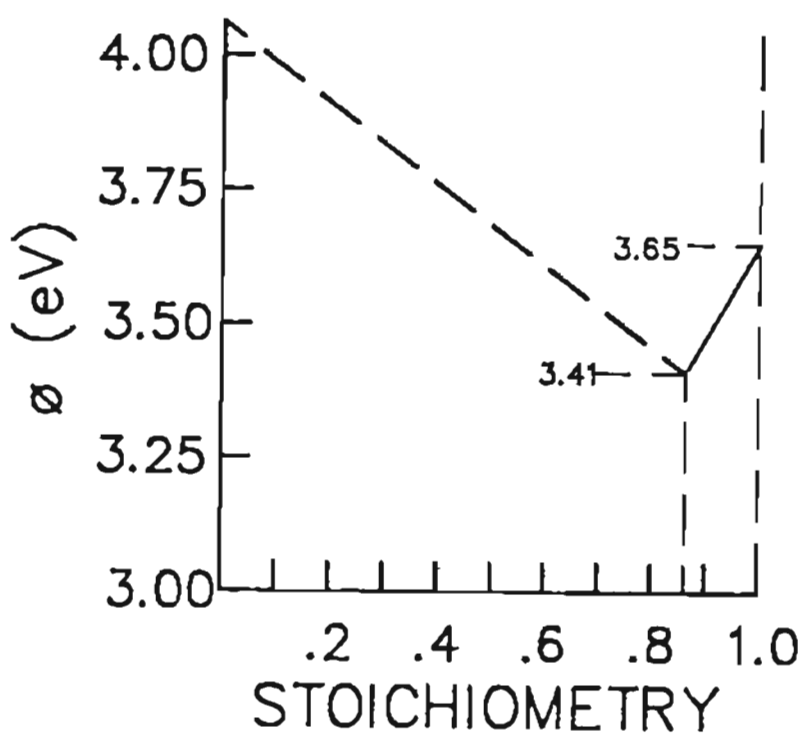

Fig. 73: Form of work function varience with stoichiometry for ZrC.

This model was extended to predict the work functions for other transition metal carbides. The parameters used in these calculations are given in Table XXII. The values of the work functions calculated using Eqs. (51) and (55) and Tables XX and XXII are compiled in Table XXIII.

TABLE XXII: Parameters Used in
Predicting the Work Function of Transition Metal Carbides

	Lattice Parameter[1] (Å)	Transition Metal radius (Å)	Bulk valence used
TiC	4.328	1.45	3
ZrC	4.700	1.64	3
NbC	4.468	1.514	4
HfC	4.640	1.60	3
TaC	4.454	1.507	4

TABLE XXIII: Work Function Predictions

for Various Transition Metal Carbides

material	plane (100)	(110)	(111)	(210)	(211)	(310)	(311)
x = 1.0			work function (eV)				
TiC_x	3.92	3.59	4.25	3.58	4.26	3.58	4.23
ZrC_x	3.65	3.36	3.95	3.35	3.95	3.35	3.93
NbC_x	4.35	3.93	4.78	3.92	4.80	3.92	4.76
HfC_x	3.70	3.40	4.01	3.39	4.01	3.39	3.99
TaC_x	4.36	3.94	4.80	3.93	4.81	3.93	4.77
x = 0.958			work function (eV)				
TiC_x	3.85	3.53	4.17	3.52	4.18	3.52	4.15
ZrC_x	3.59	3.31	3.88	3.30	3.88	3.30	3.86
NbC_x	4.27	3.86	4.68	3.85	4.69	3.85	4.66
HfC_x	3.64	3.35	3.93	3.34	3.94	3.34	3.92
TaC_x	4.28	3.87	4.70	3.86	4.71	3.86	4.67

material	(100)	(110)	(111)	(210)	(211)	(310)	(311)
x = 0.9166			work function (eV)				
TiC_x	3.78	3.48	4.09	3.47	4.10	3.47	4.07
ZrC_x	3.53	3.26	3.80	3.25	3.81	3.25	3.79
NbC_x	4.18	3.80	4.58	3.78	4.59	3.78	4.56
HfC_x	3.58	3.30	3.86	3.30	3.87	3.30	3.85
TaC_x	4.19	3.81	4.59	3.79	4.60	3.79	4.57
x = 0.896			work function (eV)				
TiC_x	3.75	3.46	4.06	3.45	4.07	3.45	4.03
ZrC_x	3.50	3.24	3.77	3.23	3.78	3.23	3.76
NbC_x	4.14	3.76	4.53	3.75	4.54	3.75	4.51
HfC_x	3.55	3.28	3.82	3.27	3.83	3.27	3.81
TaC_x	4.15	3.77	4.54	3.76	4.55	3.76	4.52
x = 0.833			work function (eV)				
TiC_x	3.65	3.38	3.94	3.37	3.95	3.37	3.92
ZrC_x	3.41	3.17	3.66	3.16	3.67	3.16	3.65
NbC_x	4.01	3.66	4.38	3.65	4.39	3.65	4.35
HfC_x	3.46	3.21	3.71	3.20	3.72	3.20	3.70
TaC_x	4.02	3.67	4.39	3.66	4.40	3.66	4.36

IV. CONCLUSIONS AND SUMMARY

Experimental ϕ and Correlation with Theory

To view the utility of the electronic work function model developed in the first section, a compilation of the values obtained experimentally are listed in Table XXIX. In addition to listing values obtained in this research effort, other single crystal value for work functions are listed and referenced, including values for other transition metal carbides as well. It should be noted that the predicted values are a function of stoichiometry, so in each case the bulk stoichiometry given in the reference is the value used as a factor in the model.

TABLE XXIX: Experimental Work Functions for Transition Metal Carbides and Comparison with Predicted Values

Material	Model ϕ (eV)	Present Research ϕ (eV)	Method
$ZrC_{0.896}$ (100)	3.50	3.53	Thermionic @ 1800 K
$ZrC_{0.896}$ (210)	3.23	3.25	"
$ZrC_{0.896}$ (311)	3.76	3.60	"
$ZrC_{0.91}$ (100)	3.53	3.50	FERP
$TiC_{0.935}$ (100)	3.83	4.12	"

Material		Model ϕ (eV)	Other's Research ϕ (eV)/Method	
$ZrC_{0.84}$	(100)	3.41	3.40[23]	Thermionic @ 1800 K
$NbC_{0.86}$	(100)	4.07	4.0[23]	"
$NbC_{0.86}$	(210)	3.70	4.1[23]	"
$NbC_{0.86}$	(100)	4.07	3.98[38]	"
$NbC_{0.81}$	(100)	3.97	3.92[38]	"
$NbC_{0.88}$	(111)	4.51	4.33[38]	"
$NbC_{0.88}$	(110)	3.76	4.05[38]	"
$TiC_{0.94}$	(100)	3.81	3.8[39]	Photoelectron
$TiC_{0.94}$	(111)	4.14	4.7[39]	UPS
$TiC_{0.94}$	(110)	3.52	3.7[39]	"

The results presented in Table XXIX show good agreement with the model. The divergent values obtained in this present study on $ZrC_{(311)}$ thermionically measured and the $TiC_{(100)}$ measured via the FERP method can be reconciled with the models values. Referring to Table XVI shows us that the ZrC sample was ~7 degrees off from an actual (311) orientation. This could easily account for the discrepency. The (100) oriented TiC was only briefly examined with only a moderate thermal cleaning. The ability to properly heat this particular sample was precluded by the experimental configuration. Future study is needed to

ascertain a dependable value.

The agreement with the other experimental values found is in most cases good.

Through this modest effort the utility of the transition metal carbides in general and ZrC in specific is enhanced. Their use as cathodes in thermionic energy converters and possible use as dependable field emitters has been demonstrated. In addition, a relatively simple and reliable method has been developed to consistently produce single crystal samples of the transition metal carbides for use in future research.

REFERENCES

1 E.K. Storms, The Refractory Carbides, Academic Press, 1967.

2 R.C. Weast, ed., CRC Handbook of Chemistry and Physics, CRC Press, 1979.

3 D.W. Lee and J.S. Haggarty, J. Am. Ceram. Soc. 52, 641 (1969).

4 S. Otani, T. Tanaka and A. Hara, J. Crystal Growth 51, 164 (1981).

5 J.D. Verhoaven, E.D. Gibson, M.A. Noack and R.J. Conzemius, J. Crystal Growth, 36, 115 (1976).

6 R.B. Bird, W.E. Stewart and E.N. Lightfoot, Transport Phenomena Wiley, New York, 1960.

7 TiC obtained from N. McMillan, Penn. State, PA; ZrC and TaC obtained from C. Finch, Oak Ridge Labs, Oak Ridge, TN.

8 Crystalite Corp., 13449 Beach Ave., Marina del Ray, CA 90291.

9 L.W. Swanson and L.C. Crouser, Surf. Sci., 23, 1-29 (1970).

10 R.W. Strayer, W. Mackie and L.W. Swanson, "Work Function Measurements by the Field Emission Retarding Potential Method," Surf. Sci., 34, 225 (1973).

11 R.L. Park,"Inner-shell spectroscopy", Physics Today, April, (1975)

12 L.A. Harris, J. Appl. Phys., 39, 1419 (1968).

13 AES Handbook, Physical Electronics Div., Perkin-Elmer Corp. 6509 Flying Cloud Drive, Eden Prairie, MN 55344.

14 R.H. Fowler and L.W. Nordheim, Proc. Royal Society (London) A 119, 173 (1928).

15 W.P. Dyke and W.W. Dolan, in L. Marton, ed., Advances in Electronics and Electron Physics, 8 (Academic Press, N.Y., p. 89, 1956.

16 R. Gomer, Field Emission and Field Ionization, Harvard Univ. Press, Cambridge, MA 1961.

17 J.A. Kubby and B.M. Siegel, Nuclear Inst. & Methods in Physics Research, B (1986).

18 A.P. Janssen and J.P. Jones, J. Phys. D: Applied Physics, Vol. 4, (1971).

19 J.M. Walls, R.M. Boothby and H.N. Southworth, Surf. Sci., 61, 419-434 (1976).

20 R. Shimizu and H. Onoda, "Direct observation of thermionic emission pattern of hemispherical single-crystal LaB_6," J. Appl. Phys., 52 (10), (Oct. 1981).

21 E.K. Storm, J. Applied Physics, 50, p. 4450, (June 1979).

22 K.O. Axelsson, K.E. Keck and B. Kasemo, Surface Science, 164, 109-126 (1985).

23 Yu.M. Goryachev, I.A. Podchernyaeva, N.I. Siman, V.S. Senel'nikova, I.I. Timofeeva and G.S. Burkhanov, Sov. Phys. Tech. Phys., 23 (3) 321 (1978).

24 G.A. Hass and R.E. Thomas, in E. Passaglia, ed., Techniques of Metals Research, Vol. VI, Part 1, Chapter 2, Interscience Publishers, 1972.

25 Hass and Thomas, ibid., p. 122.

26 L.W. Swanson and P.R. Davis, Methods of Experimental Physics, Vol. 22, Academic Press, 1985.

27 L.W. Swanson et al., Final Report, contract NAS3-8910, Field Emission Corp., (1967).

28 W. Gordy and W.J.O. Thomas, J. of Chemical Physics, 24, 439 (2/1956).

29 L. Pauling, The Nature of the Chemical Bond, 3rd ed., Ithica, N.Y., Cornell Univ. Press, 1960.

30 D. Stiener and E.P. Gyftopolous, Proc. of the 7th Annual Conf. on Physical Electronics, MIT, Cambridge, MA (1967), unpub.

31 J. Hinze, M. Whitehead and H. Jaffe, J. Am. Chem. Soc., 85, 148 (1963).

32 W. Gordy, Phys. Rev., 69, 604 (1946).

33 J.C. Slater, Quantum Theory of Molecules and Solids, New York, N.Y., McGraw-Hill Co., 1965.

34 L.W. Swanson, P.R. Davis and M.A. Gesley, Final Report, Contract F19628-80-C-0117, Oregon Graduate Center, (1981).

35 S. Yamamoto, K. Susa and U. Kawabe, J. of Chemical Physics, 60, (10), 4076 (1974).

36 J.K. Wilmshurst, J. Chem. Phys. 27, 1129 (1957).

37 C.A. Coulson, Valence, 2nd ed., Amen House, London, Oxford Univ. Press, 1961.

38 M.D. Smolin, I.A. Podchernyaeva, N.I. Siman and V.S. Sinel'nikova, Sov. Phys. Tech. Phys., 26 (9) 1158 (1981).

39 C. Oshima, T. Tanaka and M. Aono, Appl. Phys. Letters, 35 (10) 822 (1979).

40 J.C. DeVos, "Evaluation of the Quality of a Blackbody," Physica XX, 669-689 (1954).

41 L.N. Grossman, "High Temperature Thermophysical Properties of ZrC," J. Am. Ceramic Soc., 48 (5) 236 (1965).

42 V.A. Petrov, V.Ya. Chekhovskoi, A.E. Sheindlin, V.A. Nikolaeva and L.P. Fomina, High-Temperature Inst., Academy of Sci. of the USSR., Translated from Teplofizika Vysokikh Temperatur, Vol. 5, No. 6, 995 (1967).

APPENDIX: SPECTRAL EMISSIVITY OF ZrC

A. Spectral Emissivity's Defining Equations

The spectral emissivity or the monochromatic emissive power is defined as the ratio of the energy radiated from a body at some given wavelength to the energy at that same wavelength radiated by a black body at the same temperature. The spectral emissivity can be determined practically by comparison of the observed surface temperature of a material with that of a blackbody cavity existing in the same material. The equation for calculating the spectral emissivity is

$$\ln \varepsilon_{0.65\mu_m} = C_\lambda/\lambda_e(1/T_{BB} - 1/T_{br}) \qquad (56)$$

where T_{BB} is the absolute temperature shown by the blackbody cavity, T_{br} is the absolute temperature measured on the surface of the specimen, C_λ is a constant (C_λ = 1.438 μ.deg.), and λ_e is the wavelength of the light detected. In this case the wavelength used for the spectral emissivity measurements was 0.65 μm, the common wavelength used for optical pyrometric measurements.

The derivation of Eq. (56) easily follows from Plank's radiation formula which gives the radiancy of a body at temperature T, observed at wavelength λ, as

$$R_\lambda = c_1/\lambda^5[1/(e^{\varepsilon/\lambda T} - 1) \qquad (57)$$

where $c_1 = 2\pi c^2 h$ and $\varepsilon = hc/k$. Since the emissivity is a ratio of energies or radiances the factors c_1/λ^5 cancel. Also $e^{\varepsilon/\lambda T} \gg 1$ so we can drop the unity term without adversely effecting our results. Hence, since $\varepsilon_\lambda(T) = R_\lambda(T_{br})/R_\lambda(T_{BB})$ we arrive at Eq. (56)

B. Blackbody Considerations

A key element in this measurement is to approximate a blackbody very closely. The common method is to drill a hole in the material and view the light coming from the bottom of the hole. To accurately mimic a blackbody the depth to radius ratio needs to be 20:1.[40]

C. Sample Preparation and Apparatus

The ZrC samples used were zone melted from 0.125 x 0.125 inch sintered rods. After zone melting the rods were ground to a finished diameter of 0.100 inch using 600 mesh diamond powder on a centerless grinder. A typical rod had a C to Zr ratio of 0.91 and was polycrystalline in nature, with randomly oriented and shaped crystals approximately 0.100 inches in diameter.

A 0.600 to 0.700 inch sample was ground flat on one end, first with a 600 mesh diamond wheel, and was then finished optically smooth with 15

μm and finally 6 μm diamond impregnated mylar. Two sizes of blackbody holes were tried, one 0.030 inches in diameter and the other 0.040 inches in diameter. The best results were obtained from the 0.040 inch diameter hole which was drilled 0.400 inch deep. The drilling was accomplished by using commercially available diamond drills flushed with ethanol.

The samples were held either in a solid Mo holder held in turn by two close wraps of 0.030 inch W wire, or directly by the W wire itself. The best runs were taken using the Mo sheath, which tended to provide a more uniform temperature throughout the sample. Heating was accomplished by electron bombardment from a 0.010 inch W filament, wrapped 0.100 inch from the Mo sleeve.

The measurements were taken in a vacuum, with the Mo holder and filament being mounted on a 2.75 inch stainless steel flange. This flange was attached to one side of a 1.5 inch stainless steel cross as is depicted in Fig. 74. The window shield disc could be closed to block the pyrex window from contamination or opened to allow viewing of the crystal face and blackbody hole. Pressures in the vacuum system were typically in the 10^{-7} torr range, with a maximum allowed pressure of 5×10^{-6} torr.

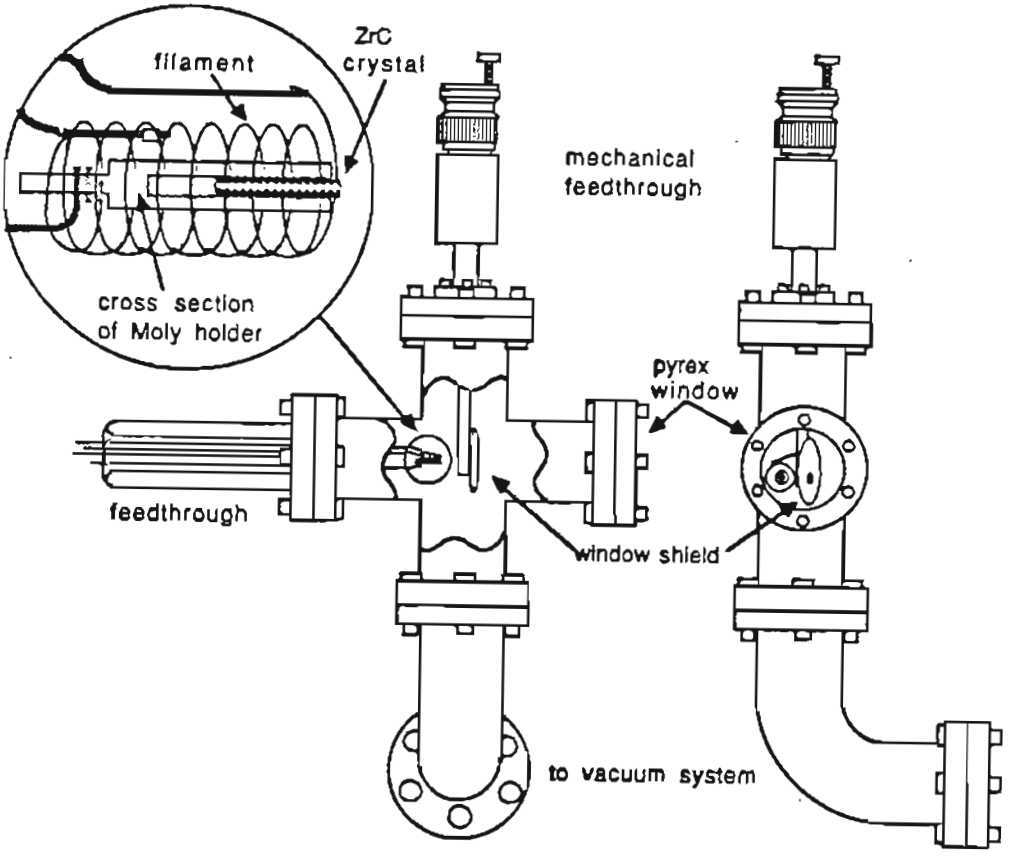

Fig. 74: Schematic of apparatus used in the spectal emissivity measurements.

D. Results

Some preliminary data were taken on sintered ZrC, and also carbon as a system check. The sintered data agrees with that taken by Grossman,[41] but needed to by corrected based on correction runs generated from the carbon data. The data by Grossman and that of Petrov[42], are for sintered ZrC and are the only references found for spectral emissivity.

These data are analyzed using a modified version of Eq. (56),

$$\varepsilon = \exp[C_\lambda/\lambda_e(1/cT_{BB} - 1/cT_{out})] \qquad (58)$$

Where c = 1.01 is a correction for window transmission. The results are plotted in Figs. 75 and 76 and represent many separate runs taken with three different crystals, each prepared identically. Fig. 76 is a comparison of the curve generated here with the data on sintered ZrC. The curve shown in Fig. 75 was used in the evaluation of temperature data used in the thermionic work.

The crystalline ZrC did not exhibit any variation with crystal direction. This effect would have been easily observed, since grinding the surface usually exhibited two or three distinct faces. No crystal structure was detected while viewing the heated crystal with the optical pyrometer.

Surface contamination could lead to differences in the spectral emissivity as noted by Grossman.[41] However, AES data reported in

section VIIA indicated that contaminants were removed at temperatures greater than 1500 C. In addition, data were usually taken at the higher temperatures before the low temperature data were taken.

As an additional verification of the $\varepsilon(T)$ function obtained, another experiment was performed. A previously used sample was ground with 600 mesh (40 μm) diamond grit. This was done to mimic the surface of samples generally used in the other experimentation. The data in Fig. 77 shows little variation from the $\varepsilon(T)$ function found using the 6 μm polished surface.

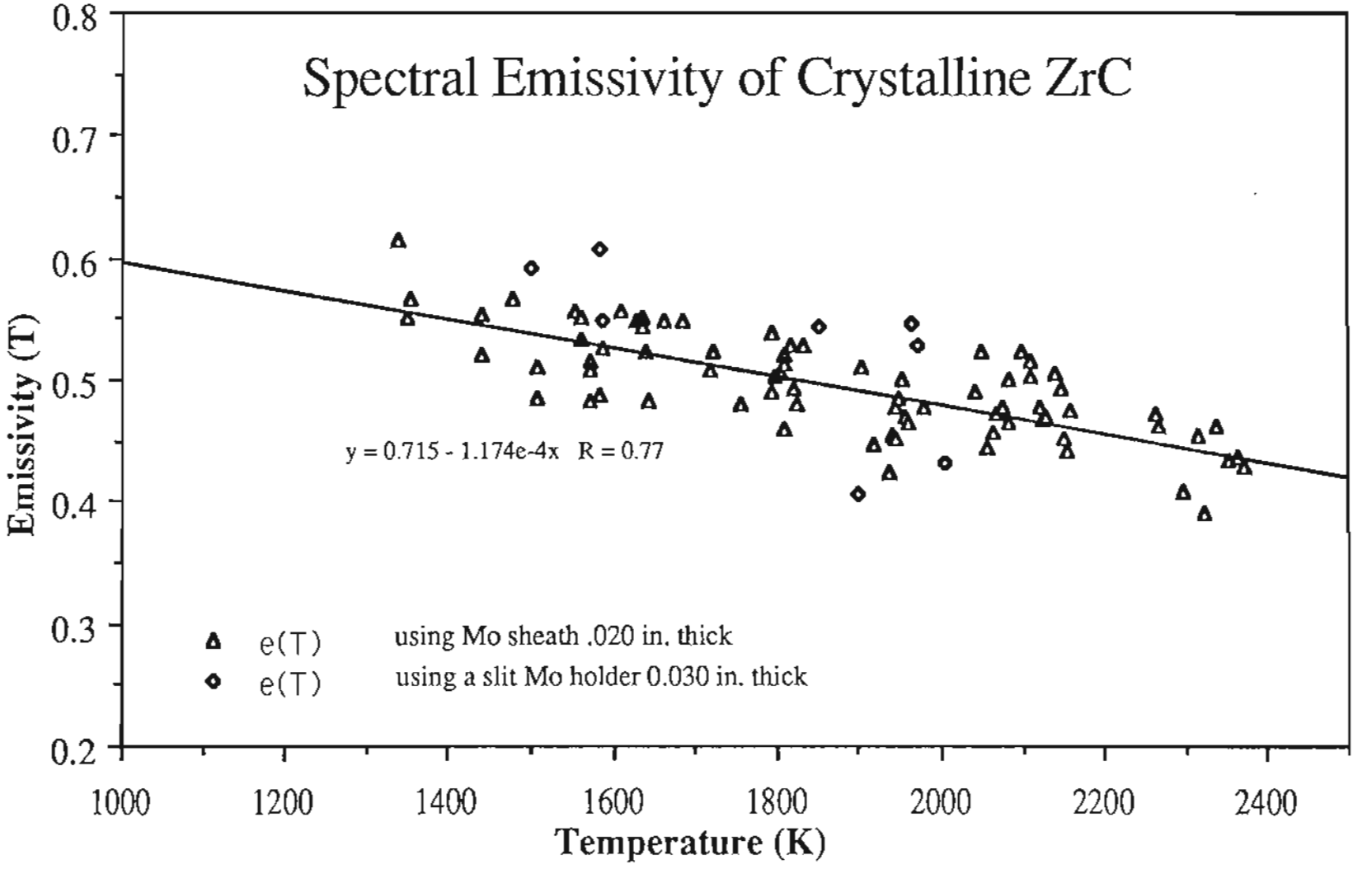

Fig. 75: Spectral emissivity (0.65 μm) as a function of temperature for crystalline ZrC.

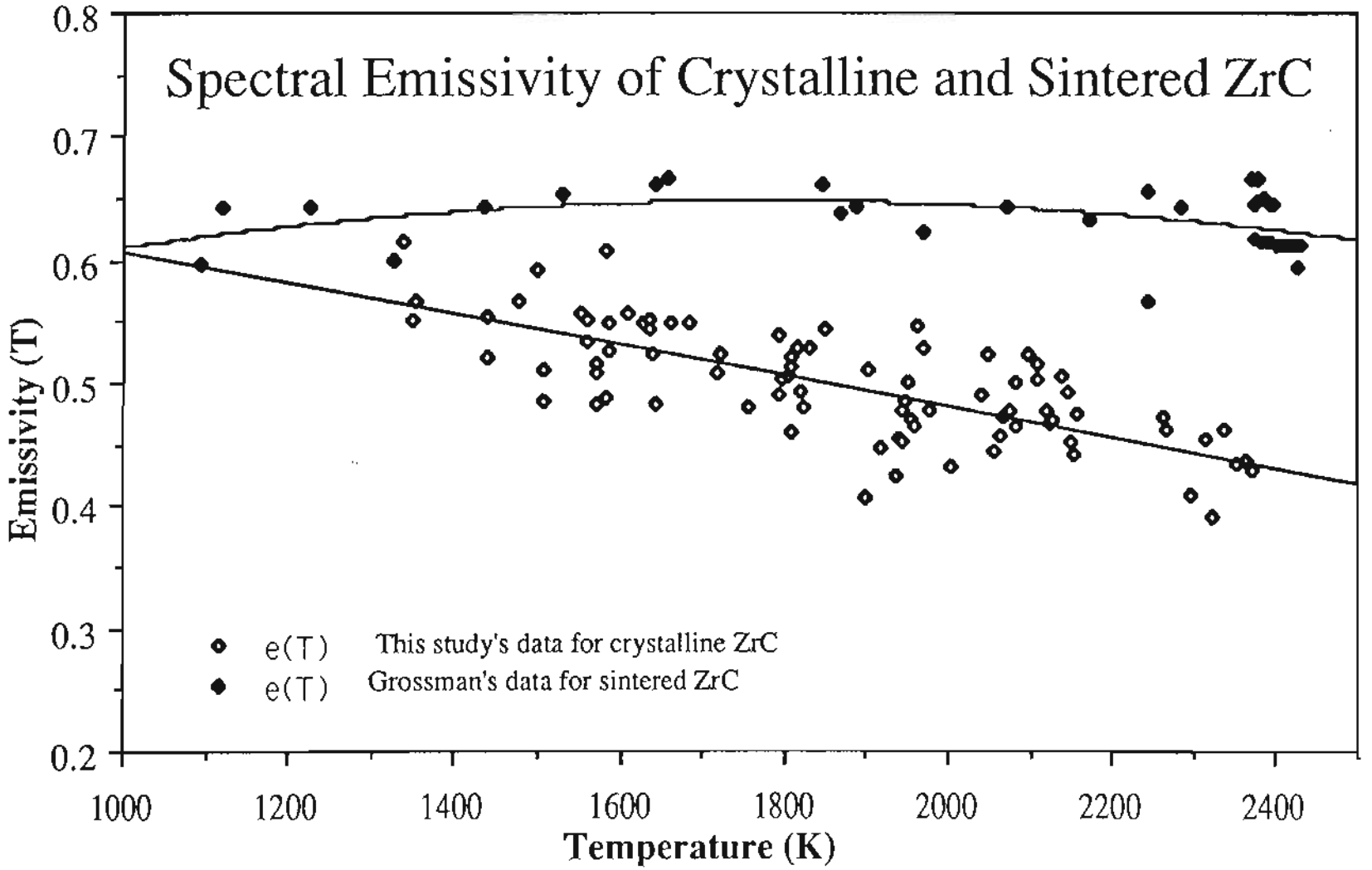

Fig. 76: Comparison of crystalline spectral emissivity with that of Grossman's sintered ZrC data.

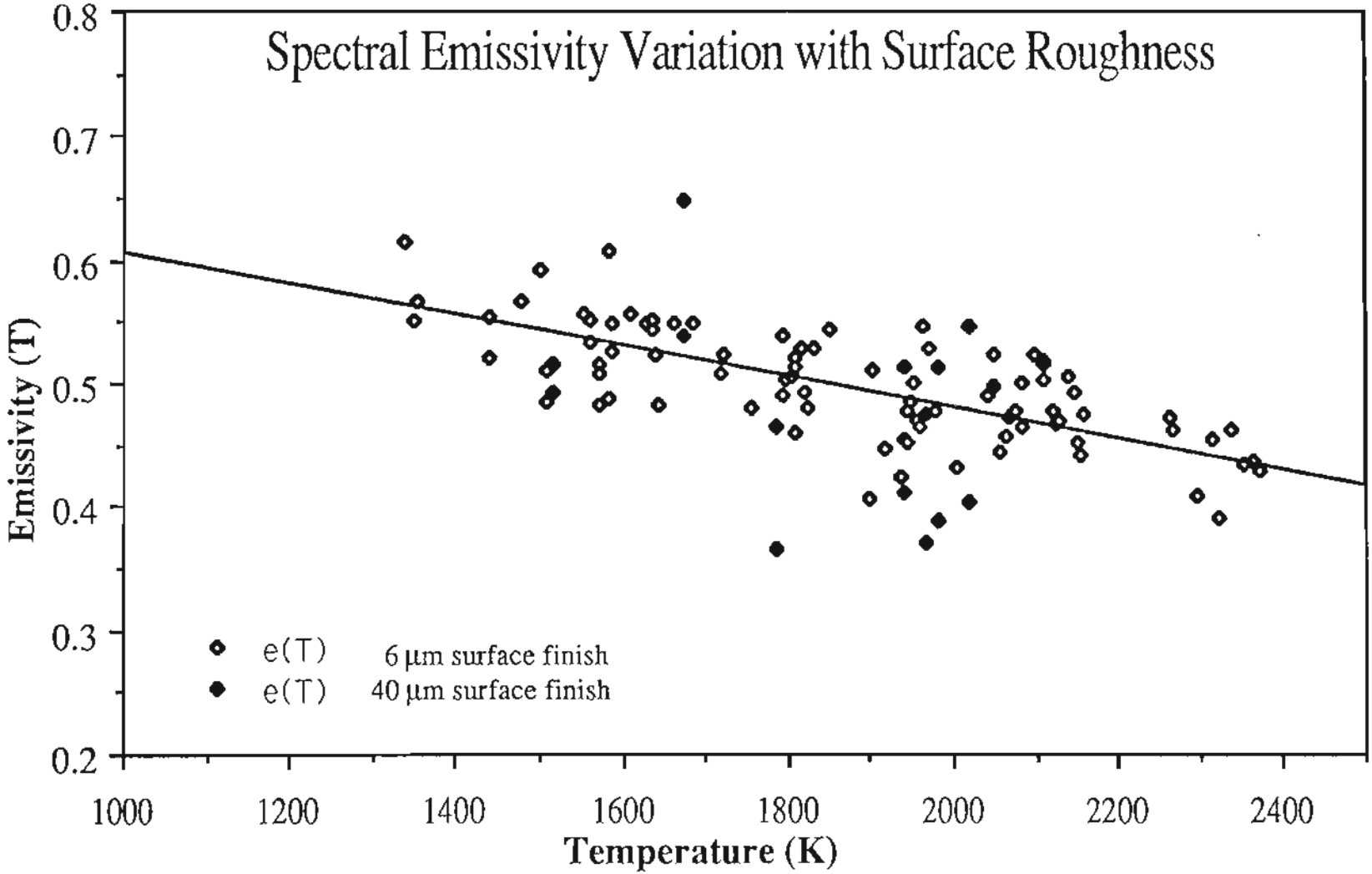

Fig. 77: Variation of spectral emissivity with surface roughness.

BIOGRAPHICAL NOTE

The author was born 8 September 1949 in Portland, Oregon, but lived in McNary, Oregon. In 1952 he moved to Mill City, Oregon and in 1960 moved to Bonneville, Oregon and while there attended and graduated from Stevenson High School, Stevenson, Washington in 1967. He then entered Linfield College, McMinnville, Oregon, graduating with a Bachelor of Arts degree in June 1971.

From 1970 to 1976 the author worked at Linfield Research Institute, McMinnville, Oregon, as a surface physics researcher and as an Adjunct Instructor.

After two years of energy consulting work, he worked from 1978 to 1980 at the Oregon Department of Energy as a contract monitor and speaker on energy conservation in building design and land use planning.

From 1980 to 1983 he was a general contractor, designing and building passive solar, energy conserving homes in Yamhill County, Oregon.

From 1983 to 1987 he has been an Adjunct Instructor and research technician at Linfield College in addition to studying at the Oregon Graduate Center. The requirements for the degree Doctor of Philosophy were completed in August of 1987.

As of July 1987 he accepted a position as Assistant Professor of Physics at Linfield College.

The author has been married 18 years to the former Marsha Hileman.

They have three children, Heather, age 14, Laura, age 3 and Emily, age 2.5 months.